Rood, A.H., Rood, D.H., Balco, G., Stafford, P.J., Ludwig, L.G., Kendrick, K.J., and Wilcken, K.M., 2022, Validation of earthquake ground-motion models in southern California, USA, using precariously balanced rocks: GSA Bulletin, https://doi.org/10.1130/B36484.1.

Supplemental Material

Figure S1. The following figures are equivalent to Figures 2, 3, and 5 in the main text, for all 20 precariously balanced rocks (PBRs) in this study.

Table S1-1. Table 1.1. Full parameters used for PBR sample data reduction.

Table S1-2. Full parameters used for stream sediment sample data reduction.

Table S1-3. Full parameters used for saprolite sample data reduction.

Table S1-4. Data on process blanks

Table S2. Inputs to Balco et al. (2011) fragility age model: Sample-specific constants, and ^{10}Be concentrations for all the PBR samples.

Table S3. Best-fit parameter results of the fragility age forward model.

Table S4. Median and 16th-84th percentile uncertainty parameter results of the fragility age forward model.

Table S5. Stream sediment samples online erosion rate calculator inputs and outputs.

Table S6. Saprolite samples online erosion rate calculator inputs and outputs.

Supplementary Materials for

Validation of earthquake ground-motion models in southern California using precariously balanced rocks

Contents of this file

Figure 1
Tables 1 to 6

Figure 1

Introduction

The following figures are equivalent to Figures 2, 3, and 5 in the main text, for all 20 precariously balanced rocks (PBRs) in this study. One page is dedicated to each PBR and includes all three results figures (fragility, fragility age, and hazard validation) for that PBR. The general figure captions are provided below. PBR-specific captions and discussion are provided for each PBR on its dedicated page.

Fragility Results. (A) Field photo of the most slender view of the PBR on its pedestal compared to the 3-D model constructed of the PBR using photogrammetry. (B) Area of the PBR 3-D model that is in contact with the pedestal, i.e., the base of the rock, labelled with measured geometric parameters required for toppling calculations. Gray circles are the critical rocking points that define the narrowest basal 2-D section through the center of mass (yellow circle). Alpha values (in radians) are gray text and radius length (in meters) are in yellow. The lowest alpha value is the direction the rock will topple. (C) Fragility function of the PBR. The 25th, 50th (median), and 75th percentile ground motions are labeled.

Fragility Age Results. (A) Sample locations labelled as blue circles on a field photo of the PBR. (B) Graphs show ^{10}Be concentration (x-axis) and depth below PBR top (y-axis). Left graph shows the components of the total predicted nuclide concentration attributable to different phases of PBR exhumation. Blue line is before exhumation, yellow line is during exhumation, and gray line is after exhumation. Right graph shows the measured nuclide concentrations in samples (blue circles) compared with those predicted by the forward model best-fitting parameters (open black circles). Light gray circles are samples that were not used in the modeling of PBR. Yellow circles are the measured concentration in the saprolite sample plotted at the approximate height in the landscape relative to the PBR. Error bars show 1σ uncertainty on measured nuclide concentrations; error bars that are not visible are equal to or smaller than the size of the symbols. The horizontal dashed line is the height of the lowest point on the PBR-pedestal contact. (C) Histogram of t_{tip} age, in ka, calculated by each of the 400 Monte Carlo iterations. Cumulative black curve of output t_{tip} ages are labelled at the 16th, median (50th), and 84th percentile ages.

Hazard Validation Results. (A) Hazard curves computed by the OpenQuake engine (Pagani et al., 2014) for the location of the PBR. The lower (dotted line), central (solid line), and upper (dashed line) are plotted for each ground-motion model (GMM) as well as the weighted mean hazard curve (yellow line). Each hazard curve is produced by the "true mean" UCERF3 source model with each branch of the GMM logic tree (Field et al., 2013; Rao et al., 2017). The spread between the upper and lower backbone hazard curves for each GMM represents the epistemic uncertainty in the ground motions estimated by that GMM. (B) The hazard curves for the location of the PBR (the same curves as in A) colored by whether they pass the PBR validation, i.e., the ground-motion estimates are consistent with a 5% probability of survival of the PBR, or fail the PBR validation, i.e., the ground-motion estimates are inconsistent with a 5% probability of survival of the PBR.

BR1

Fragility Results

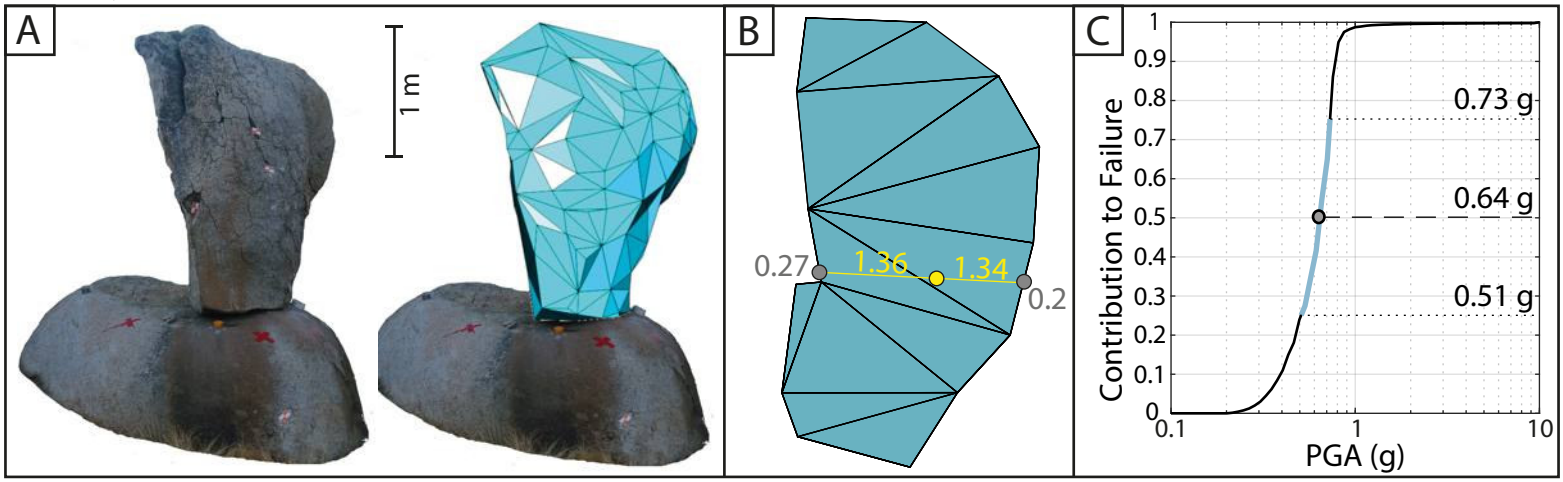

(A) One planar side of the PBR with a lighter color than the rest of the outcrop (left side in photo) may indicate significant mass loss, resulting in the PBR geometry evolving at some unknown time before the present. However, there was no evidence of this lost material on the ground surface below the pedestal. (B) The two alternative methods of selecting α_1 and α_2 produce near identical values, therefore, we are confident that the basal area of BR1 approximates the rectangular basal geometry that was described by the Purvance et al. (2008) fragility equations. α_2 is 1.34 times greater than α_1, so BR1 is classified as having an asymmetric rocking response. A narrower bottom than top of the PBR results in a high center of mass over a small basal area.

Fragility Age Results

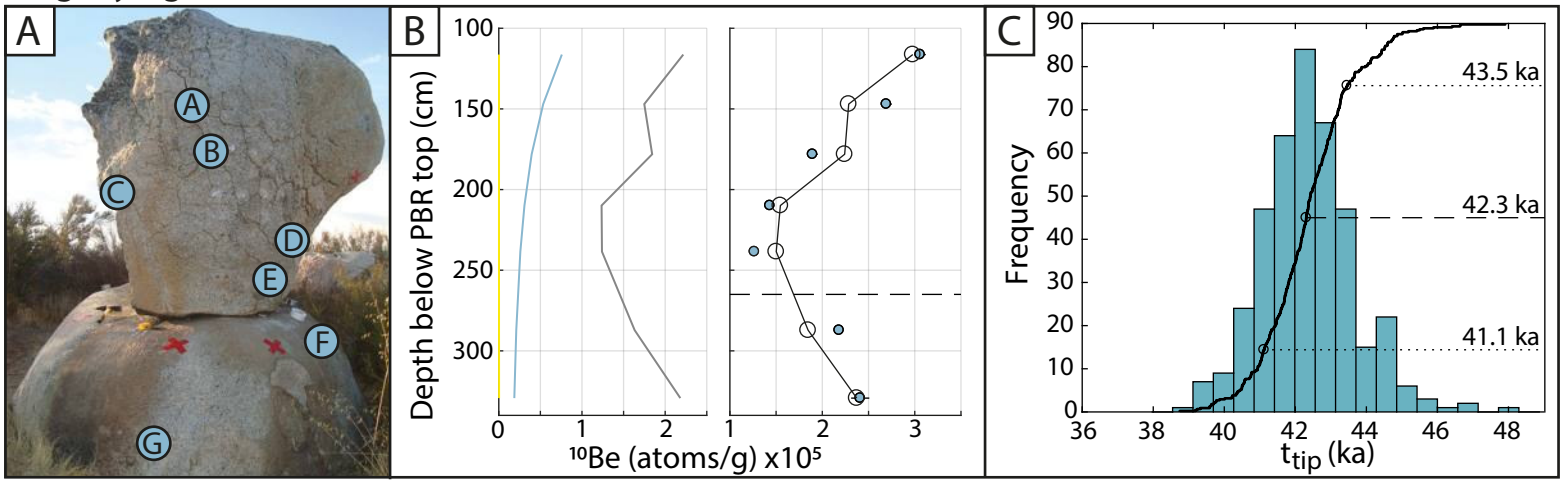

(A) Field observations of case-hardening and dark varnished areas on the sampled side of PBR and pedestal indicate an aged rock surface and, therefore, little post-exhumation physical weathering. Samples A - E are on the PBR and samples F and G are on the pedestal. (B) An instantaneous exhumation rate, ε_1, results in no ^{10}Be accumulation during exhumation (yellow line). The overprediction of modeled ^{10}Be concentration in sample C, attributed to the post-exhumation phase of accumulation (gray line), may support the occurance of mass loss from one side of BR1. Sample C is located on the edge of where the mass loss may have occurred and so it's shielding based on the present geometry would be significantly lower than a pre-mass loss geometry, resulting in the ^{10}Be concentration to be overpredicted. Misfit between the modeled and measured ^{10}Be concentrations of other samples may suggest that the shielding has changed through time or differential erosion has occurred.

Hazard Validation Results

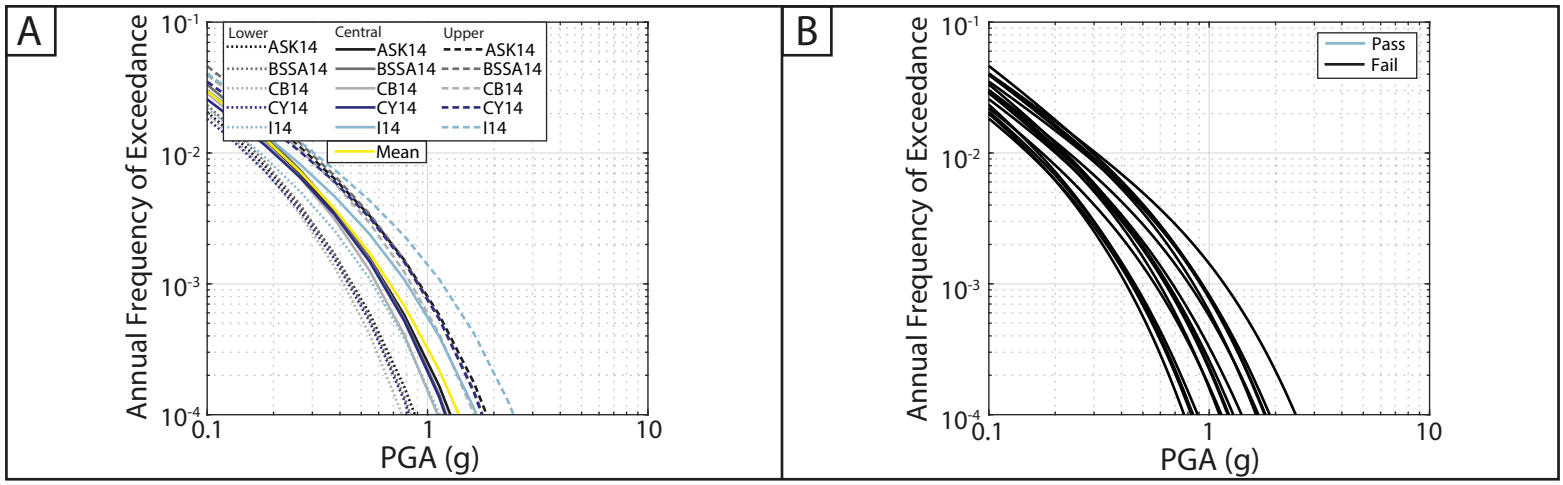

BR1 is located between the San Jacinto and Elsinore faults, which are the dominant seismic sources controlling the seismicity at the site. The old fragility age and unstable fragility of BR1 cause all three branches (upper, central, and lower) of all five GMMs to be inconsistent with a 5% probability of survival of BR1. The removal of the I14 GMM, at 2475 year mean return period, reduces the mean ground-motion estimate by 4% and the reduces the range of estimated 5th–95th fractile ground motions by 29% at the BR1 site.

BS1

Fragility Results

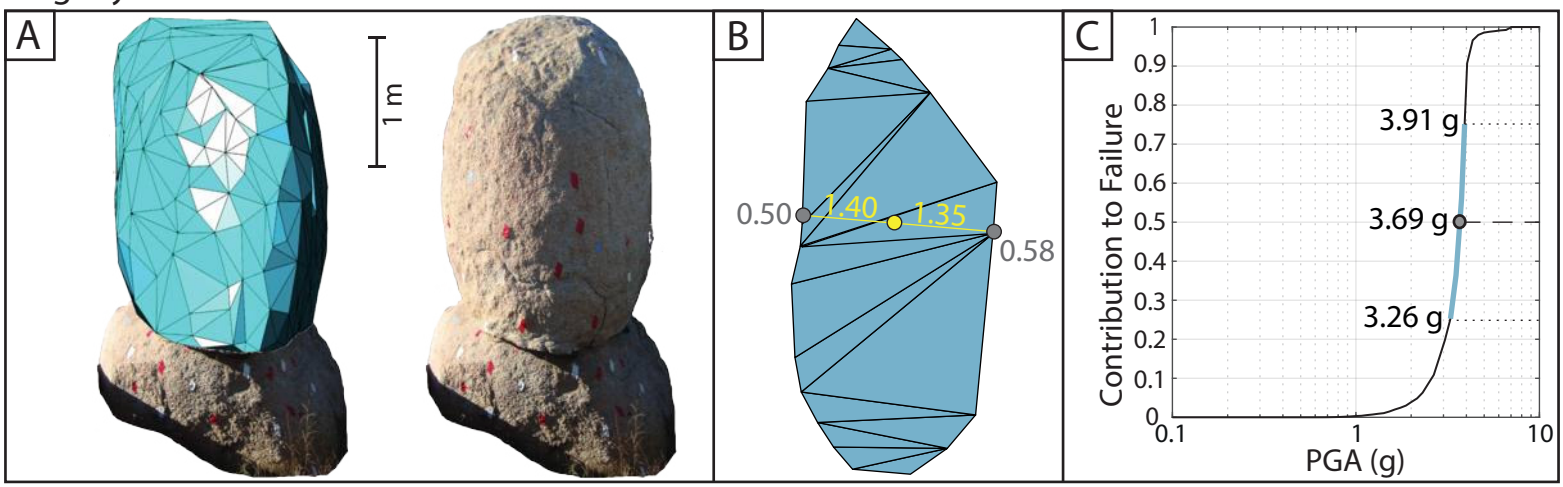

(A) There was no evidence of post-exhumation erosion of the PBR. B) The two alternative methods of selecting α_1 and α_2 produce identical critical rocking points, therefore, we are confident that the basal area of BS1 approximates the rectangular basal geometry than was described by the Purvance et al. (2008) fragility equations. α_2 is a factor of 1.15 greater than α_1, so BS1 is classified as having an asymmetric rocking response. The tall but wide geometry of BS1 means that this is the least fragile PBR we studied. However, the α_2 of BS1 is greater than the range investigated by Purvance et al. (2008), which reduces our confidence in the fragility characterization of BS1.

Fragility Age Results

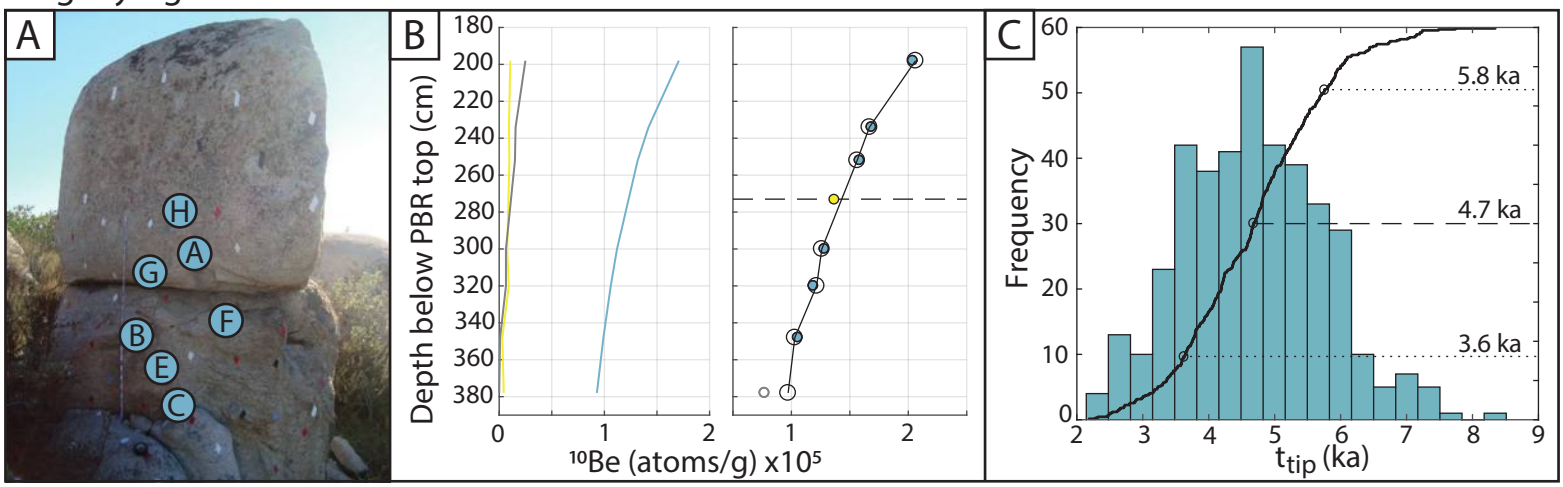

(A) Samples A, G, and H are located on the PBR and samples B, C, D, and F are located on the pedestal. (B) Sample C was excluded from the model fitting because field observations suggested a block was recently removed from the position of sample C. The removal of such a block would have the effect of the present shielding being too low and, therefore, the ^{10}Be production rate being too high. This potential block removal is supported by the forward model overpredicting the ^{10}Be concentration in C, as a result of an erronously high production rate for this sample. The remaining 6 samples used by the forward model are equally distributed above and below the pedestal and span ~1.5 m. The saprolite sample at this site was collected at approximately the height of the PBR-pedestal contact. The measured ^{10}Be concentration in the saprolite sample (yellow circle) matches the concentrations predicted by the forward model, which validates the model and its results.

Hazard Validation Results

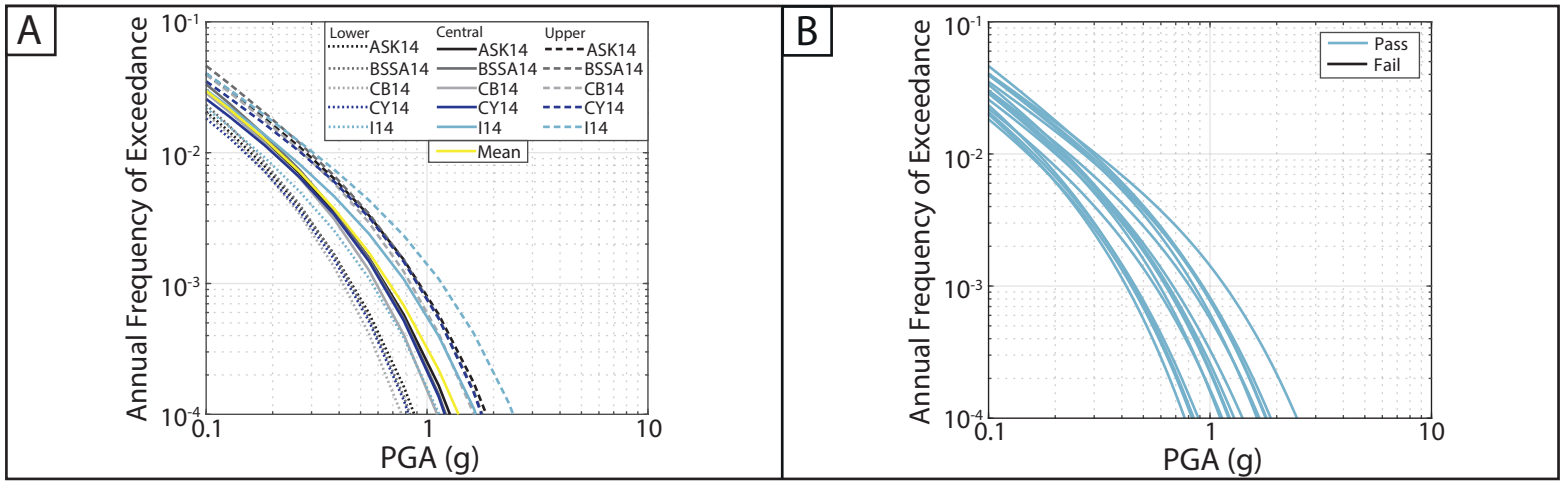

BS1 is located between the San Andreas and San Jacinto faults, which are the dominant seismic sources controlling the seismicity of the site. The relatively young fragility age and stable fragility of BS1 cause none of the three branches (upper, central, and lower) of all five GMMs to be inconsistent with a 5% probability of survival of BS1. The removal of the I14 GMM, at 2475 year mean return period, reduces the mean ground-motion estimate by 4% and the reduces the range of estimated 5th–95th fractile ground motions by 29% at the BS1 site.

BS2

Fragility Results Figures

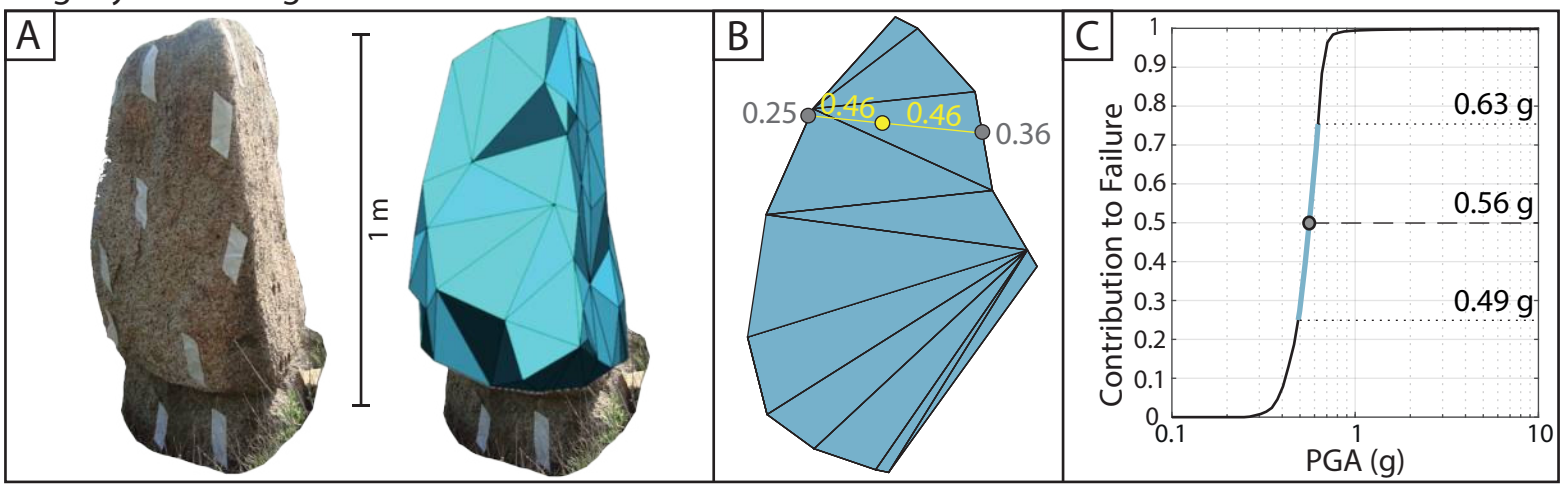

(A) The planar sides of BS2 align with the planar sides of the pedestal, therefore, we are confident that the PBR rhas the same geometry as when it was exhumed and that post-exhumation erosion has not occurred. (B) The wedge-shaped basal geometry of BS2 and the overhang at the narrower end cause the center of mass to be located much closer to one end of the PBR than the other. The geometry of BS2 is such that there is a 20% difference in α_1 and a 53% difference in α_2 between the two alternative methods of selecting the critical rocking points. It's geometry, therefore, greatly differs from the rectangular block geometry that the Purvance et al. (2008) fragility equations were intended to model, which reduces our confidence in the fragility characterization of BS2.

Fragility Age Results Figures

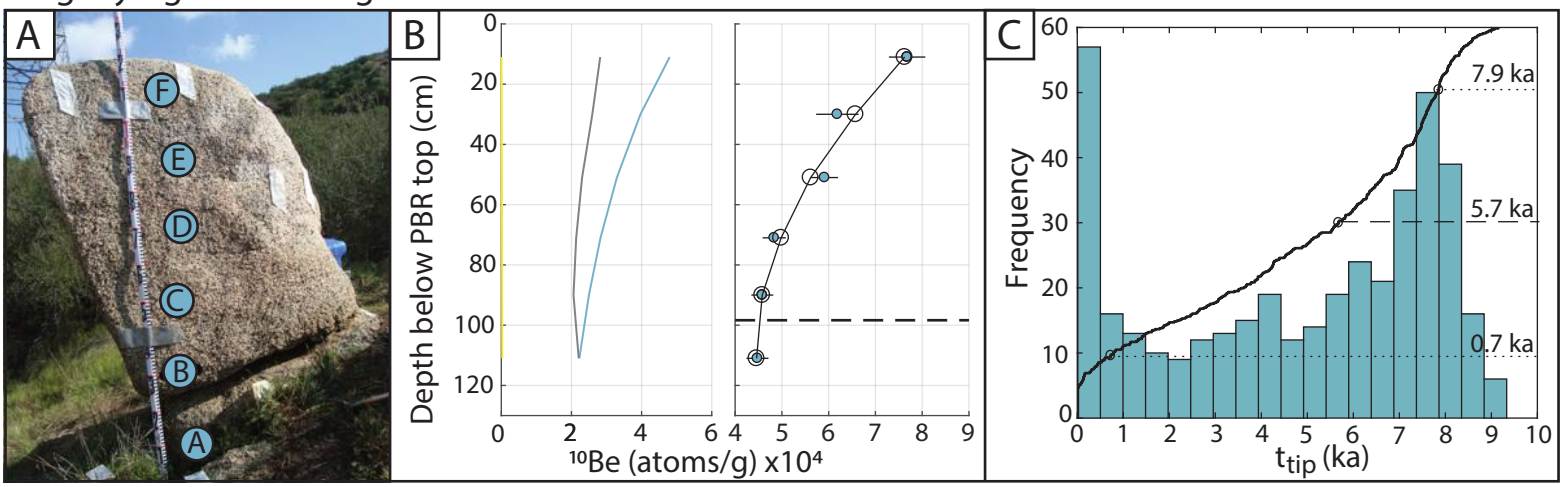

(A) Samples B - F are located on the PBR and sample A is located on the pedestal. The short pedestal height made it possible to only collect a single sample from the pedestal. (B) The best-fit ε_1 value is an instantaneous exhumation rate, therefore, no ^{10}Be accumulation during exhumation is modeled (yellow line). The best-fit modeled ^{10}Be concentrations of all samples overlap the measured ^{10}Be concentrations within 1σ uncertainties. (C) The spread of t_{tip} ages is the result of a large uncertainty in the Monte Carlo ε_1 results. The high ε_1 values produce the older t_{tip} ages and the young age tail and peak are associated with lower ε_1 values. Because the samples were collected from a planar surface, the shielding values result in a post-exhumation ^{10}Be profile (gray line) that has a shape similar to the pre-exhumation ^{10}Be profile (blue line), which has the net effect of producing a non-unique t_{tip} solution.

Hazard Validation Results Figures

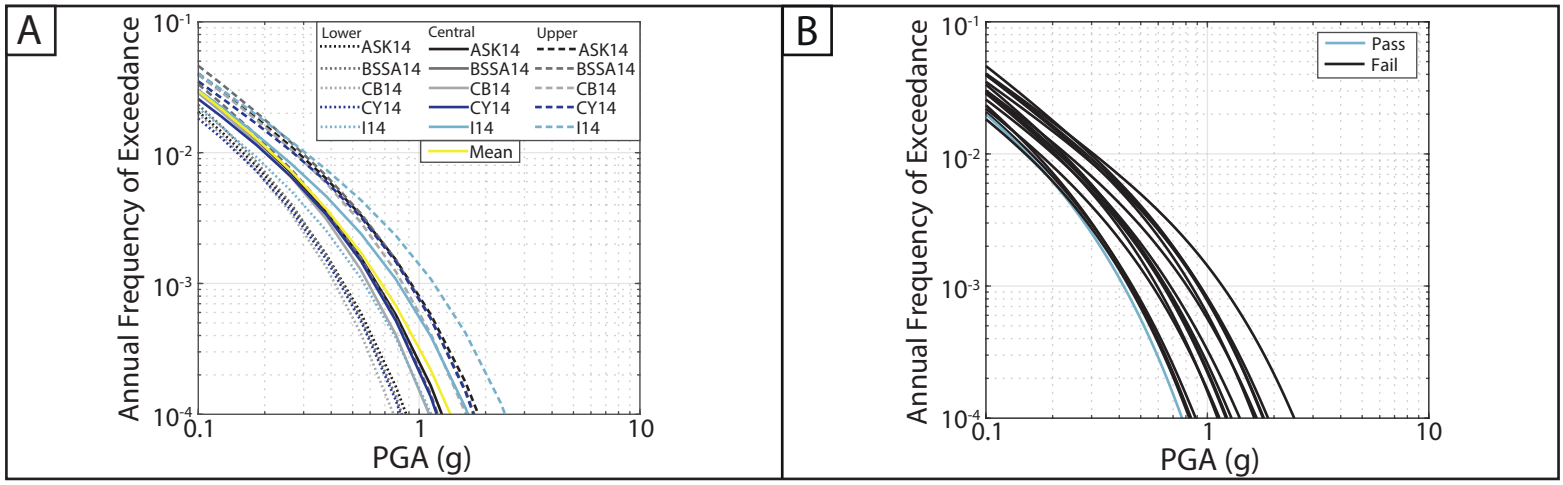

BS2 is located between the San Andreas and San Jacinto faults, which are the dominant seismic sources controlling the seismicity of the site. The relatively young fragility age and moderate fragility of BS2 cause the ground-motions estimated by the central and upper branches of all five GMMs and the lower branch of ASK14, BSSA14, CY14, and I14 to be inconsistent with a 5% probability of survival of BS2. The removal of the I14 GMM, at 2475 year mean return period, reduces the mean ground-motion estimate by 4% and the reduces the range of estimated 5th–95th fractile ground motions by 29% at the BS2 site.

GV1

Fragility Results Figures

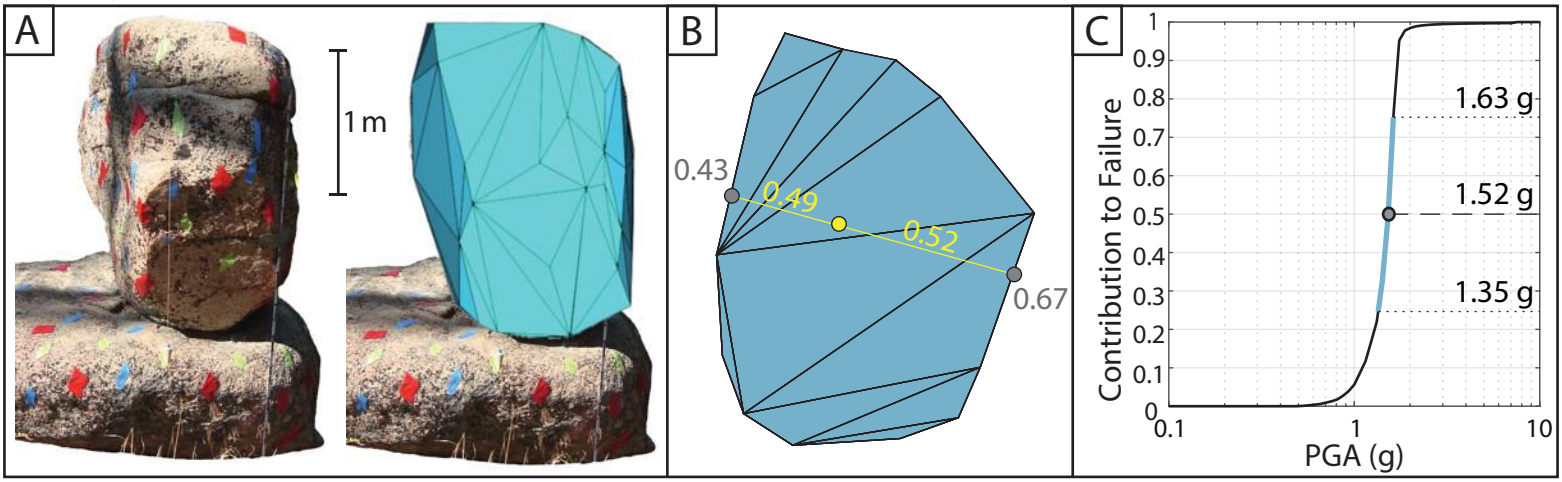

(A) Dark varnish on the PBR and pedestal indicates the occurrence of negligible post-exhumation erosion. (B) The two alternative methods of selecting α_1 and α_2 produce the same critical rocking points, therefore, we are confident that the basal area of GV1 approximates the rectangular basal geometry than was described by the Purvance et al. (2008) fragility equations. α_2 is 1.57times greater than α_1, so GV1 is classified as having an asymmetric rocking response. However, the α_2 of GV1 is greater than the range investigated by Purvance et al. (2008), which reduces our confidence in the fragility characterization of GV1.

Fragility Age Results Figures

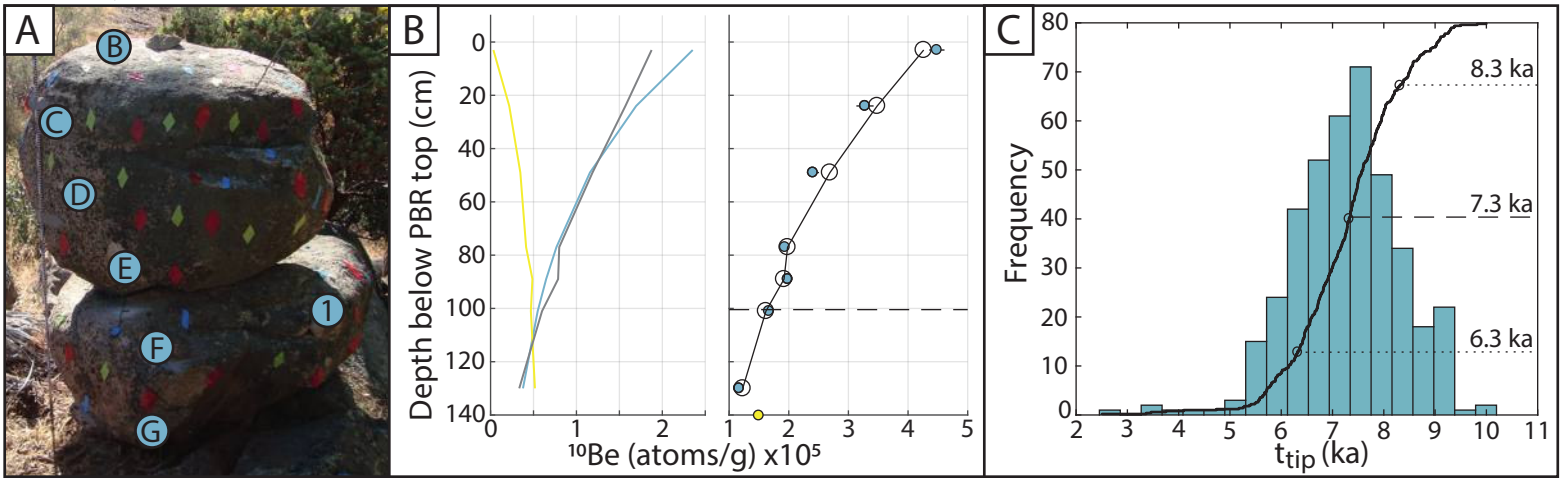

(A) Samples B-E are located on the PBR and samples 1, F, and G are located on the pedestal. (B) The fact that the samples were not collected from a single planar surface, but instead curve around one side of the pedestal, results in the shape of the post-exhumation profile of ^{10}Be concentration with sample depth (gray line) to be distinct from the pre-exhumation profile of ^{10}Be concentration with sample depth (blue line). The best-fit modeled ^{10}Be concentrations of all samples overlap the measured ^{10}Be concentrations within 1σ uncertainties. The saprolite sample was collected on the ground surface. The measured ^{10}Be concentration in the saprolite sample is within the range of concentrations, which validates the model and its results.

Hazard Validation Results Figures

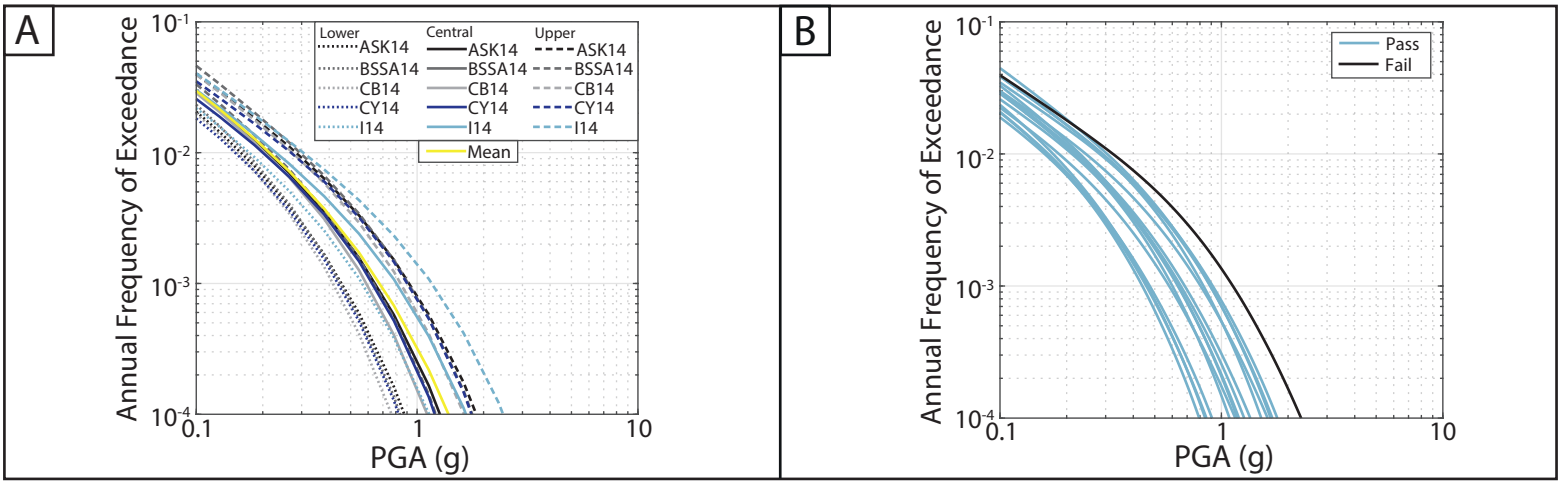

The dominant seismic sources for the GV1 site are the San Andreas fault, Cleghorn fault, San Jacinto fault, and North Frontal thrust faults. The combination of the moderately old fragility age and relatively stable fragility of GV1 causes the ground-motions estimated by the upper branch of I14 to be inconsistent with a 5% probability of survival of GV1. The removal of the I14 GMM, at 2475 year mean return period, reduces the mean ground-motion estimate by 4% and the reduces the range of estimated 5th–95th fractile ground motions by 27% at the GV1 site.

GV2

Fragility Results Figures

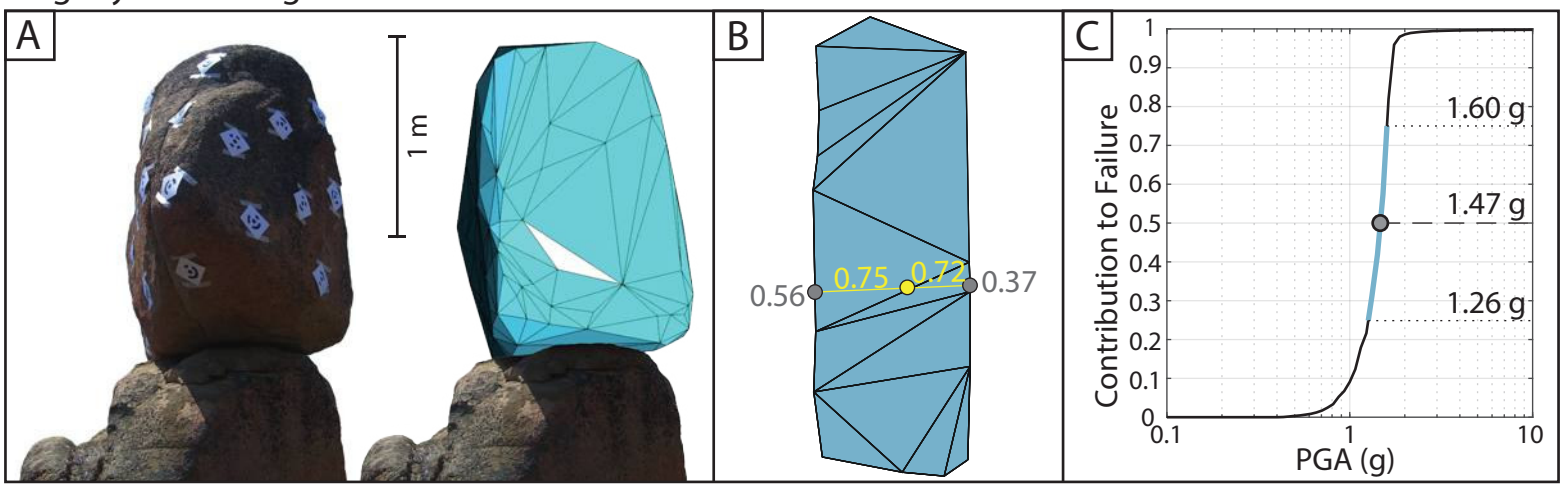

(A) Dark varnish on the PBR and pedestal indicates the occurrence of negligible post-exhumation erosion. The PBR overhangs its pedestal at one end, however, this is not in the 2-D rocking direction and so does not contribute to the fragility of the PBR. (B) The two alternative methods of selecting α_1 and α_2 produce the same critical rocking points, therefore, we are confident that the basal area of GV2 approximates the rectangular basal geometry than was described by the Purvance et al. (2008) fragility equations. α_2 is 1.49 times greater than α_1, so GV2 is classified as having an asymmetric rocking response. However, the α_2 of GV2 is greater than the range investigated by Purvance et al. (2008), which reduces our confidence in the fragility characterization of GV2.

Fragility Age Results Figures

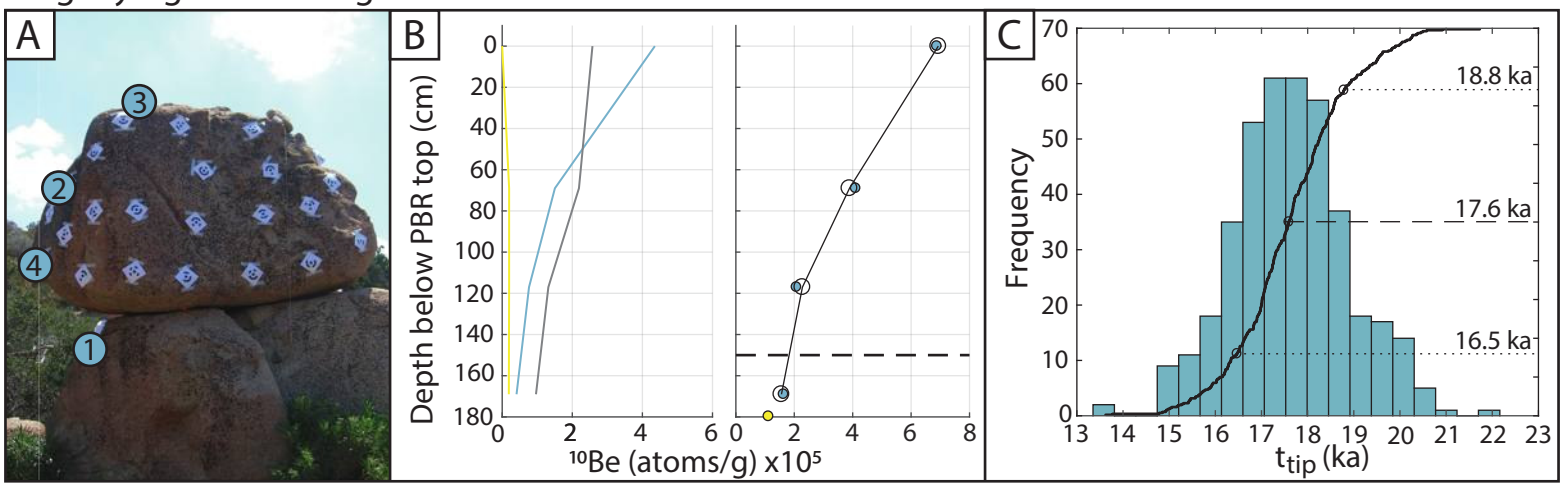

(A) Samples 2 - 4 are located on the PBR and sample 1 is located on the pedestal. (B) The fact that the samples were not collected from a single planar surface, but instead curve around one side of the PBR and pedestal, results in the shape of the post-exhumation profile of ^{10}Be concentration with sample depth (gray line) to be distinct from the pre-exhumation profile of ^{10}Be concentration with sample depth (blue line). The best-fit modeled ^{10}Be concentrations of all samples overlap the measured ^{10}Be concentrations within 1σ uncertainties. The saprolite sample was collected on the ground surface ~1 m below sample 1. Therefore, the measured ^{10}Be concentration in the saprolite sample is expected to be lower than in sample 1, which is what is observed and validates the model and its results.

Hazard Validation Results Figures

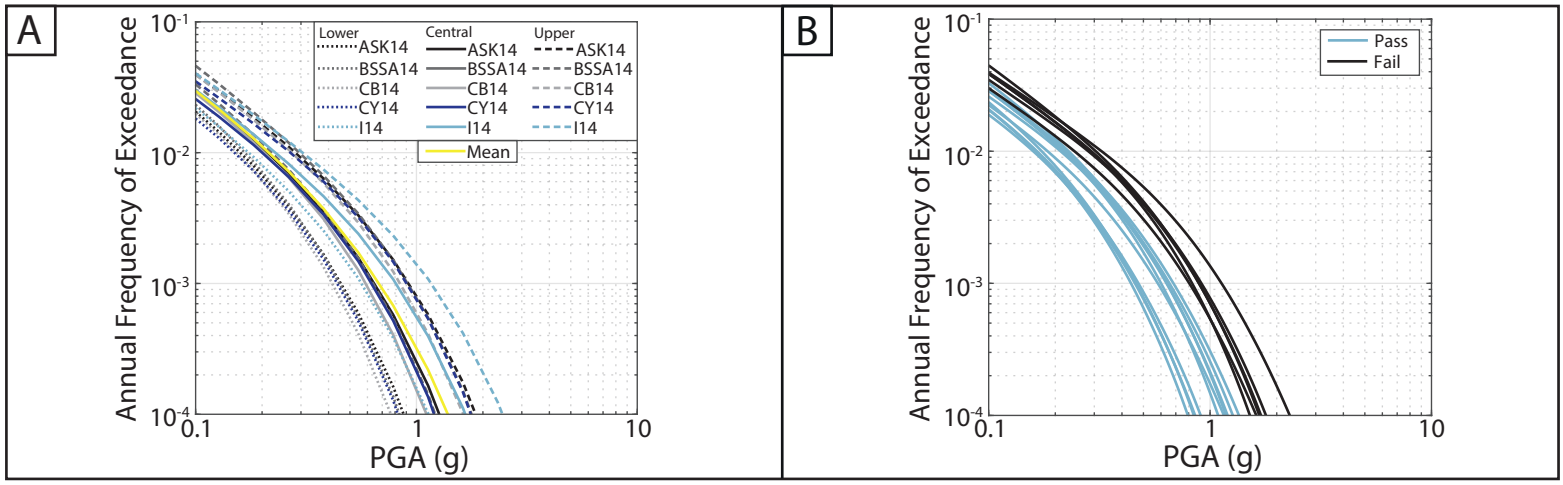

The dominant seismic sources for the GV2 site are the San Andreas fault, Cleghorn fault, San Jacinto fault, and North Frontal thrust faults. The combination of the relatively old fragility age and moderate fragility of GV2 cause the ground-motions estimated by the upper branches of all five GMMs and the central branch of I14 to be inconsistent with a 5% probability of survival of GV2. The removal of the I14 GMM, at 2475 year mean return period, reduces the mean ground-motion estimate by 4% and the reduces the range of estimated 5th–95th fractile ground motions by 27% at the GV2 site.

LB05

Fragility Results Figures

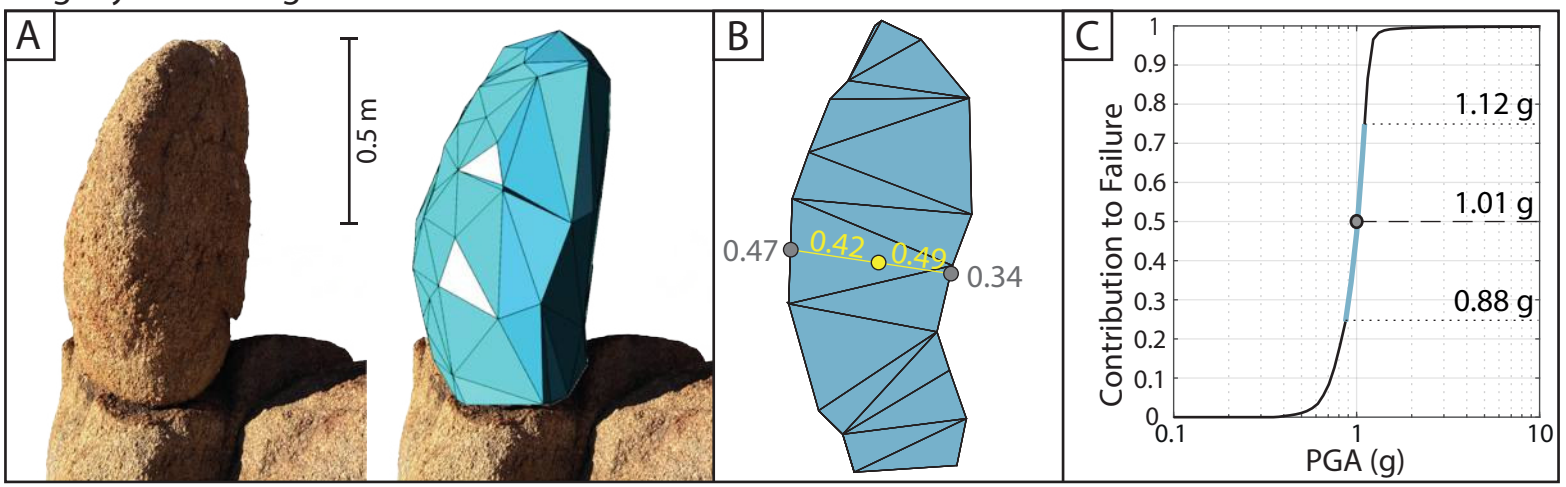

(A) One planar side of LB05 (right side in photos) may indicate significant mass loss, which would result in the LB05 geometry evolving at some unknown time before the present. However, there was no evidence of this lost material, e.g., a block, on the ground surface below the pedestal. The other three sides of LB05 are bound by joints that continue into the pedestal and surrounding outcrop. (B) The two alternative methods of selecting α_1 and α_2 produce near identical values, therefore, we are confident that the basal area of LB05 approximates the rectangular basal geometry that was described by the Purvance et al. (2008) fragility equations. α_2 is 1.39 times greater than α_1, so LB05 is classified as having an asymmetric rocking response.

Fragility Age Results Figures

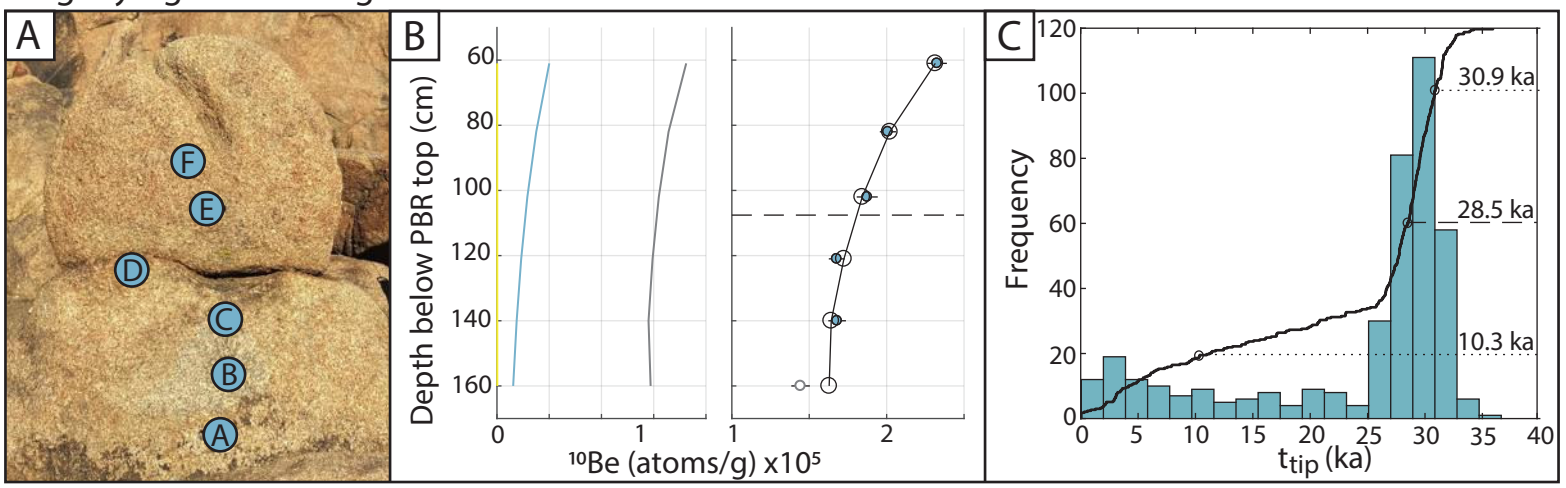

(A) Samples E & F are located on the PBR, and samples A-D are located on the pedestal. However, the dip of the PBR-pedestal contact means that sample D, although collected from the pedestal, is above the lowest point on the PBR-pedestal contact. (B) Sample A was excluded from the model fitting because field observations suggested the ground surface was recently lowered to expose the location of sample A. The recent removal of such material would have the effect of present shielding being to low and, therefore, the ^{10}Be production rate being to high. This underestimation of the shielding factor is supported by the forward model overpredicting the ^{10}Be concentration in A as a result of an erroneously high production rate for this sample. An instantaneous exhumation rate, ε_1, results in no ^{10}Be accumulation during exhumation (yellow line).

Hazard Validation Results Figures

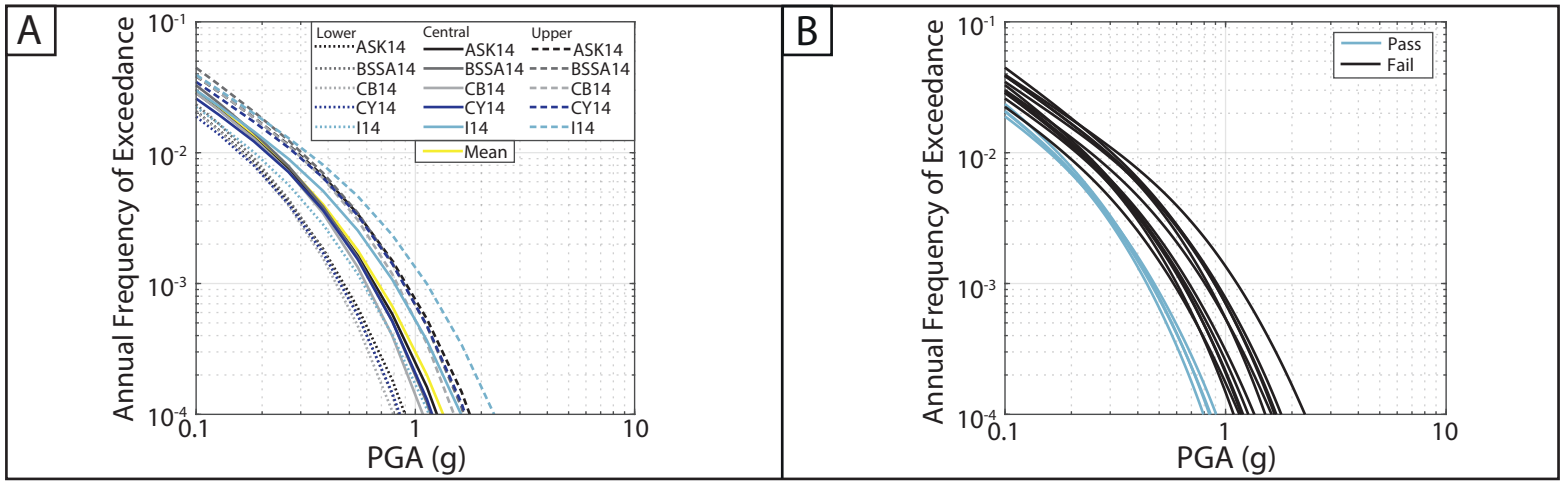

The dominant seismic source for the LB05 site is the San Andreas fault. The combination of the relatively old fragility age and moderate fragility of LB05 cause the upper and central branches of all five GMMs as well as the lower branch I14 to be inconsistent with a 5% probability of survival of LB05. The removal of the I14 GMM, at 2475 year mean return period, reduces the mean ground-motion estimate by 3% and the reduces the range of estimated 5th–95th fractile ground motions by 25% at the LB05 site.

LJ1

Fragility Results Figures

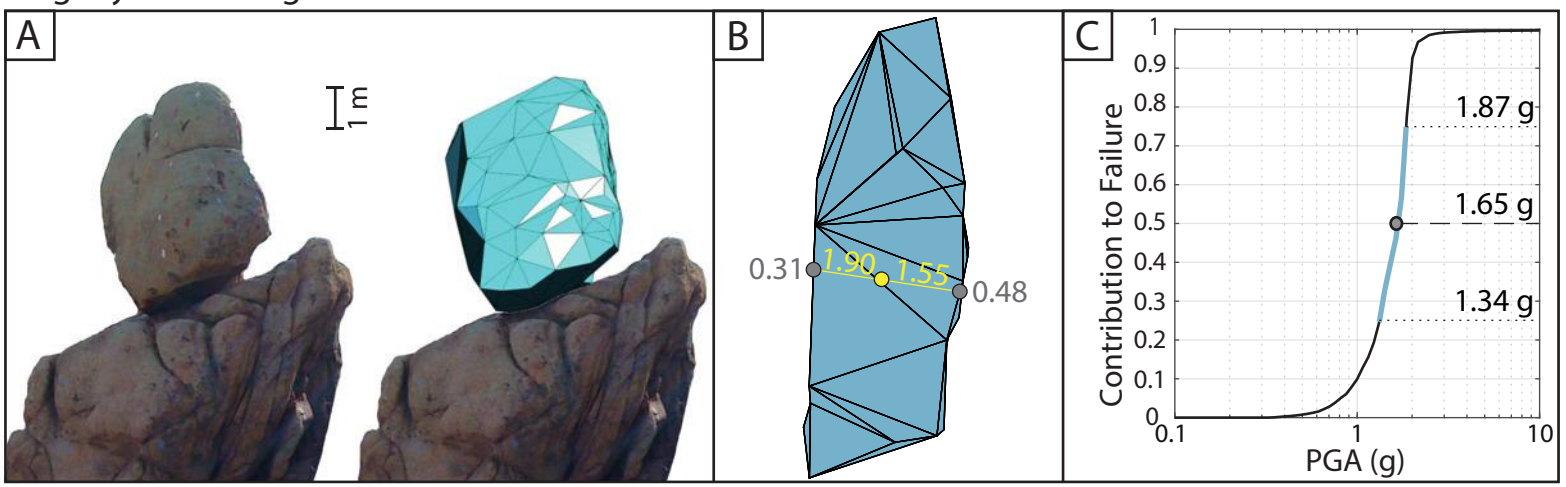

(A) LJ1 has the greatest height of our studied PBRs. The surface of LJ1 and its pedestal have a well-developed varnish and the sides are bound by joints that continue into the pedestal, which indicate the occurrence of negligible post-exhumation erosion. (B) The PBR-pedestal contact area is narrower than the maximum length and width of the PBR, therefore, LJ1 is more fragile than one might expect. The two alternative methods of selecting α_1 and α_2 produce near identical values, therefore, we are confident that the basal area of LJ1 approximates the rectangular basal geometry that was described by the Purvance et al. (2008) fragility equations. α_2 is 1.55 times greater than α_1, so LJ1 is classified as having an asymmetric rocking response.

Fragility Age Results Figures

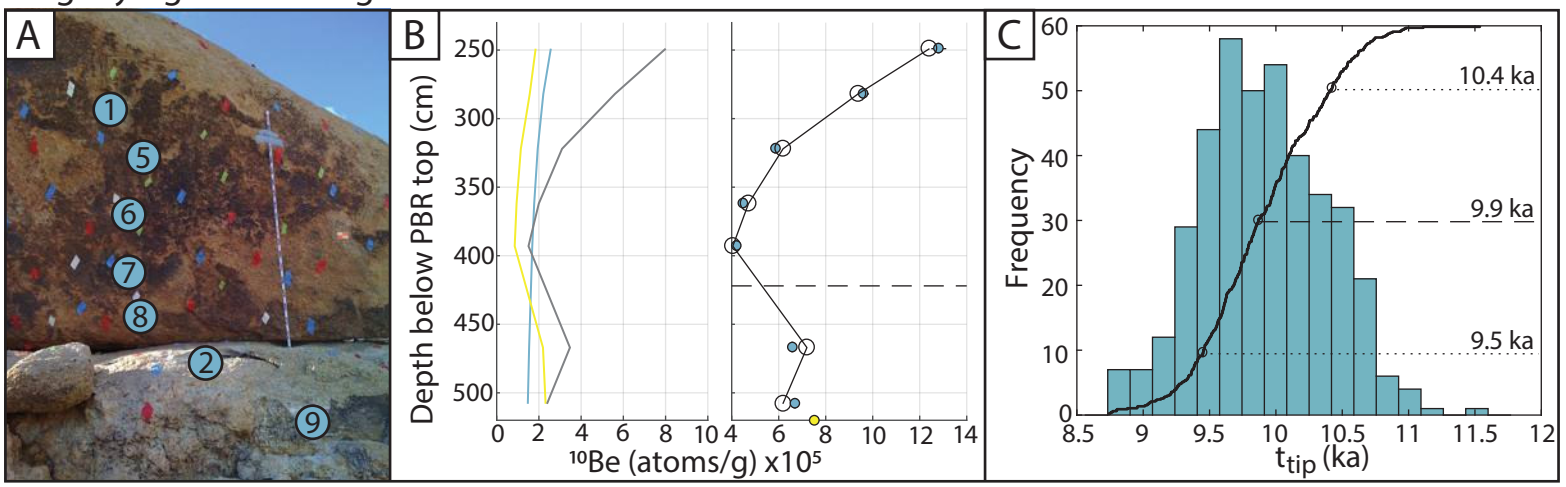

A) Samples 1 and 5 - 8 are located on the PBR and samples 2 and 9 are located on the pedestal. (B) The fact that all the samples were not collected from a planar surface, but instead curve around onto the pedestal, results in the shape of the post-exhumation profile of ^{10}Be production with sample depth (gray line) to be distinct from the pre-exhumation ^{10}Be production with sample depth (blue line). The saprolite sample was collected on the ground surface ~2 m below sample 9, on the opposite side of the outcrop from the PBR-pedestal sample profile. The shielding, and so the ^{10}Be production rate, is different for the saprolite sample than the PBR-pedestal samples. Therefore, the measured ^{10}Be concentration in the saprolite sample is only expected to be within the range of concentrations, which is what is observed and validates the model and its results.

Hazard Validation Results Figures

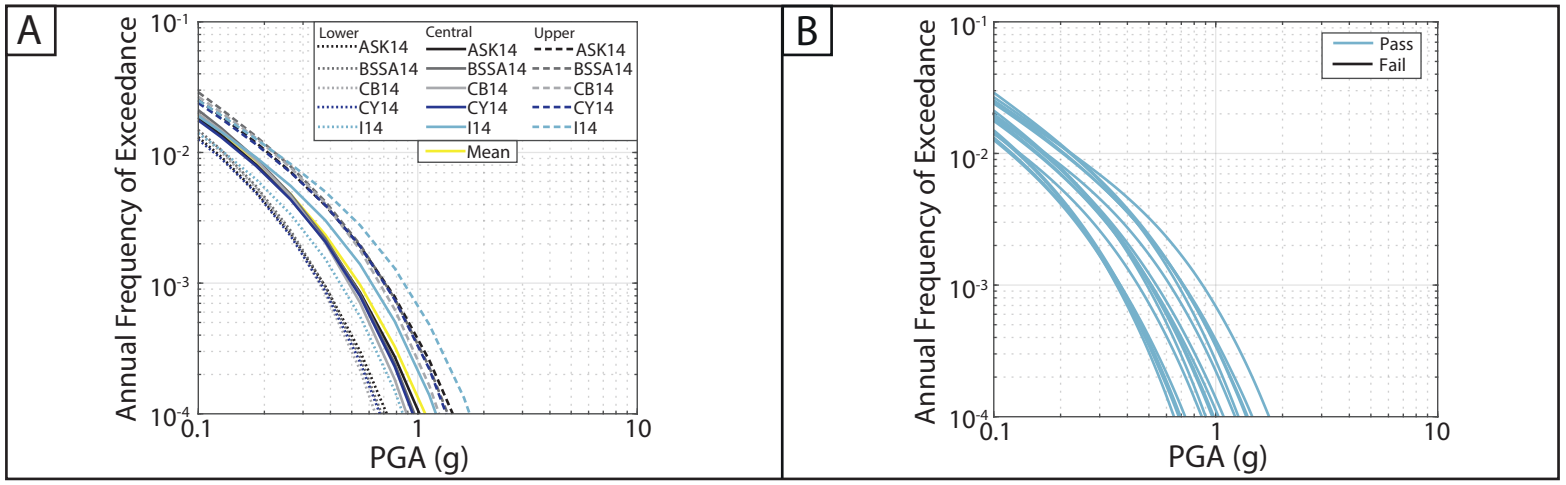

The dominant seismic source for the LJ1 site is the San Andreas fault. The combination of the relatively old fragility age and moderate fragility of LJ1 cause none of the three branches (upper, central, and lower) of all five GMMs to be inconsistent with a 5% probability of survival of LJ1. The removal of the I14 GMM, at 2475 year mean return period, reduces the mean ground-motion estimate by 3% and the reduces the range of estimated 5th–95th fractile ground motions by 25% at the LJ1 site.

LJ5

Fragility Results Figures

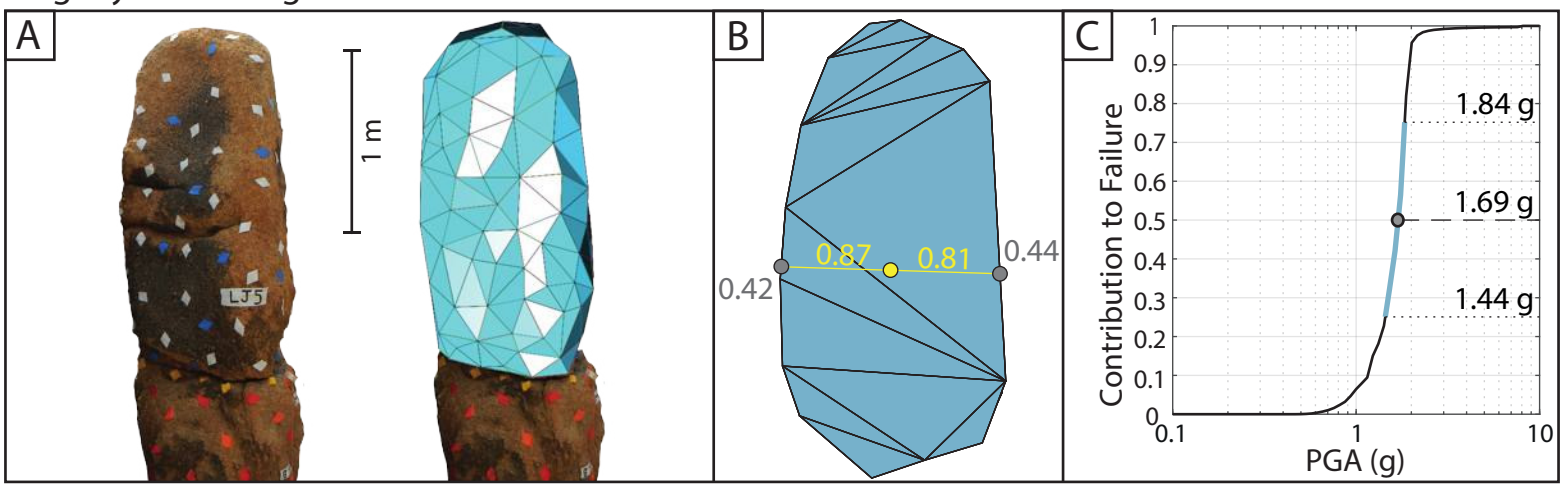

(A) LJ5 has extensive well-developed varnish on its surface, and the joints that bound the PBR align with the joints that bound the pedestal. We, therefore, have confidence that LJ5 was exhumed with its current geometry and since that time little post-exhumation erosion has occurred. (B) The two alternative methods of selecting α_1 and α_2 produce identical critical rocking points, therefore, we are confident that the basal area of LJ5 approximates the rectangular basal geometry that was described by the Purvance et al. (2008) fragility equations. However, its rocking response will be impeded by the outcrop in the direction of α_2. In addition, α_2 is 1.05 times greater than α_1, so LJ5 is classified as having a symmetric rocking response. LJ5 is the only PBR with a symmetric geometry that we studied.

Fragility Age Results Figures

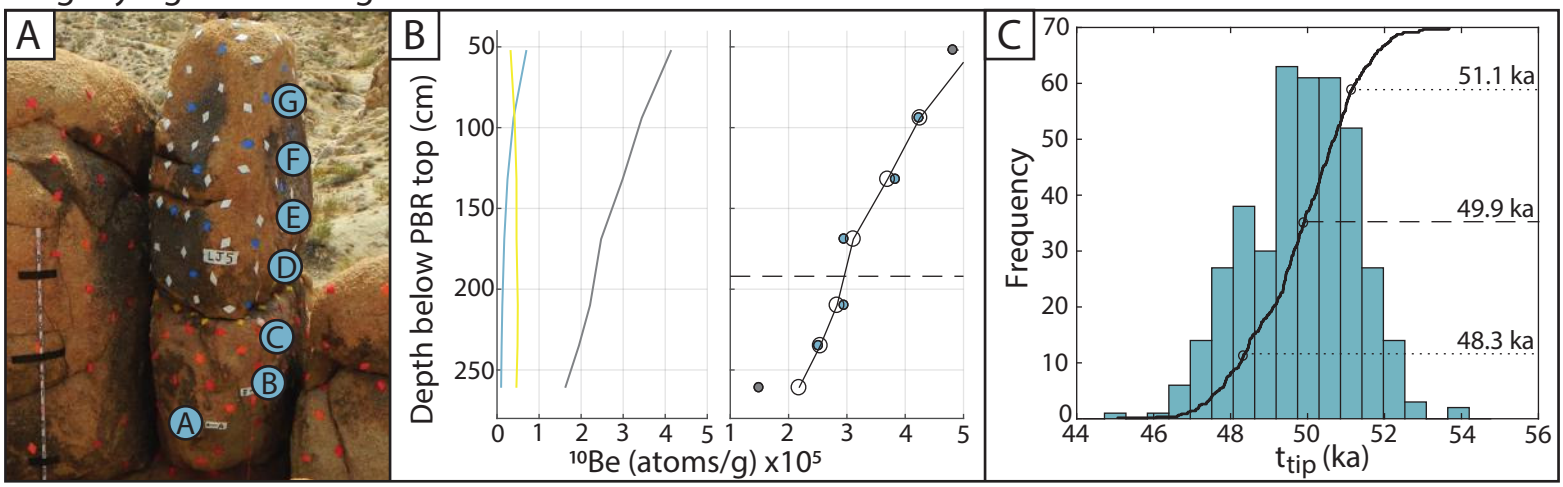

(A) Samples D - G are located on the PBR and samples A - C are located on the pedestal. (B) Sample A was excluded from the model fitting because field observations suggested that its position may have had a different exhumation history because it is located on a different side of the pedestal and adjacent to the modern saprolite surface. The overprediction of the modeled ^{10}Be concentration in sample A would be consistent with this sample location being shielded by saprolite for some duration of time after the other samples were exhumed. LJ5 is the oldest PBR we studied and so has a large component of post-exhumation ^{10}Be production (gray line). Low ε_0 erosion rates and an increased but still low ε_1 exhumation rate result in both pre-exhumation (blue line) and during-exhumation (yellow line) ^{10}Be production.

Hazard Validation Results Figures

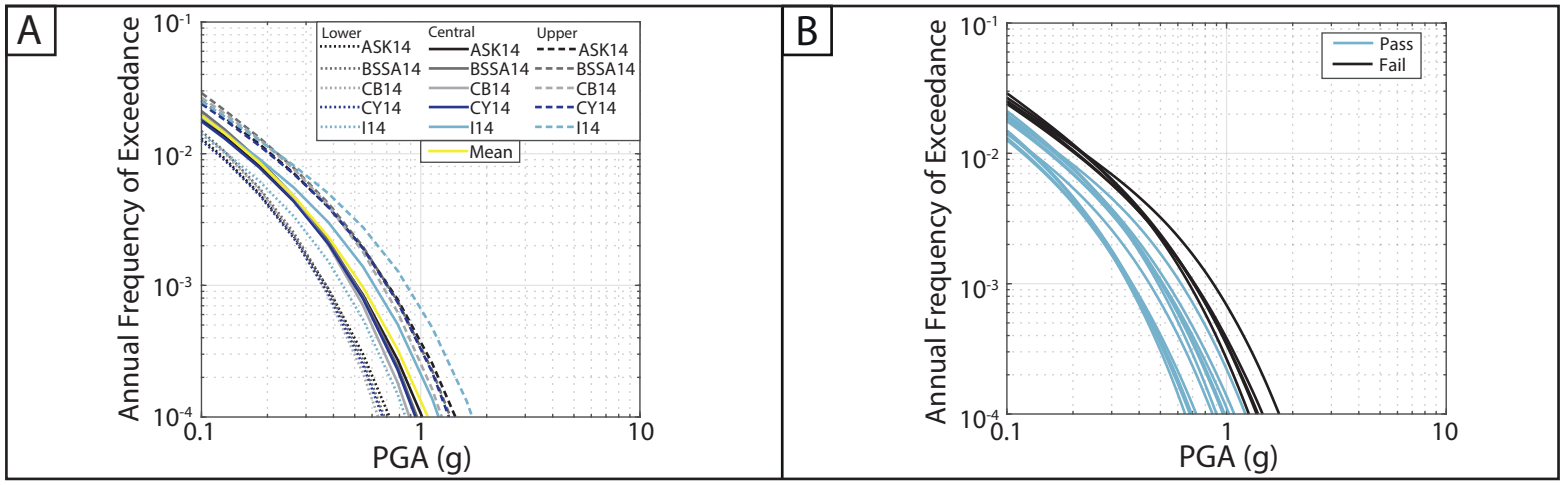

The dominant seismic source for the LJ5 site is the San Andreas fault. The combination of the old fragility age and relatively stable fragility of LJ5 causes the ground-motions estimated by the upper branches of all five GMMs to be inconsistent with a 5% probability of survival of LJ5. The removal of the I14 GMM, at 2475 year mean return period, reduces the mean ground-motion estimate by 3% and the reduces the range of estimated 5th–95th fractile ground motions by 25% at the LJ5 site.

LJB1

Fragility Results Figures

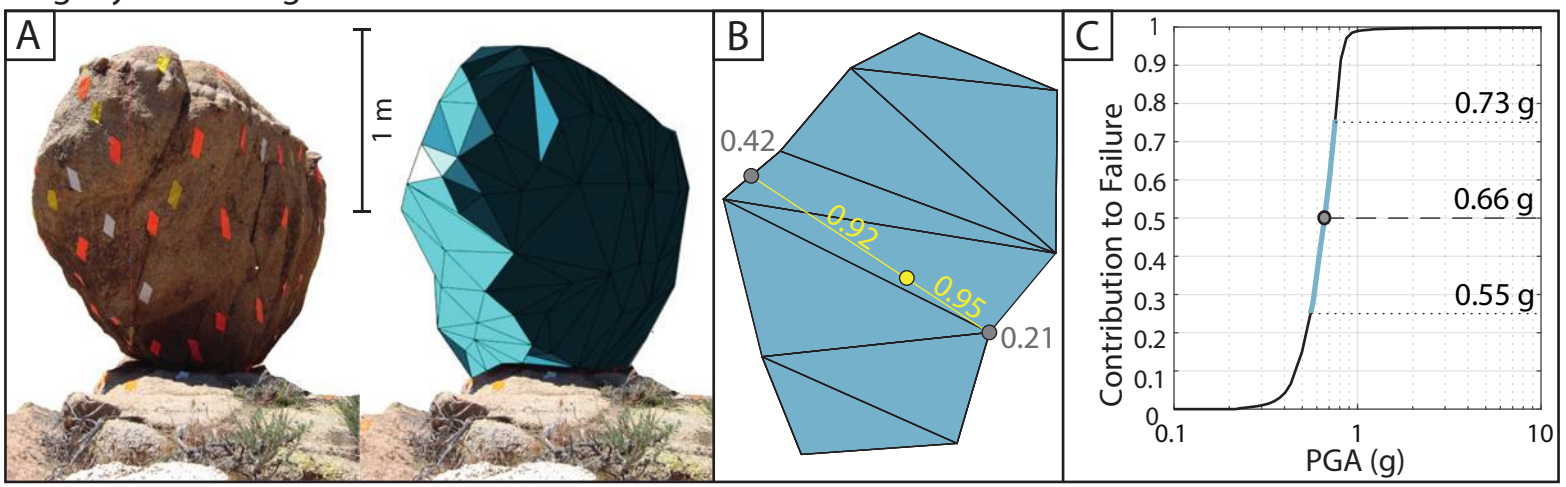

(A) The inclined dip of the pedestal, in the direction approximately perpendicular to the 2-D rocking direction of LJB1, suggests that sliding could be a potential failure mechanism of LJB1 in addition to rocking leading to toppling. (B) The two alternative methods of selecting α_1 and α_2 produce identical critical rocking points, therefore, we are confident that the basal area of LJB1 approximates the rectangular basal geometry that was described by the Purvance et al. (2008) fragility equations. In addition, α_2 is 2.00 times greater than α_1, so LJB1 is classified as having an symmetric rocking response.

Fragility Age Results Figures

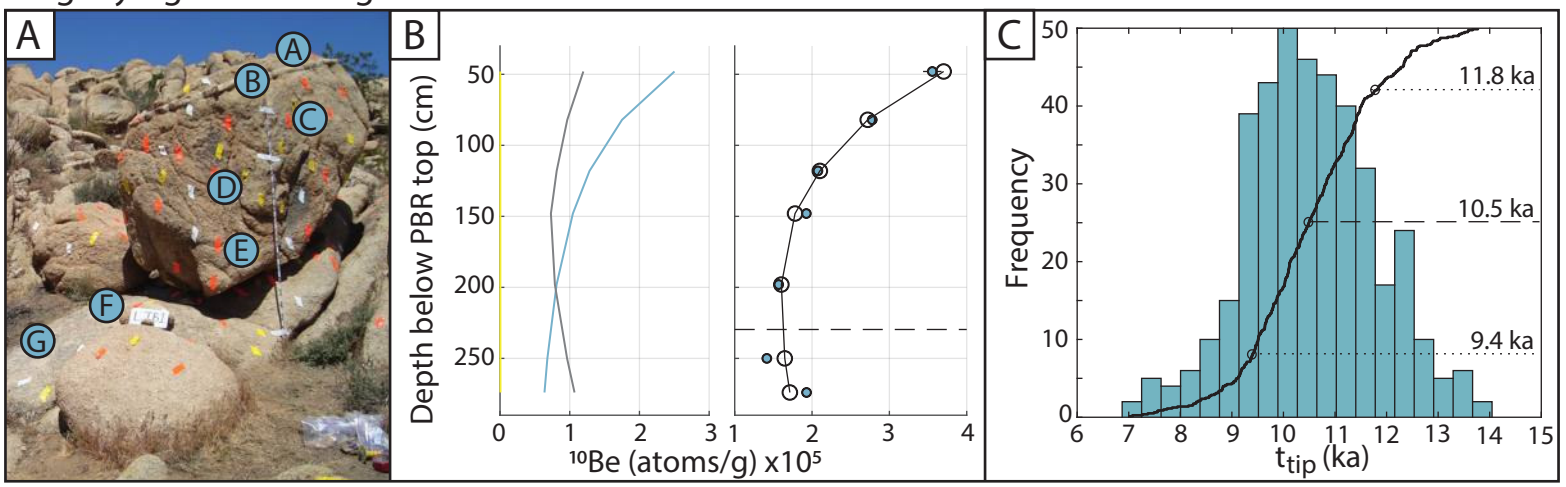

(A) Samples A - E are located on the PBR and samples F and G are located on the pedestal. (B) The modeled ε_1 erosion rate results in an instantaneous exhumation of LJB1, therefore, no ^{10}Be production occured during exhumation (yellow line). The higher measured ^{10}Be concentration in sample G than in sample F suggests the potential recent removal of material that was shielding the location of sample F.

Hazard Validation Results Figures

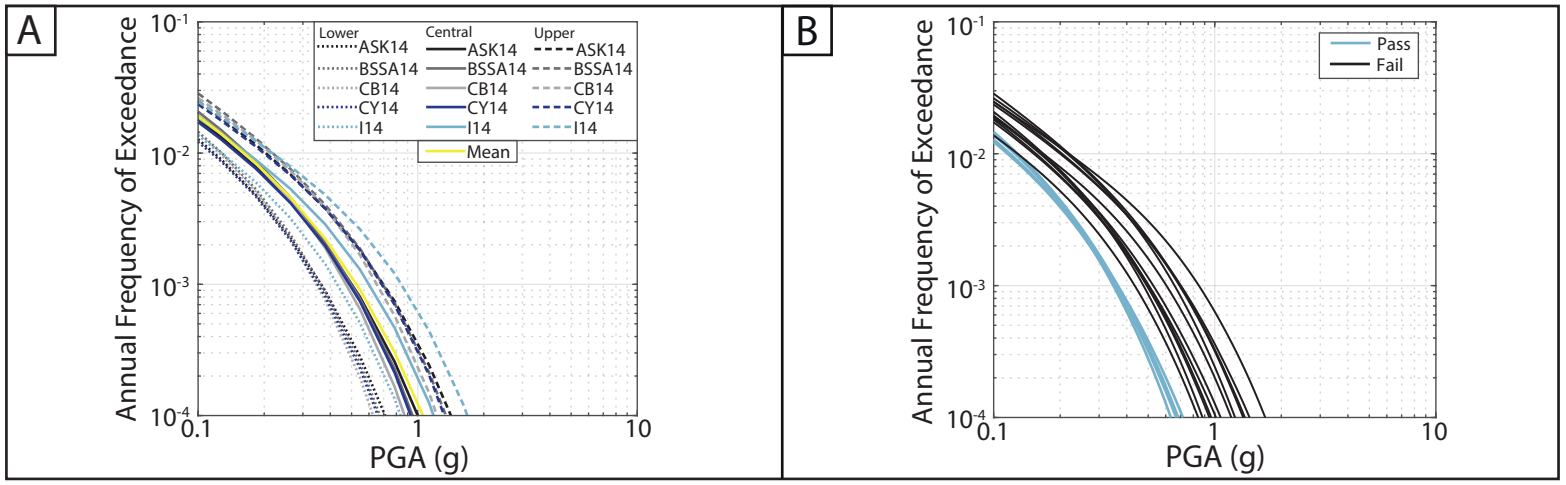

The dominant seismic source for the LJB1 site is the San Andreas fault. The combination of the moderate fragility age and relatively unstable fragility of LJB1 cause the upper and central branches of all five GMMs as well as the lower branch I14 to be inconsistent with a 5% probability of survival of LJB1. The removal of the I14 GMM, at 2475 year mean return period, reduces the mean ground-motion estimate by 3% and the reduces the range of estimated 5th–95th fractile ground motions by 24% at the LJB1 site.

LJB2

Fragility Results Figures

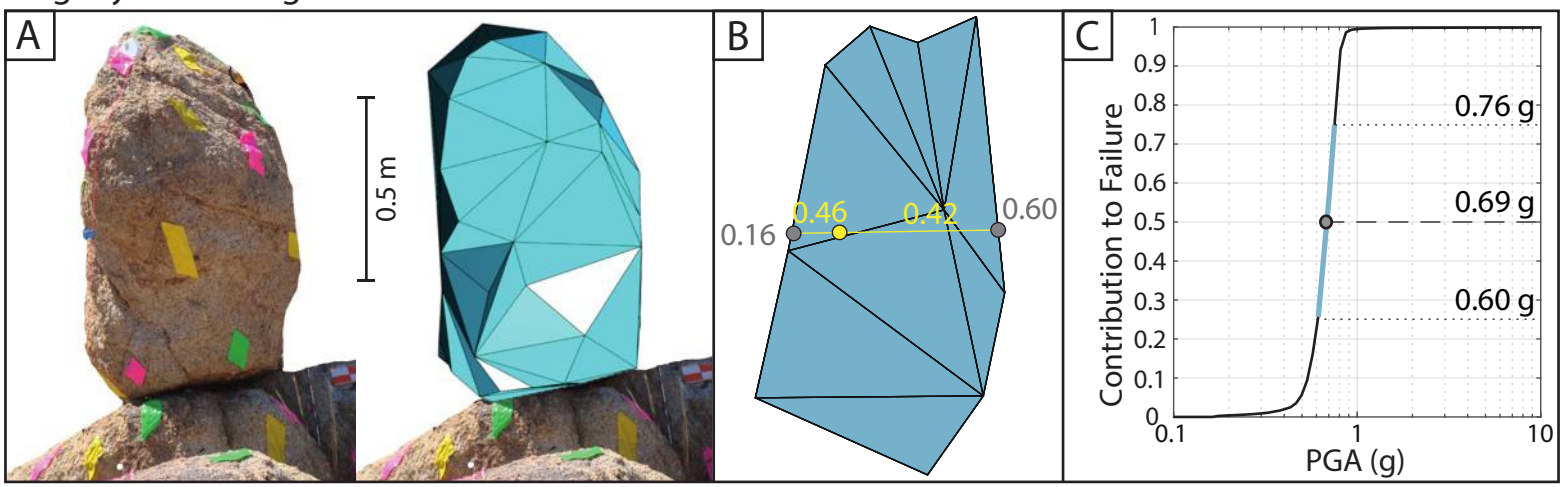

(A) The surface of LJB2 has localized varnish and the sides are bounded by joints that continue into the pedestal, which suggest the occurrence of negligible post-exhumation erosion. (B) The two alternative methods of selecting α_1 and α_2 produce similar critical rocking points, therefore, we are confident that the basal area of LJB2 approximates the rectangular basal geometry that was described by the Purvance et al. (2008) fragility equations. In addition, α_2 is 3.72 times greater than α_1, so LJB2 is classified as having an asymmetric rocking response. LJB2 is the most asymmetric PBR we studied, which is primarily due to the dip of the pedestal. In addition, the α_2 of LJB2 is greater than the range investigated by Purvance et al. (2008), which reduces our confidence in the fragility characterization of LJB2.

Fragility Age Results Figures

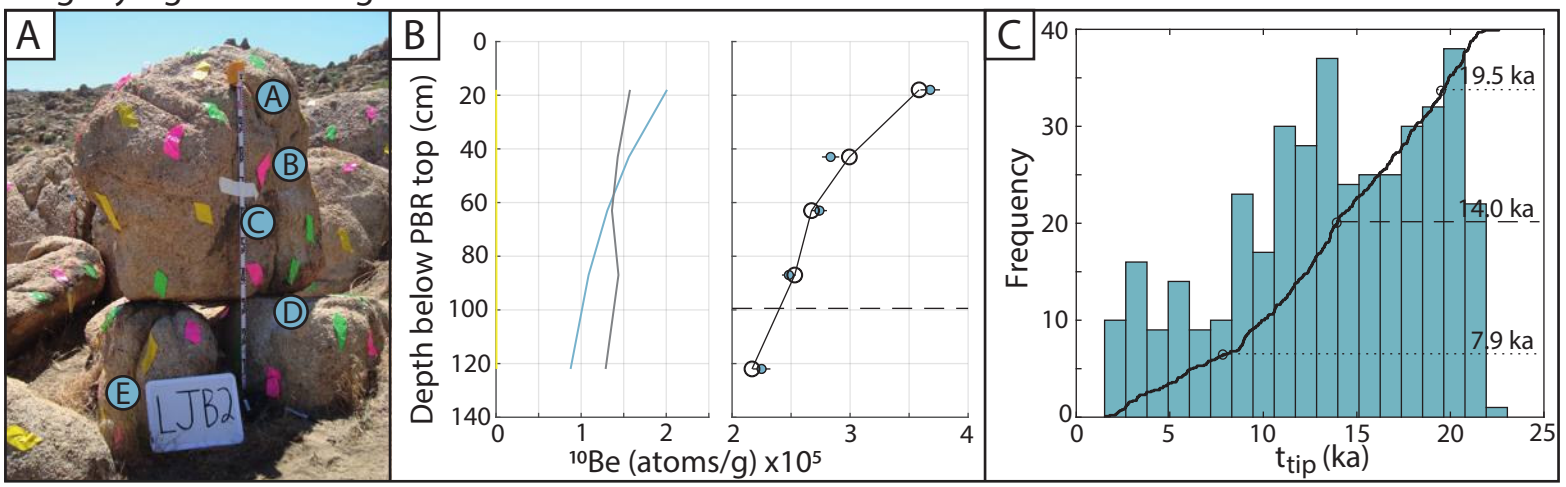

(A) Samples A - C are located on the PBR, and samples D and E are located on the pedestal. (B) Due to the dip of the PBR-pedestal contact, sample D is above the lowest point on the PBR-pedestal contact (horizontal dashed line). (C) The forward model predicts a non-unique ttip age for LJB2, ranging from ~2 - 22 ka. The median ttip age and best estimate value are in good agreement, however, the ambiguous model results give us only moderate confidence in the fragility age of LJB2.

Hazard Validation Results Figures

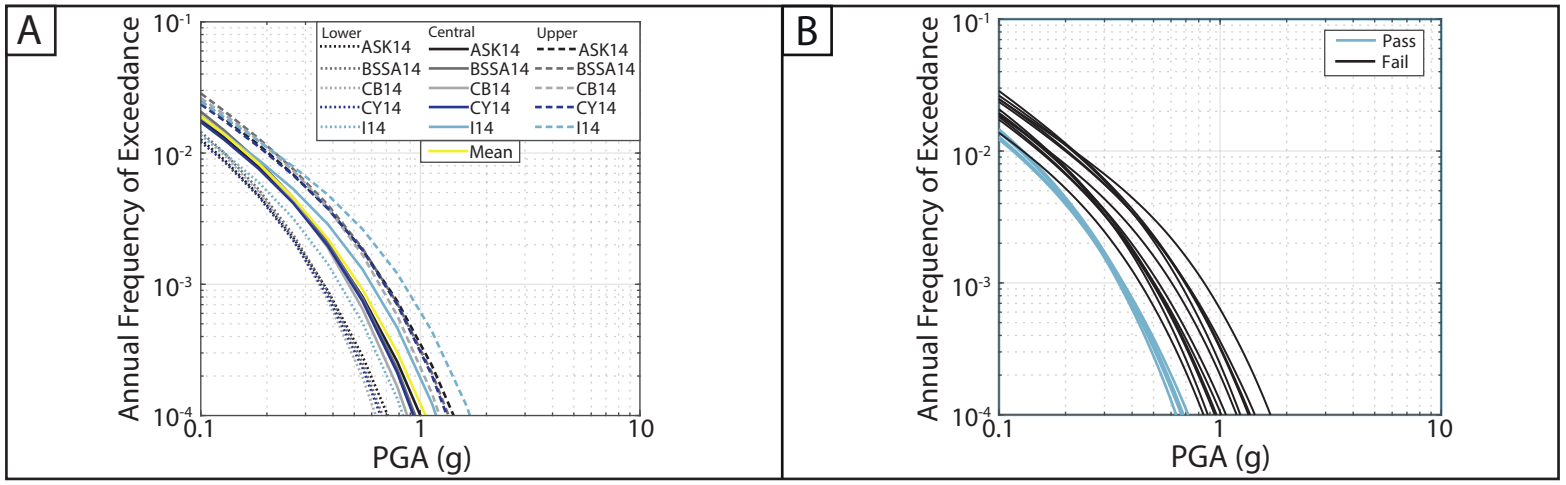

The dominant seismic source for the LJB2 site is the San Andreas fault. The combination of the moderate fragility age and relatively unstable fragility of LJB2 cause the upper and central branches of all five GMMs as well as the lower branch I14 to be inconsistent with a 5% probability of survival of LJB2. The removal of the I14 GMM, at 2475 year mean return period, reduces the mean ground-motion estimate by 3% and the reduces the range of estimated 5th–95th fractile ground motions by 24% at the LJB2 site.

MR1

Fragility Results Figures

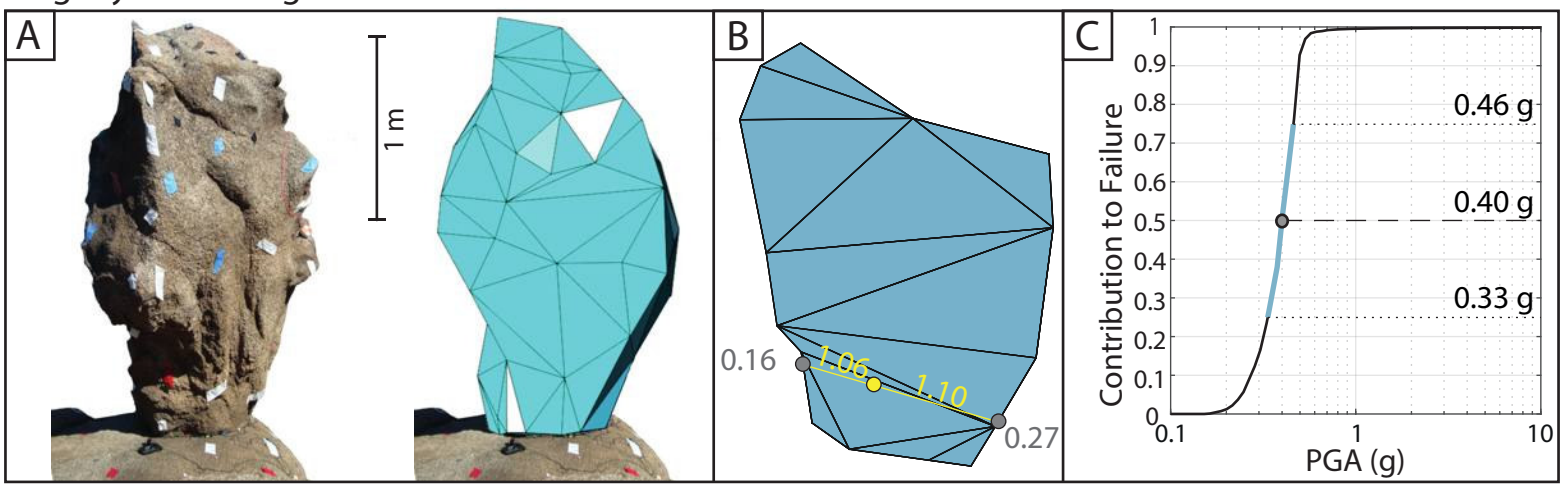

(A) One planar side of MR1 (left side in photo) may indicate significant mass loss, which would result in the MR1 geometry evolving at some unknown time before the present. However, there was no evidence of a block on the ground surface below the pedestal. (B) The alternative method of selecting the minimum α rocking point and corresponding α_2 rocking point 180 degrees through the center of mass (not shown) results in α_1 and α_2 values of 0.14 and 0.59, respectively, which are located on the two sides of the PBR than do not contain the narrowest base critical rocking points (gray circles). Therefore, we have low confidence that the rocking response of MR1 is described by the selected critical rocking points and Purvance et al. (2008) fragility equations. α_2 is 1.70 times greater than α_1, so MR1 has an asymmetric rocking response.

Fragility Age Results Figures

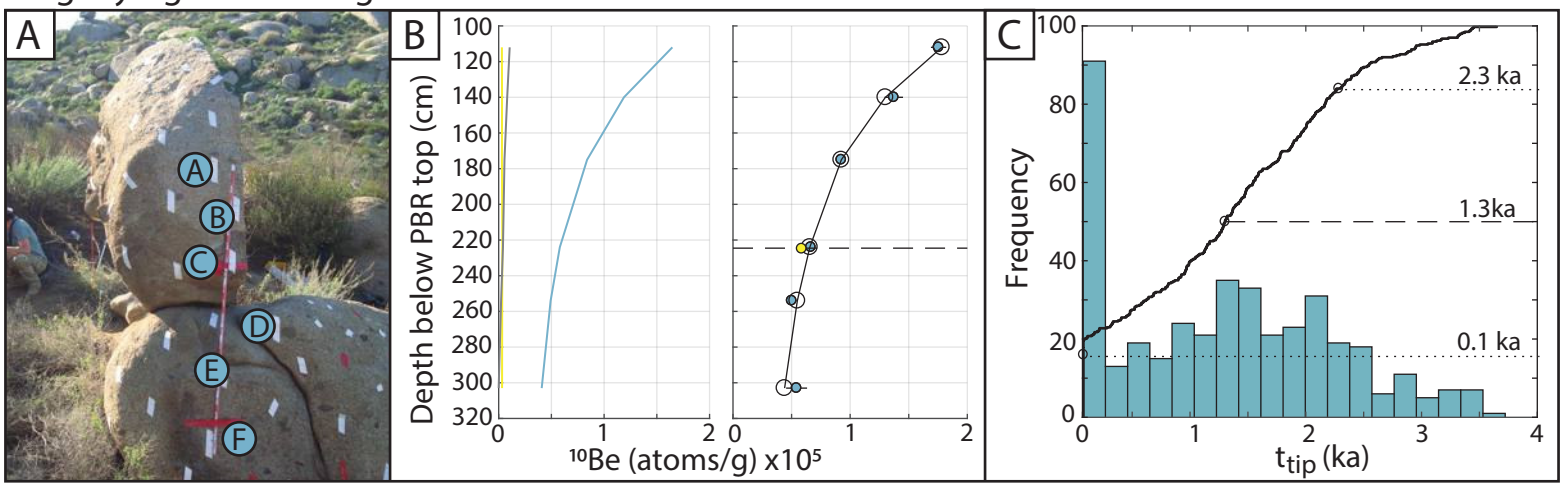

(A) Samples A - C are located on the PBR and samples D - F are located on the pedestal. (B) The saprolte sample collected at this site was collected at approximately the height of the PBR-pedestal contact. The measured ^{10}Be concentration in the saprolite sample (yellow circle) matches the concentration predicted by the forward model, validating the model and its results. (C) MR1 is one of the youngest PBRs we studied, and its t_{tip} age is not well constrained, so we have low confidence in its fragility age. This uncertain t_{tip} age results from the poorly constrained free-parameter ε_1 , for which the 16th - 84th percentile uncertainty range is ~400 - ~10,000 m/Myr. We propose that this ε_1 uncertainty range is because the majority of modeled ^{10}Be production occurred pre-exhumation (blue line) and so the small proportion of during-exhumation (yellow line) and post-exhumation (gray line) production is difficult to constrain.

Hazard Validation Results Figures

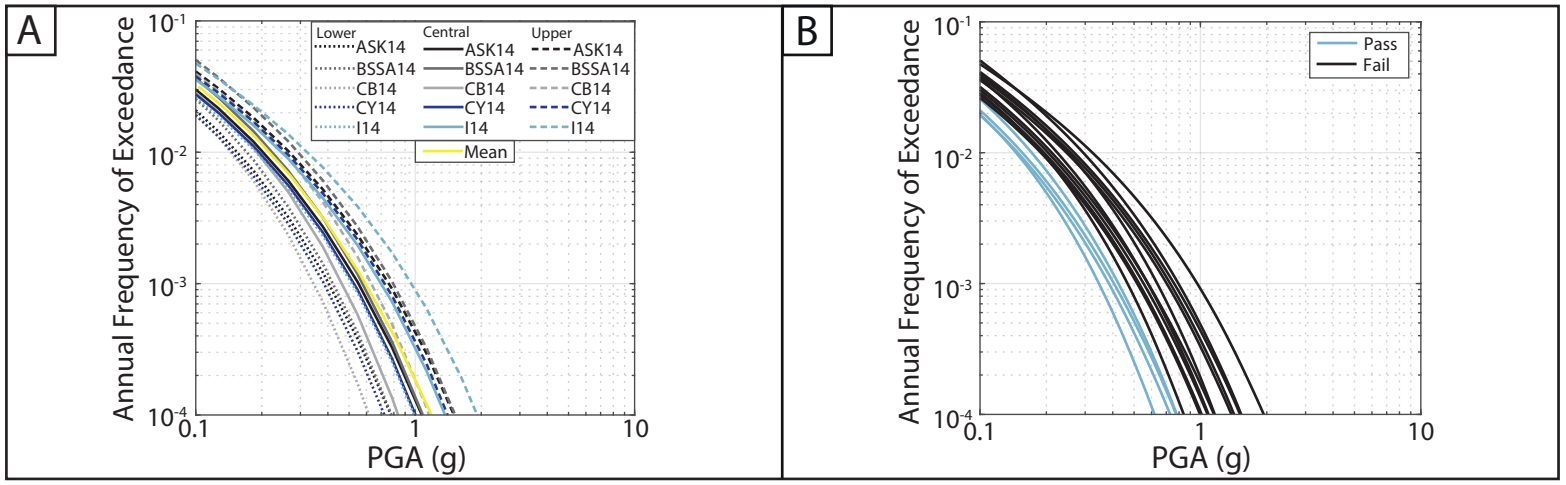

MR1 is located between the San Jacinto and Elsinore faults, which are the dominant seismic sources controlling the seismicity at the site. The young fragility age and unstable fragility of MR1 cause the upper and central branches of all five GMMs as well as the lower branch I14 to be inconsistent with a 5% probability of survival of MR1. The removal of the I14 GMM, at 2475 year mean return period, reduces the mean ground-motion estimate by 5% and the reduces the range of estimated 5th–95th fractile ground motions by 24% at the MR1 site.

PC1

Fragility Results Figures

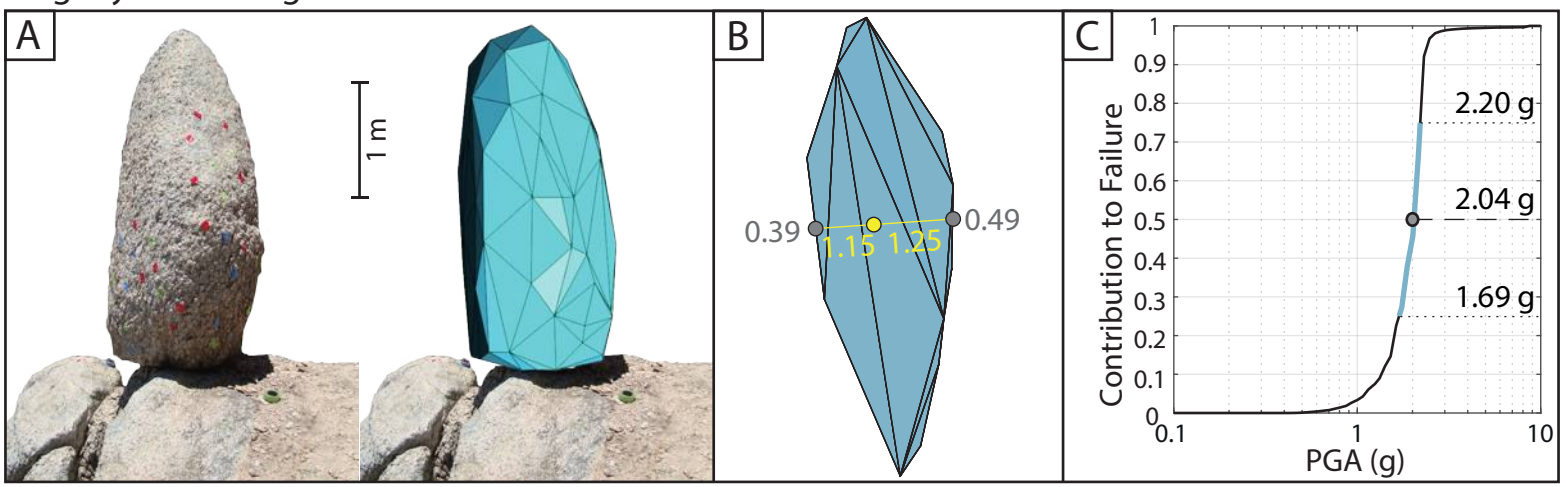

(A) PC1 and the surrounding outcrop show evidence of intense chemical weathering, which makes it much more susceptible to post-exhumation erosion. The rock-mass is easily disaggregated by hand. However, there is localized varnish and one side (left side in photo) is a planar surface that is formed by a joint that bounds the PBR and continues into the pedestal, which suggests limited post-exhumation erosion on some, but not all, PBR surfaces. (B) The two alternative methods of selecting α_1 and α_2 produce near identical values, therefore, we are confident that the basal area of PC1 approximates the rectangular basal geometry that was described by the Purvance et al. (2008) fragility equations. α_2 is 1.27 times greater than α_1, so PC1 is classified as having an asymmetric rocking response.

Fragility Age Results Figures

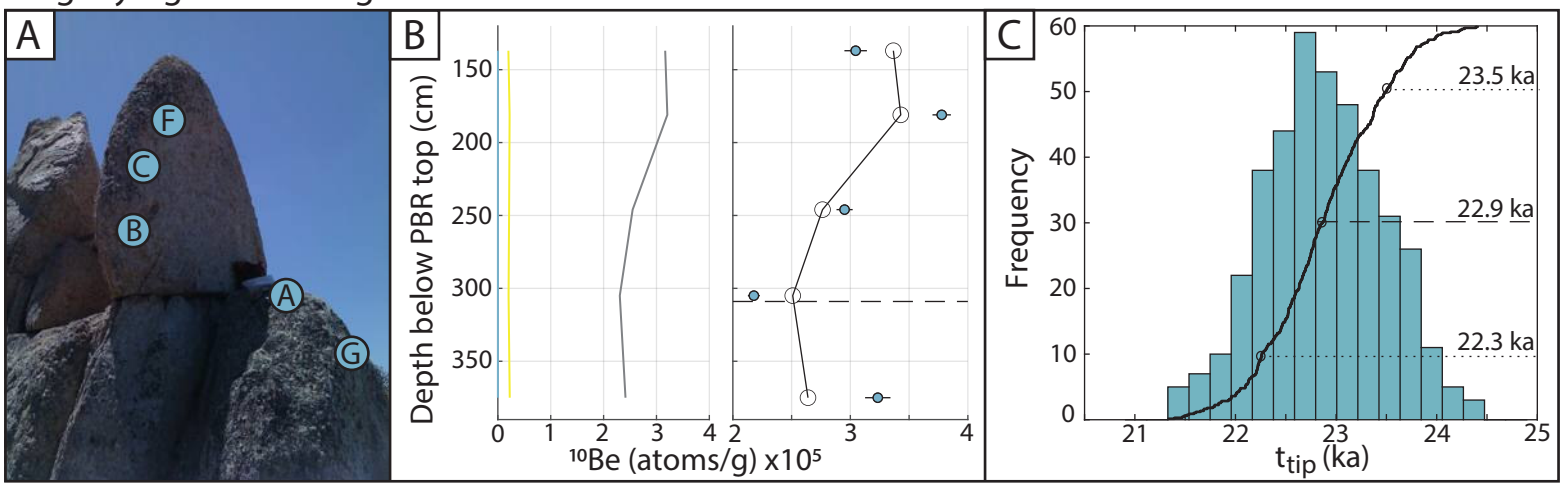

(A) Samples B, C, and F are located on the PBR and samples A and G are located on the pedestal. (B) Due to the dip of the PBR-pedestal contact, sample A is above the lowest point on the PBR-pedestal contact (horizontal dashed line). (B) The best-fitting free parameters have a high misfit (fval) and none of the measured ^{10}Be concentrations overlap with the modeled concentrations. PC1 has an instantaneous best fit ε_0 value, which we believe suggest that the ε_0 signal has been completely removed during the ε_1 phase of exhumation, and so ε_0 is an unconstrained parameter for PC1. Alternatively, the occurrence of post-exhumation erosion would violate the assumptions of our geomorphic model, therefore, we cannot be confident in the modeled fragility age of PC1.

Hazard Validation Results Figures

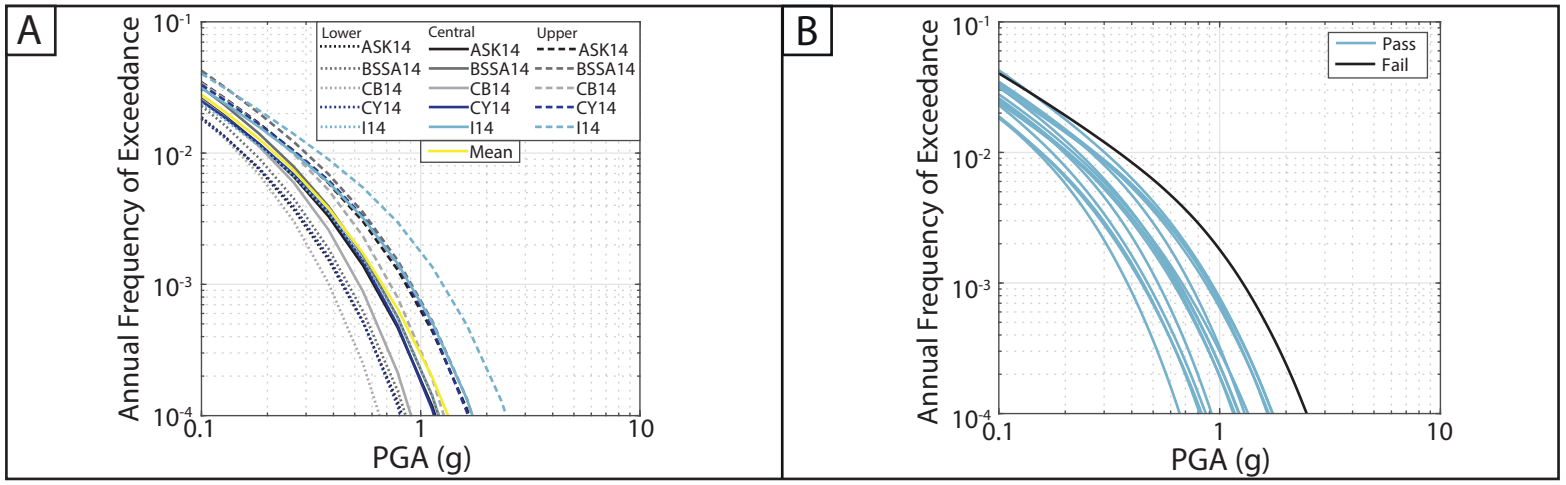

The dominant seismic source for the PC1 site is the San Andreas fault. The combination of the relatively old fragility age and relatively stable fragility of PC1 causes the ground-motions estimated by the upper branch of I14 to be inconsistent with a 5% probability of survival of PC1. The removal of the I14 GMM, at 2475 year mean return period, reduces the mean ground-motion estimate by 7% and the reduces the range of estimated 5th–95th fractile ground motions by 36% at the PC1 site.

PI1

Fragility Results Figures

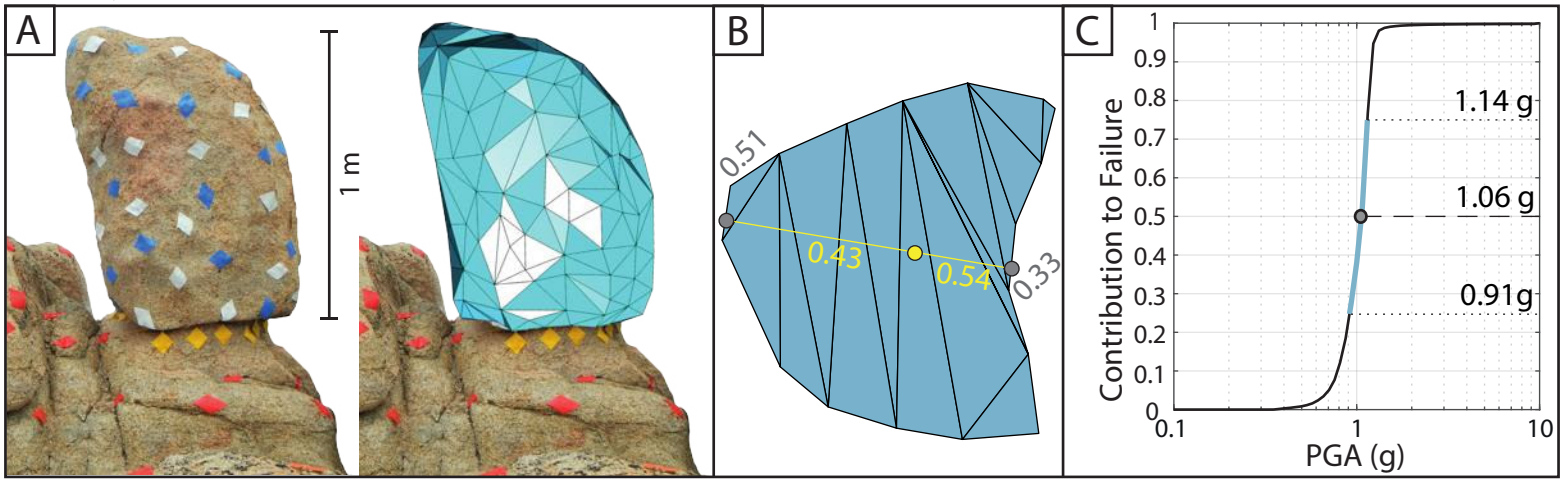

(A) PI1 is clearly bounded on all sides by joints that continue into the pedestal and surrounding outcrop, which indicates that the PBR was exhumed in its current geometry and that negligible post-exhumation erosion has occurred. (B) The two alternative methods of selecting α_1 and α_2 produce near identical values, therefore, we are confident that the basal area of PI1 approximates the rectangular basal geometry that was described by the Purvance et al. (2008) fragility equations. The fragility of PI1 is increased by the undercutting of the PBR base in the most fragile direction. α_2 is 1.54 times greater than α_1, so PI1 is classified as having an asymmetric rocking response. However, the α_2 of PI1 is greater than the range investigated by Purvance et al. (2008), which reduces our confidence in the fragility characterization of PI1.

Fragility Age Results Figures

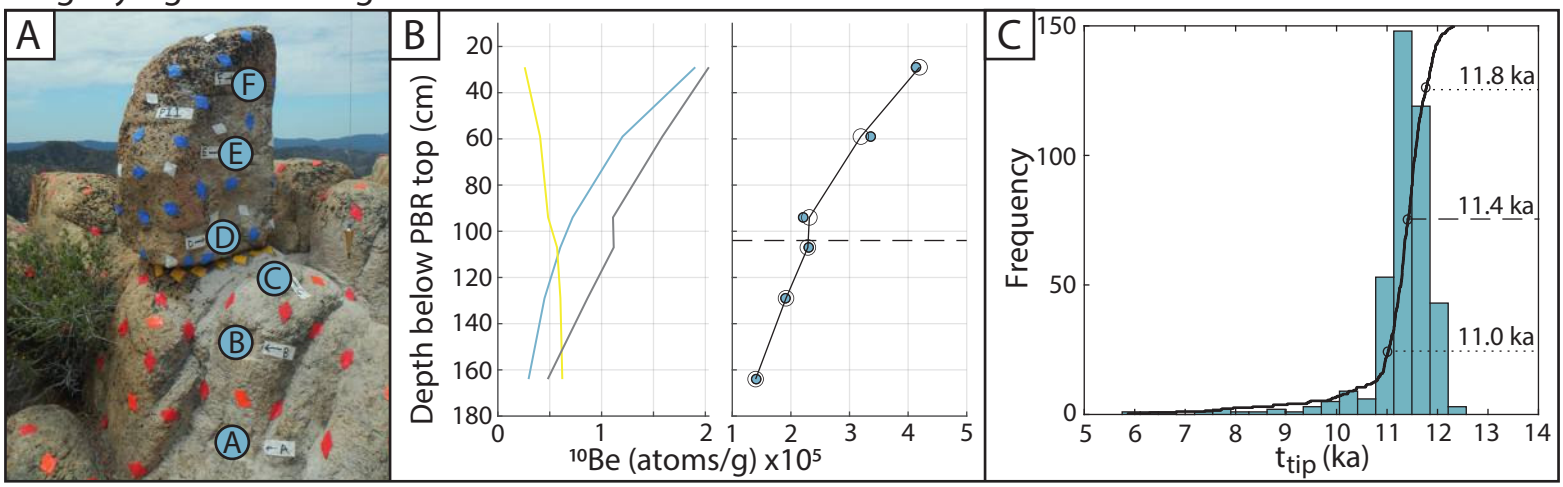

(A) Samples D - F are located on the PBR and samples A - C are located on the pedestal. (B) The low modeled ε_0 and higher, but still low, ε_1 result in ^{10}Be accumulation both before and during exhumation (blue and yellow lines, respectively). The samples collected down two sides of the outcrop result in a distinctive change in shielding and, therefore, associated profile of post-exhumation ^{10}Be production (gray line), between the two sides.

Hazard Validation Results Figures

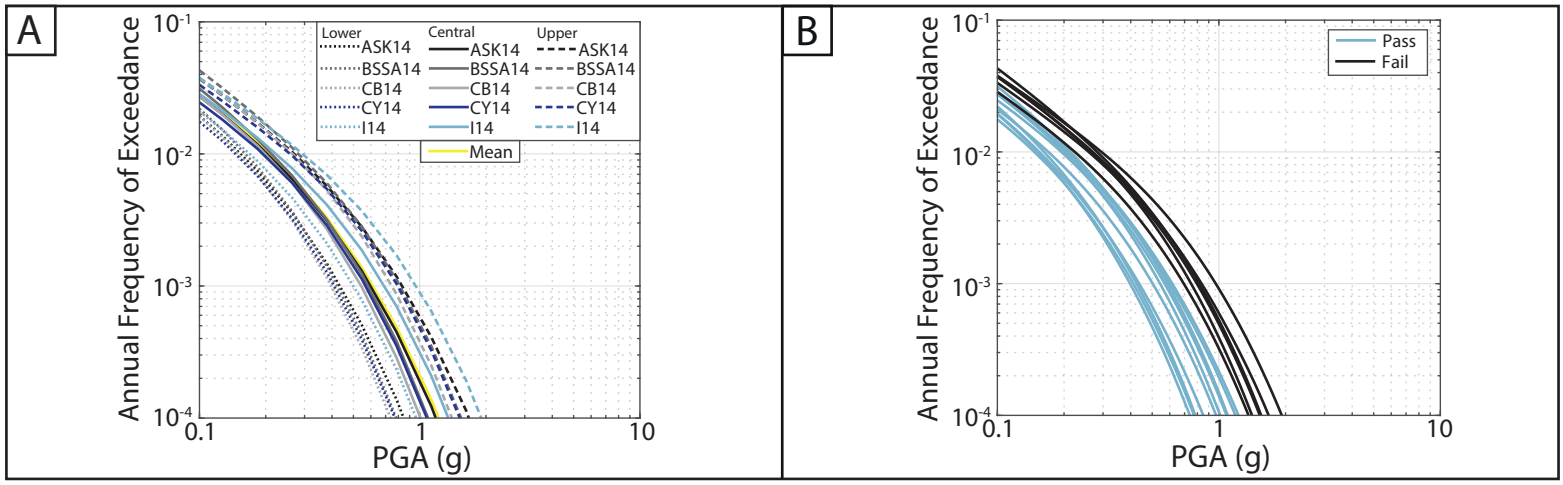

The dominant seismic sources at the PI1 site are the San Andreas fault, Cleghorn fault, San Jacinto fault, and North Frontal thrust faults. The combination of the moderate fragility age and moderate fragility of PI1 causes the ground-motions estimated by the upper branches of all five GMMs and the central branch of I14 to be inconsistent with a 5% probability of survival of PI1. The removal of the I14 GMM, at 2475 year mean return period, reduces the mean ground-motion estimate by 3% and the reduces the range of estimated 5th–95th fractile ground motions by 17% at the PI1 site.

PI2

Fragility Results Figures

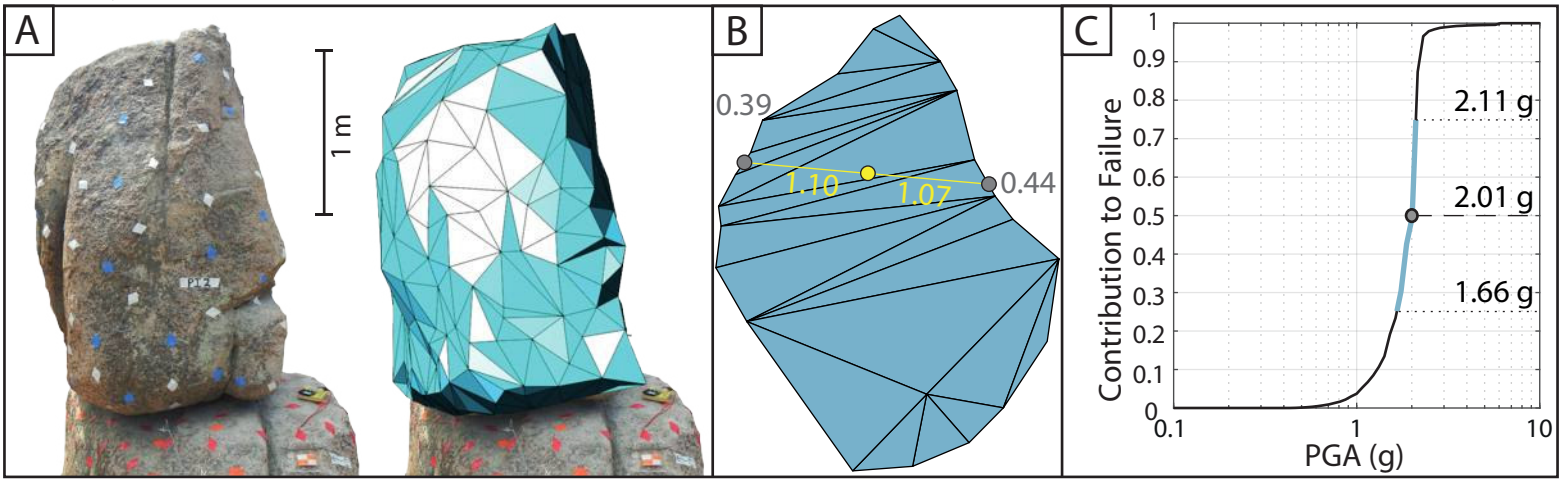

(A) PI2 is clearly bounded on all sides by joints that continue into the pedestal and surrounding outcrop, which indicates that the PBR was exhumed in its current geometry and that negligible post-exhumation erosion has occurred. (B) The two alternative methods of selecting α_1 and α_2 produce a moderate 13% and 18% difference, respectively. Therefore, we only have moderate confidence that the basal area of PI2 approximates the rectangular basal geometry that was described by the Purvance et al. (2008) fragility equations. α_2 is 1.15 times greater than α_1, so PI2 is classified as having an asymmetric rocking response.

Fragility Age Results Figures

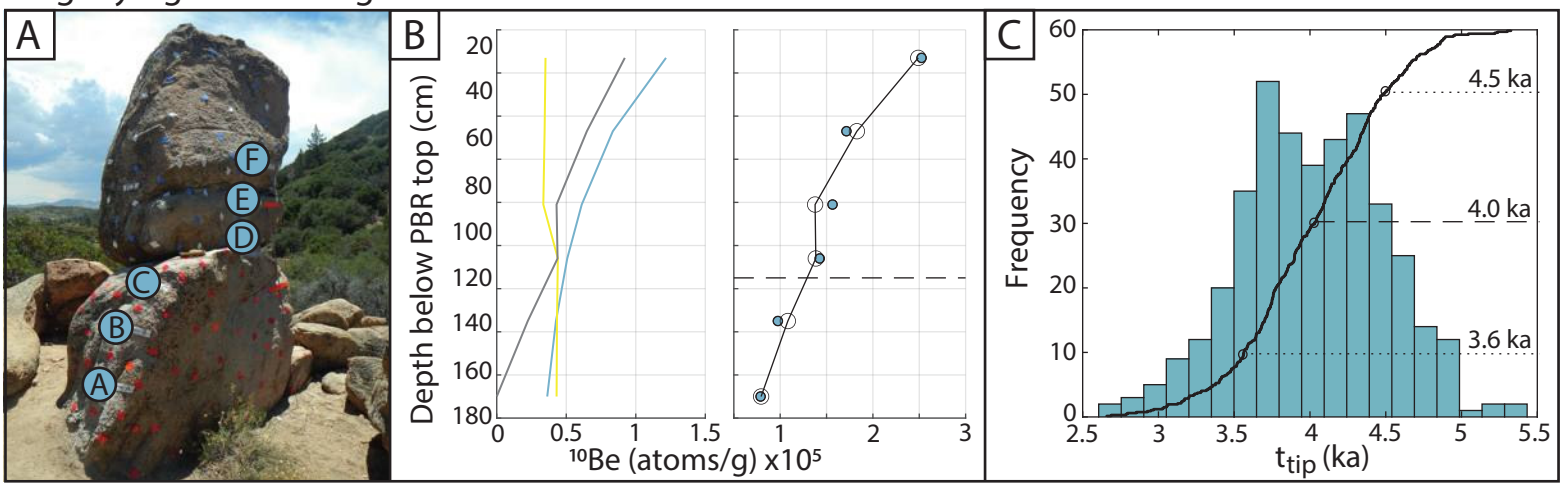

(A) Samples D - F are located on the PBR, and samples A - C are located on the pedestal. Due to the dip of the pedestal, sample C is above the lowest point on the PBR-pedestal contact. (B) The samples collected down two sides of the outcrop result in a distinctive change in shielding and, therefore, associated profile of post-exhumation ^{10}Be production (gray line), between the two sides. The low modeled ε_0 and higher, but still low, ε_1 result in ^{10}Be accumulation both before and during exhumation (blue and yellow lines, respectively).

Hazard Validation Results Figures

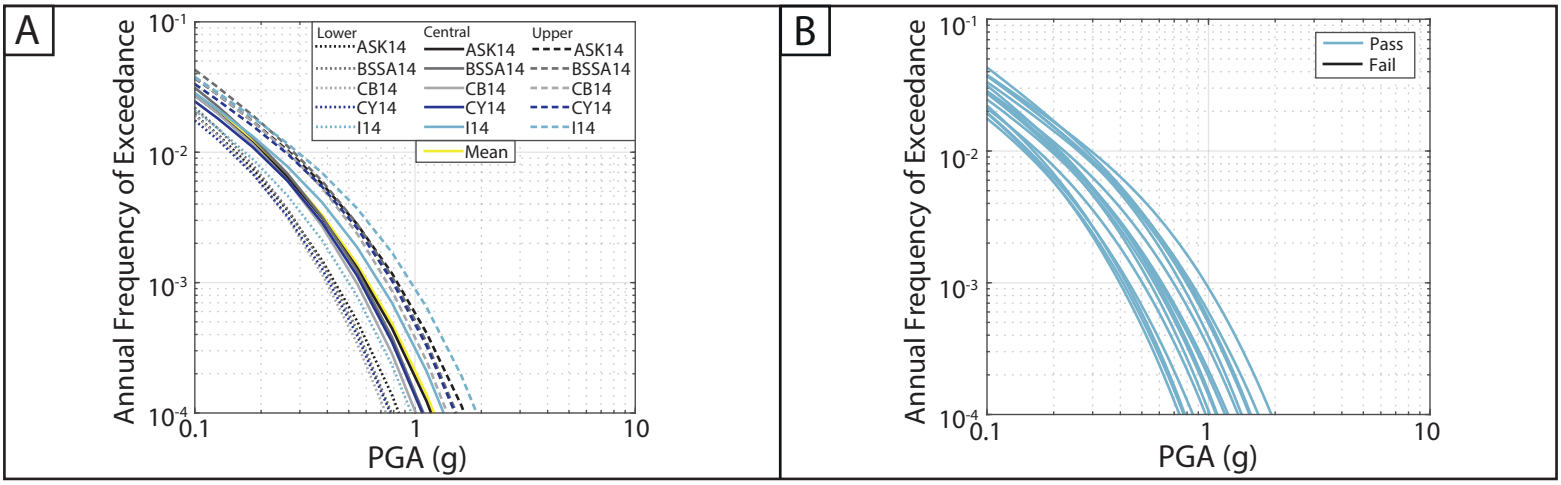

The dominant seismic sources at the PI2 site are the San Andreas fault, Cleghorn fault, San Jacinto fault, and North Frontal thrust faults. The combination of the young fragility age and moderate fragility of PI2 cause none of the three branches (upper, central, and lower) of all five GMMs to be inconsistent with a 5% probability of survival of PI2. The removal of the I14 GMM, at 2475 year mean return period, reduces the mean ground-motion estimate by 3% and the reduces the range of estimated 5th–95th fractile ground motions by 18% at the PI2 site.

PNT01

Fragility Results Figures

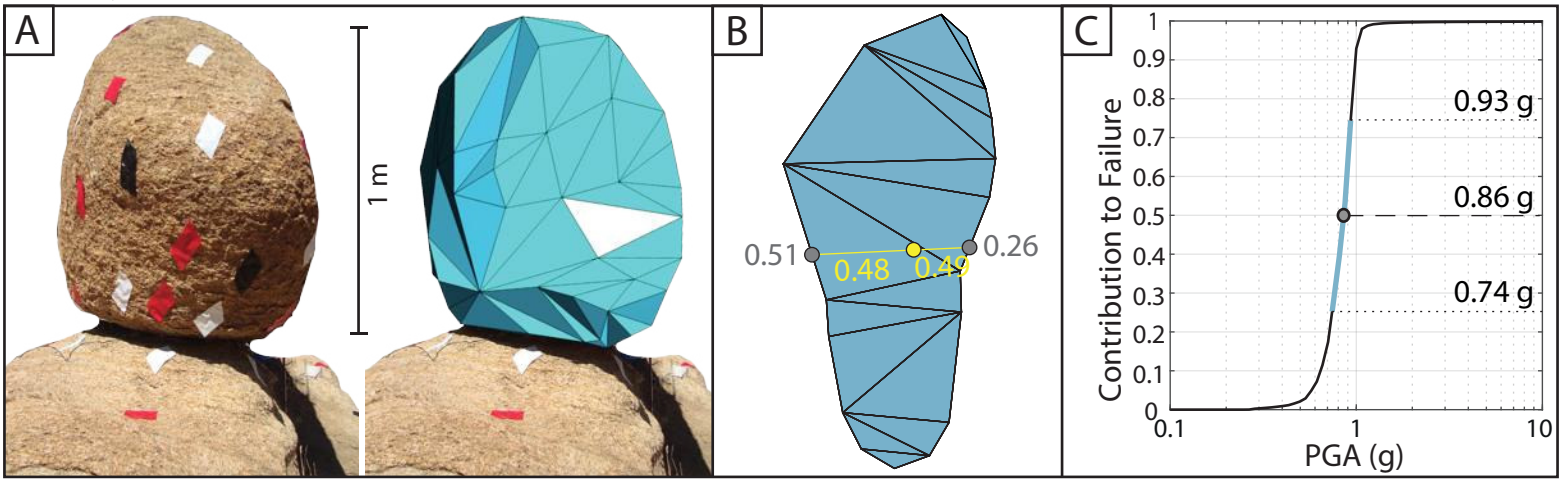

(A) PNT01 is bounded by joints, which continue through the pedestal and surrounding outcrop, on both the fragile rocking directions, which indicates that the PBR was exhumed in its current geometry and that negligible post-exhumation erosion has occurred. (B) The two alternative methods of selecting α_1 and α_2 produce a minor 5% and 7% difference, respectively. Therefore, we only have moderate confidence that the basal area of PNT01 approximates the rectangular basal geometry that was described by the Purvance et al. (2008) fragility equations. In addition, the α_2 of PNT01 is greater than the range investigated by Purvance et al. (2008), which further reduces our confidence in the fragility characterization of PNT01. α_2 is 2.00 times greater than α_1, so PNT01 is classified as having an asymmetric rocking response.

Fragility Age Results Figures

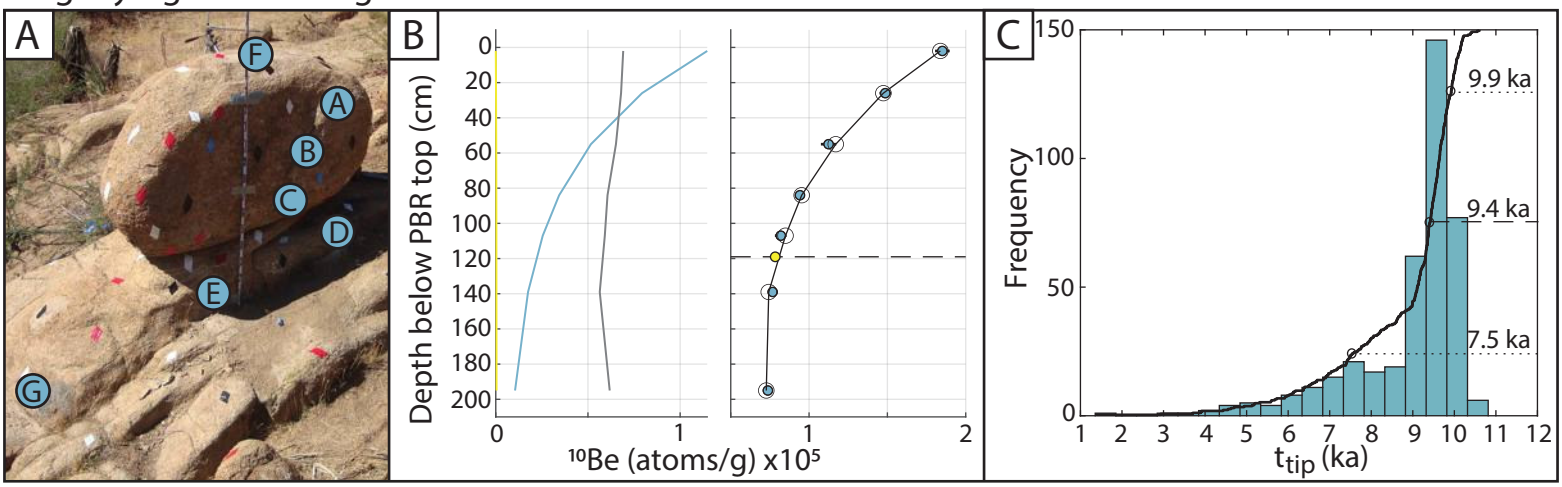

(A) Samples A - C and F are located on the PBR, and samples D, E, and G are located on the pedestal. Due to the dip of the PBR-pedestal contact, sample D is above the lowest point on the PBR-pedestal contact. (B) The best fit modeled ε_1 suggests instantaneous exhumation of the PBR, which results in no ^{10}Be accumulation during exhumation (yellow line). The saprolite sample was collected ~8 m from the PBR at approximately the height of the PBR-pedestal contact. All ^{10}Be accumulated in the saprolite sample was produced during post-ε_1 exposure due to the modeled instantaneous ε_1 value. We calculated an exposure age of 8193±300 years for the saprolite sample, assuming zero erosion and no inheritance, which overlaps within the uncertainties on the t_{tip} age of PNT01. This agreement in ages further validates our geomorphic model that the rapid saprolite erosion that exhumed the PBR, ε_1, abruptly stopped at the present ground surface level, and since that time has been accumulating ^{10}Be at a negligible erosion rate.

Hazard Validation Results Figures

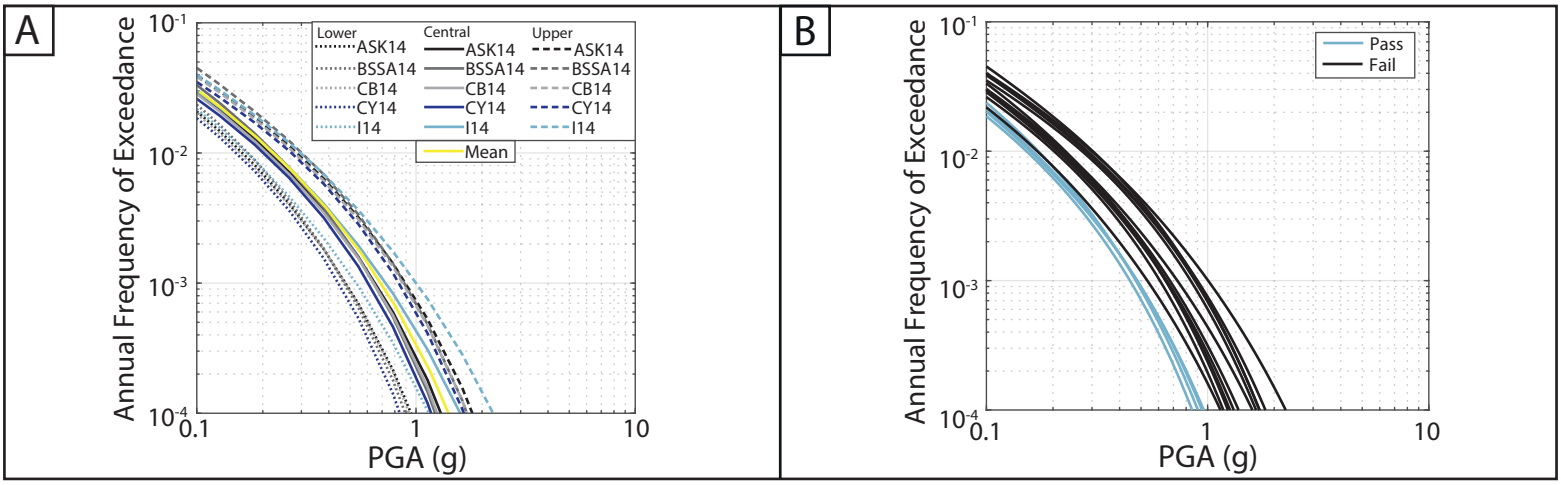

The dominant seismic source controlling the seismicity of the PNT01 site is the Pinto Mountain fault. The moderate fragility age and relatively unstable fragility of PNT01 cause the upper and central branches of all five GMMs as well as the lower branch I14 to be inconsistent with a 5% probability of survival of PNT01. The removal of the I14 GMM, at 2475 year mean return period, reduces the mean ground-motion estimate by 3% and the reduces the range of estimated 5th–95th fractile ground motions by 26% at the PNT01 site.

PP1

Fragility Results Figures

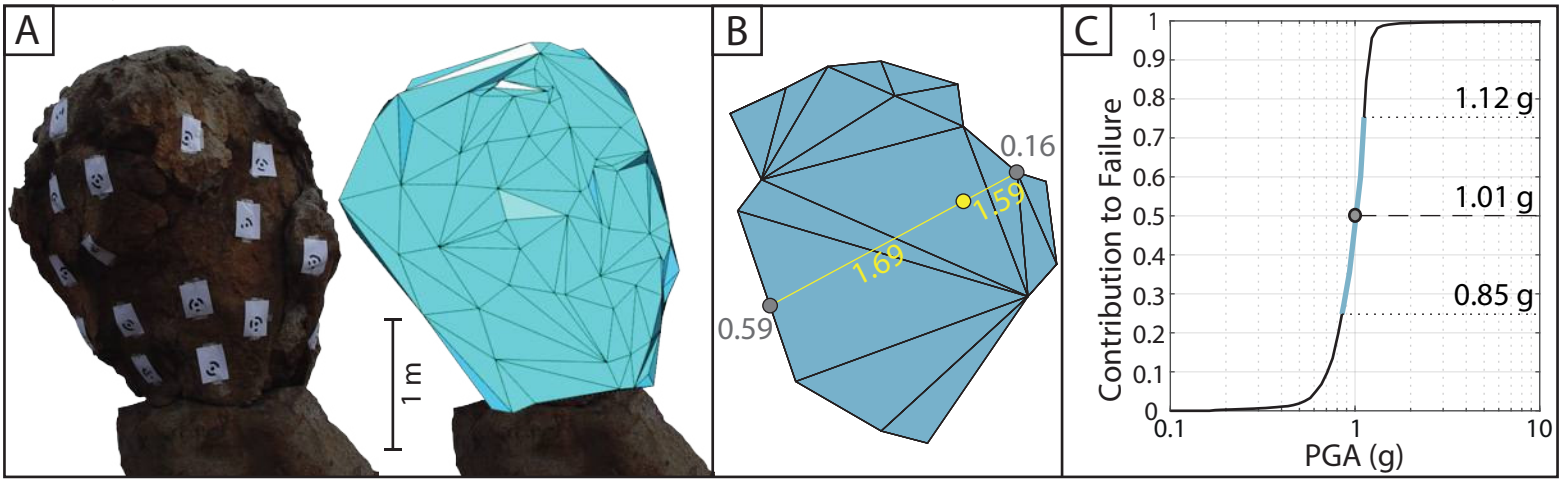

(A) Field observations of PP1 suggested that it experienced post-exhumation erosion, i.e., spalling, of previously case hardened rock surfaces, which together suggest a long period of negligible post-exhumation erosion followed by a more recent period of post-exhumation erosion. (B) The two alternative methods of selecting α_1 and α_2 produce a minor 6% and 7% difference, respectively. Therefore, we only have moderate confidencethat the basal area of PP1 approximates the rectangular basal geometry that was described by the Purvance et al. (2008) fragility equations. In addition, the α_2 of PP1 is greater than the range investigated by Purvance et al. (2008), which further reduces our confidence in the fragility characterization of PP1. α_2 is 3.60 times greater than α_1, so PP1 is classified as having an asymmetric rocking response.

Fragility Age Results Figures

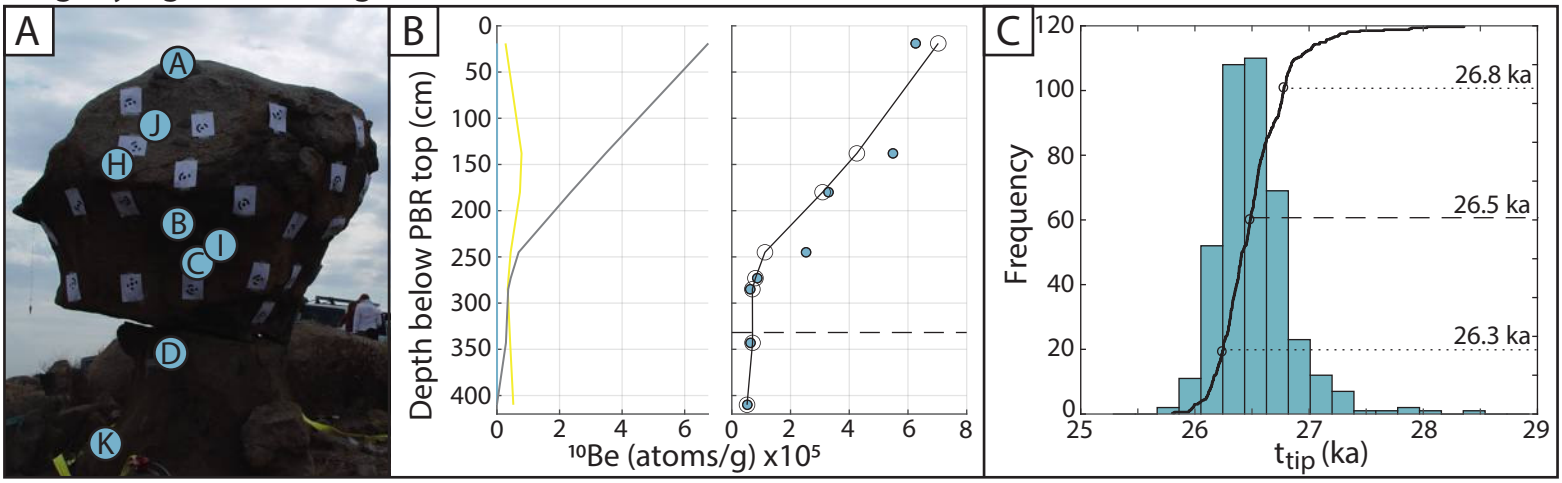

(A) Samples A - C and H - J are located on the PBR, and samples D and K are located on the pedestal. The samples were collected from PP1 after it was toppled during a housing development construction project, and the sample locations had to be reconstructed onto the 3-D model constructed from pre-toppling photos. (B) We suggest that post-exhumation erosion could be responsible for the poor fit of measured to modeled ^{10}Be concentrations. However, fitting the model using only the four lowest samples, i.e., 2 samples above and 2 samples below the PBR-pedestal contact, yields the same t_{tip} fragility age. PP1 has an instantaneous best fit ε_0 value, which we believe suggests that the ε_0 signal has been completely removed during the ε_1 phase of exhumation and so ε_0 is an unconstrained parameter for PP1. Alternatively, the occurrence of post-exhumation erosion would violate the assumptions of our geomorphic model, therefore, we cannot be confident in the modeled fragility age of PP1.

Hazard Validation Results Figures

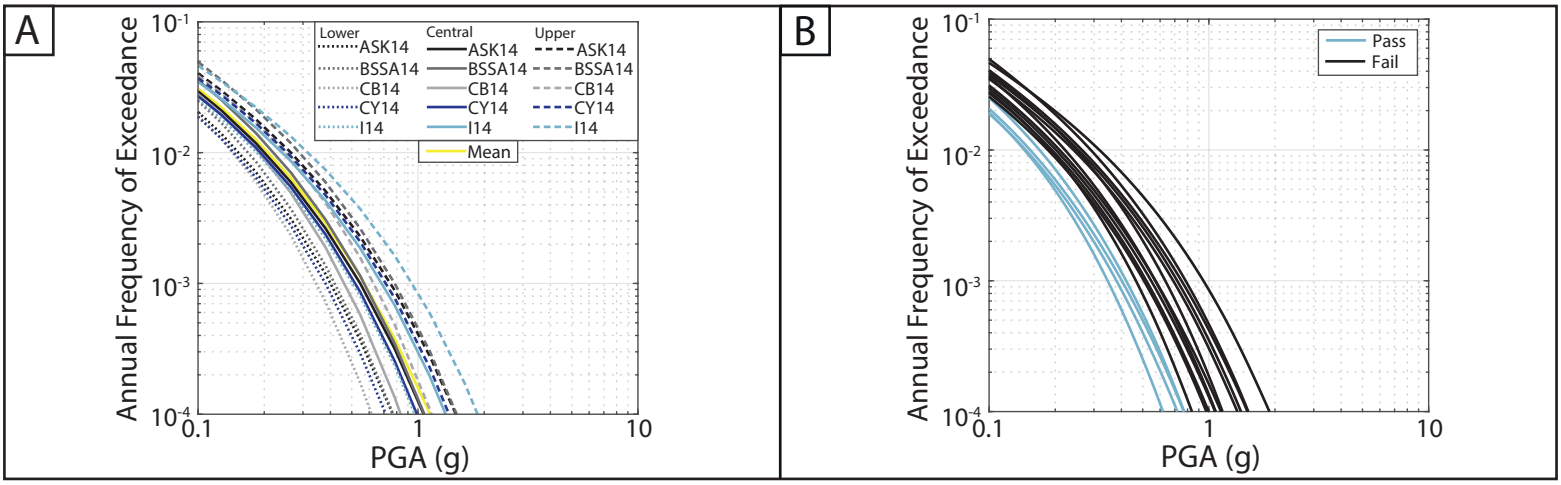

PP1 is located between the San Jacinto and Elsinore faults, which are the dominant seismic sources controlling the seismicity at the site. The old fragility age and unstable fragility of PP1 cause the upper and central branches of all five GMMs as well as the lower branch I14 to be inconsistent with a 5% probability of survival of PP1. The removal of the I14 GMM, at 2475 year mean return period, reduces the mean ground-motion estimate by 5% and the reduces the range of estimated 5th–95th fractile ground motions by 24% at the PP1 site.

RT1

Fragility Results Figures

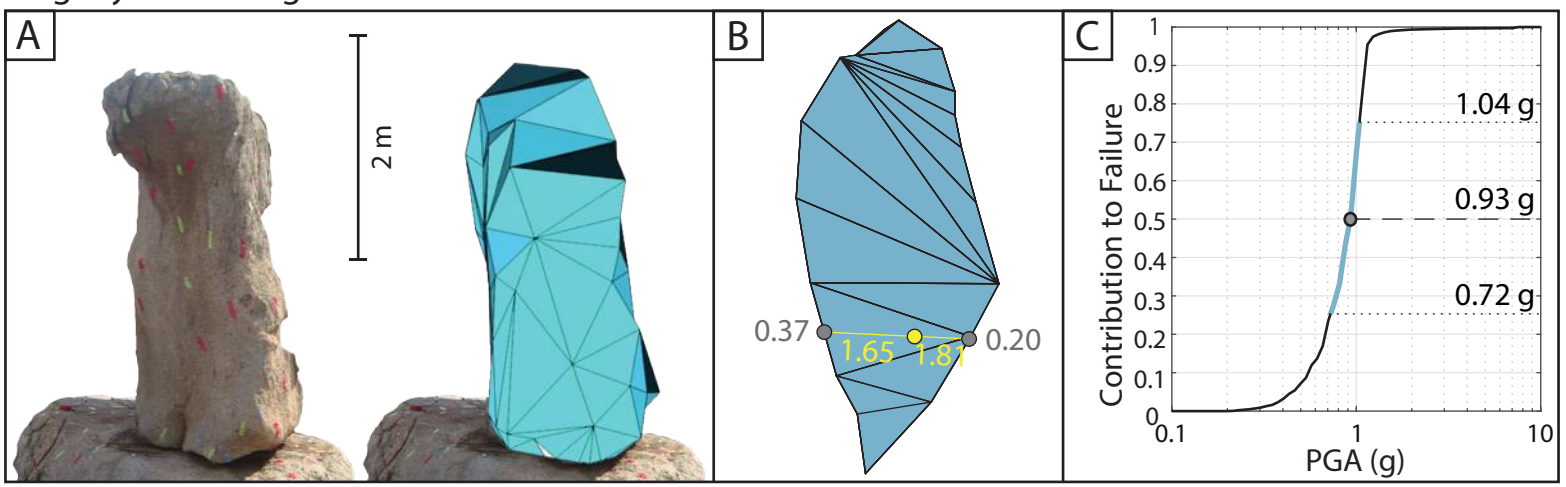

(A) RT1 was the PBR studied by Hall et al. (2019), who concluded that it had been exhumed with its current geometry and that since exhumation little weathering has occurred to the PBR (B) The two alternative methods of selecting α_1 and α_2 produce a significant 13% and 25% difference, respectively. Therefore, we only have moderate confidence that the basal area of RT1 approximates the rectangular basal geometry that was described by the Purvance et al. (2008) fragility equations. α_2 is 1.83 times greater than α_1, so RT1 is classified as having an asymmetric rocking response.

Fragility Age Results Figures

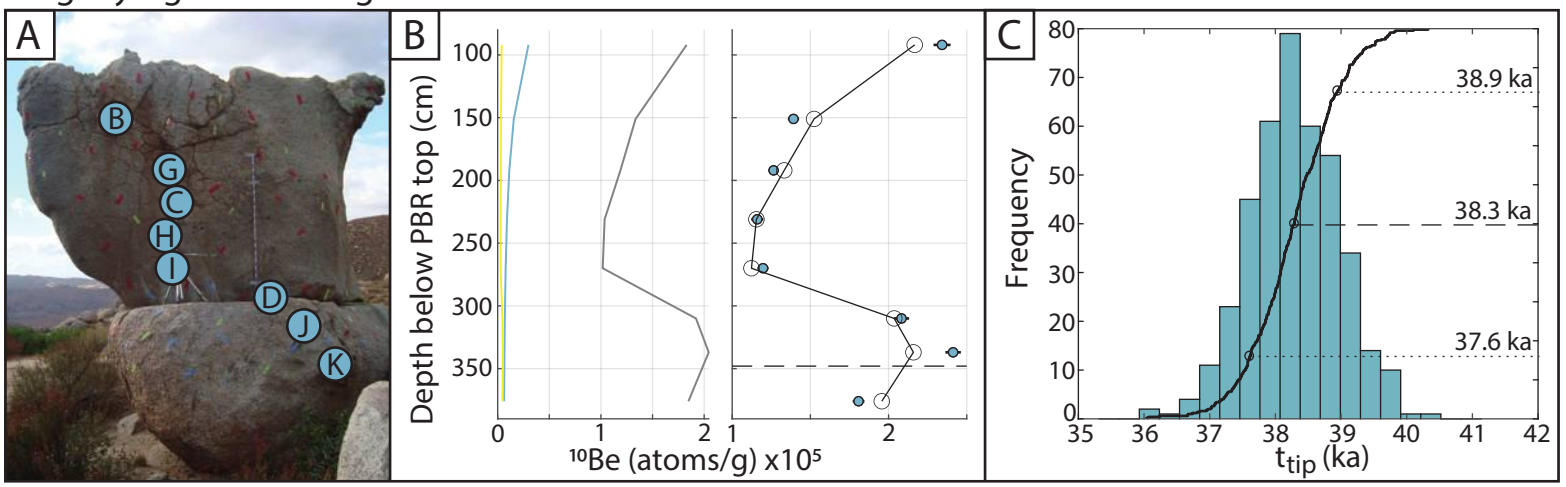

(A) Samples B, C and G - I are located on the PBR, and samples J and K are located on the pedestal. Due to the dip of the PBR-pedestal contact, samples D and J are above the lowest point on the PBR-pedestal contact. (B) RT1 is modeled to have beem exhumed by a rapid ε_1, therefore, negligibe ^{10}Be accumulation occurred during exhumation (yellow line). We suggest that the poor model fitting to the lowest three samples is due to the large height of RT1 and so the increased likelihood of violating our model assumption that the full range of sample heights was exhumed during a single pulse of erosion at a constant rate.

Hazard Validation Results Figures

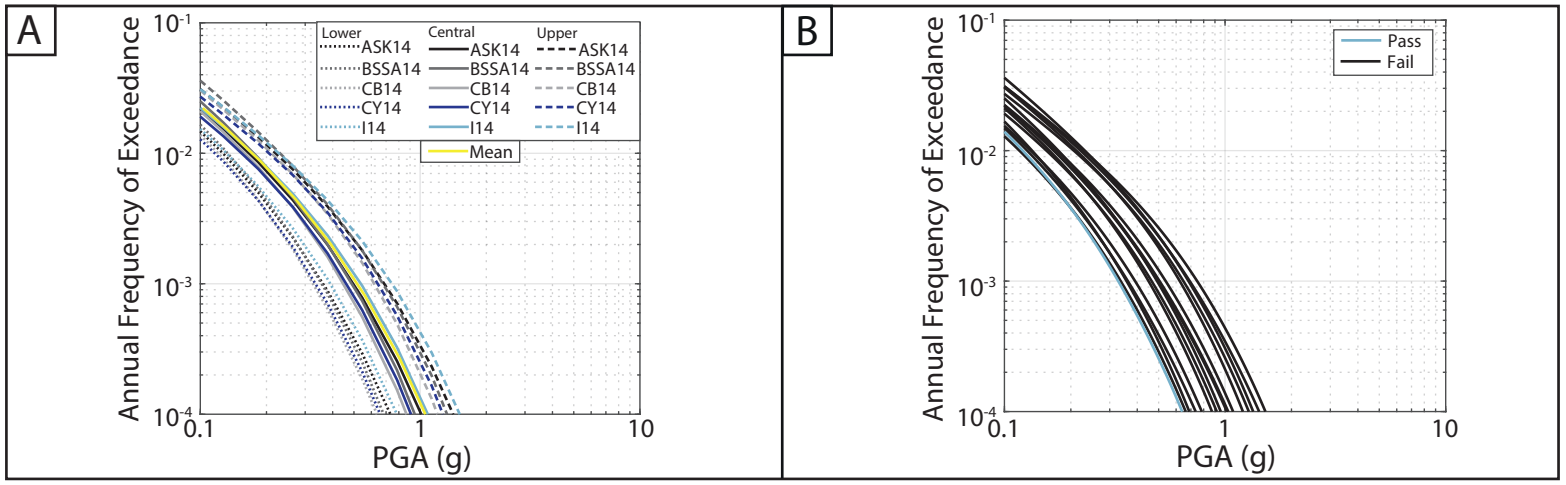

RT1 is located between the San Jacinto and Elsinore faults, which are the dominant seismic sources controlling the seismicity at the site. The old fragility age and unstable fragility of RT1 cause the upper and central branches of all five GMMs and the lower branches of ASK14, BSSA14, CY14, and I14 to be inconsistent with a 5% probability of survival of RT1. The removal of the I14 GMM, at 2475 year mean return period, reduces the mean ground-motion estimate by 2% and the reduces the range of estimated 5th–95th fractile ground motions by 10% at the RT1 site.

SW02

Fragility Results Figures

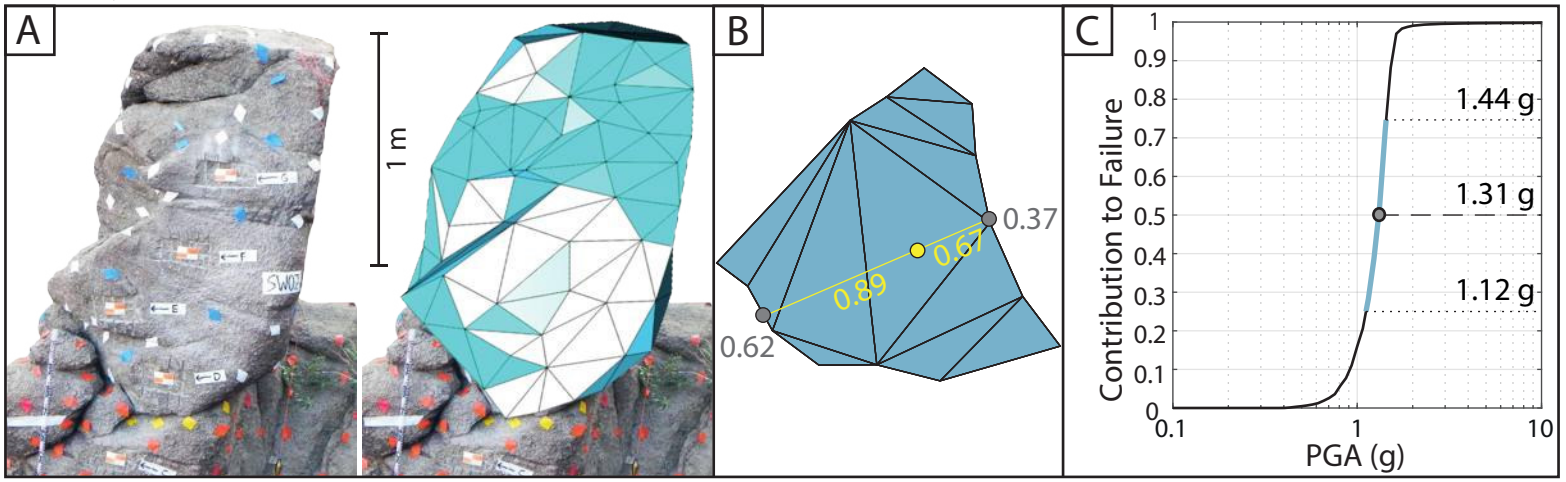

(A) SW02 is clearly bounded on all sides by joints that continue into the pedestal and surrounding outcrop. (B) The two alternative methods of selecting α_1 and α_2 produce a minor 1% and moderate 11% difference, respectively. Therefore, we have moderate confidence that the basal area of SW02 approximates the rectangular basal geometry that was described by the Purvance et al. (2008) fragility equations. In addition, the α_2 of SW02 is greater than the range investigated by Purvance et al. (2008), which further reduces our confidence in the fragility characterization of SW02. α_2 is 1.68 times greater than α_1, so SW02 is classified as having an asymmetric rocking response.

Fragility Age Results Figures

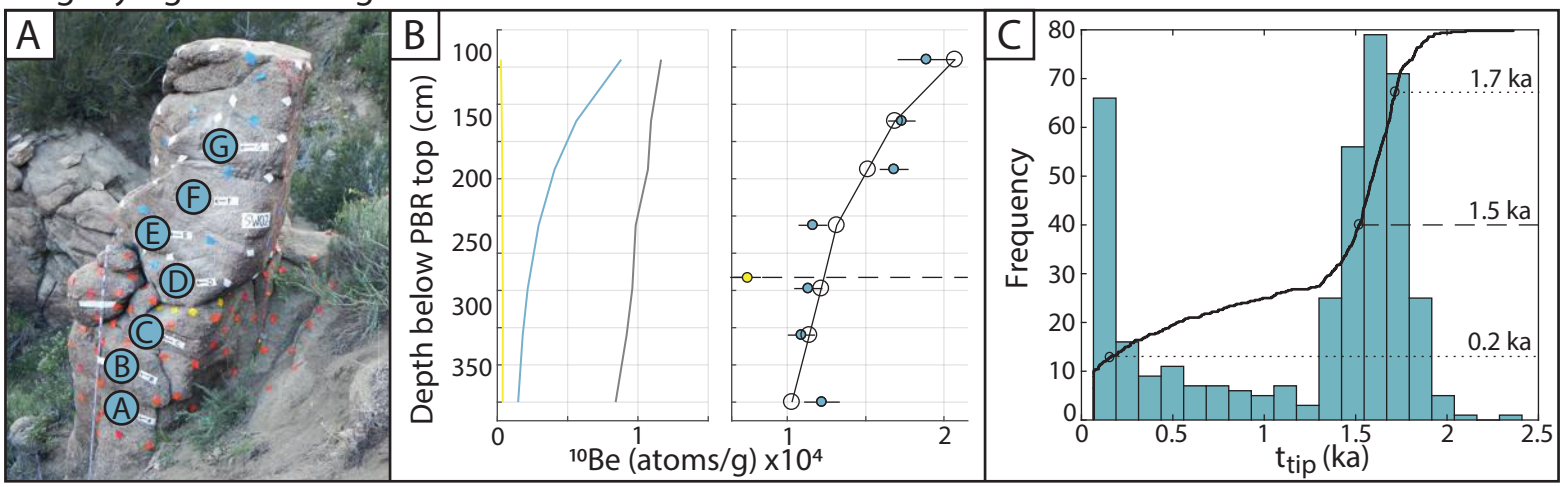

(A) Samples D - G are located on the PBR, and samples A - C are located on the pedestal. (B) The low measured ^{10}Be concentrations relate to a young fragility age. The best fit ε_1 suggests rapid exhumation, which is plausible considering the location of the PBR in the center of a steep stream channel. The saprolite sample was collected ~2 m from the PBR at approximately the height of the PBR-pedestal contact. All the measured ^{10}Be accumulated in the saprolite sample (yellow circle) was produced during post-ε_1 exposure due to the modeled instantaneous ε_1 value. We calculated an exposure age of 937±80 years for the saprolite sample, assuming zero erosion and no inheritance. This age overlaps within the uncertainties on the t_{tip} age of SW02. This agreement in ages validates our geomorphic model that the rapid saprolite erosion that exhumed the PBR, ε_1, abruptly stopped at the present ground surface level, and since that time has been accumulating ^{10}Be at a negligible erosion rate.

Hazard Validation Results Figures

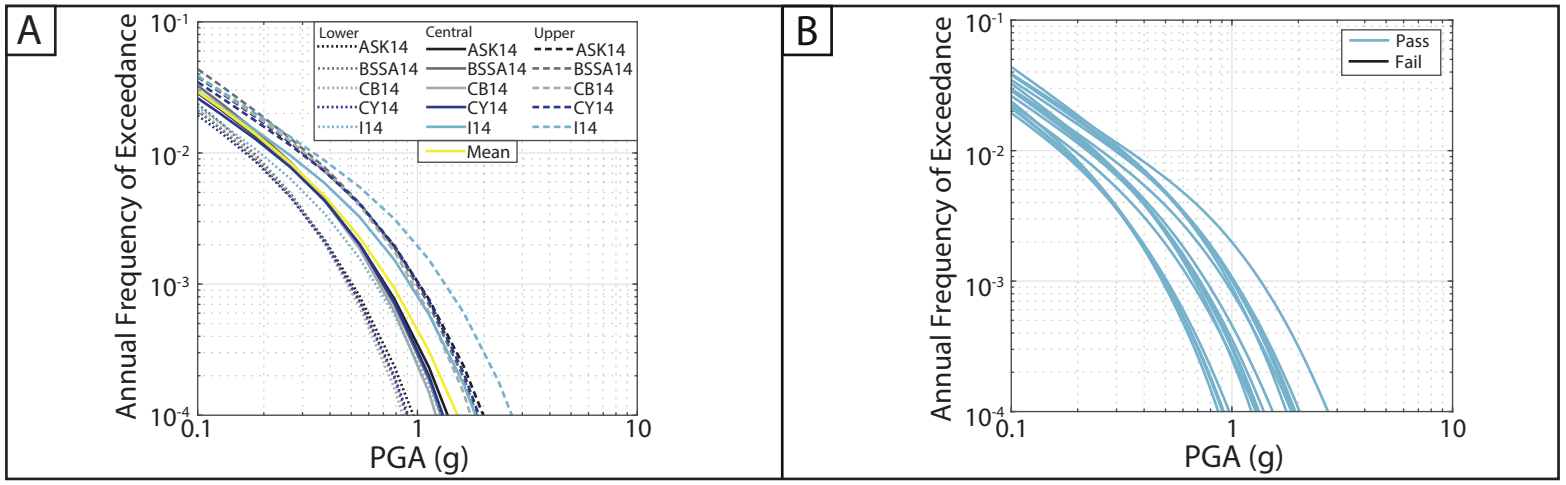

The dominant seismic sources at the SW02 site are the San Andreas fault, Cleghorn fault, San Jacinto fault, and North Frontal thrust faults. The combination of the young fragility age and stable fragility of SW02 cause none of the three branches (upper, central, and lower) of all five GMMs to be inconsistent with a 5% probability of survival of SW02. The removal of the I14 GMM, at 2475 year mean return period, reduces the mean ground-motion estimate by 5% and the reduces the range of estimated 5th–95th fractile ground motions by 33% at the SW02 site.

UCR1

Fragility Results Figures

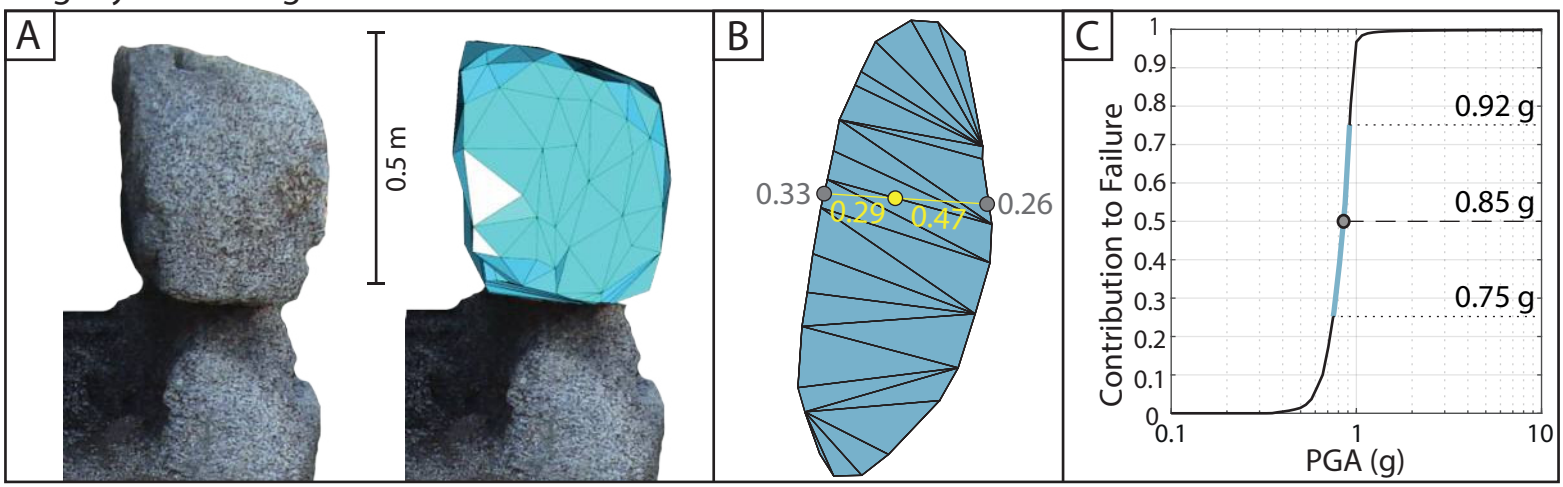

(A) The geometry of UCR1 is well defined on one side by a joint surface (left side in photo), which suggests limited erosion on one side of the PBR. (B) The two alternative methods of selecting α_1 and α_2 produce a minor 2% and 8% difference, respectively. Therefore, we have moderate confidence that the basal area of UCR1 approximates the rectangular basal geometry that was described by the Purvance et al. (2008) fragility equations. α_2 is 1.43 times greater than α_1, so UCR1 is classified as having an asymmetric rocking response.

Fragility Age Results Figures

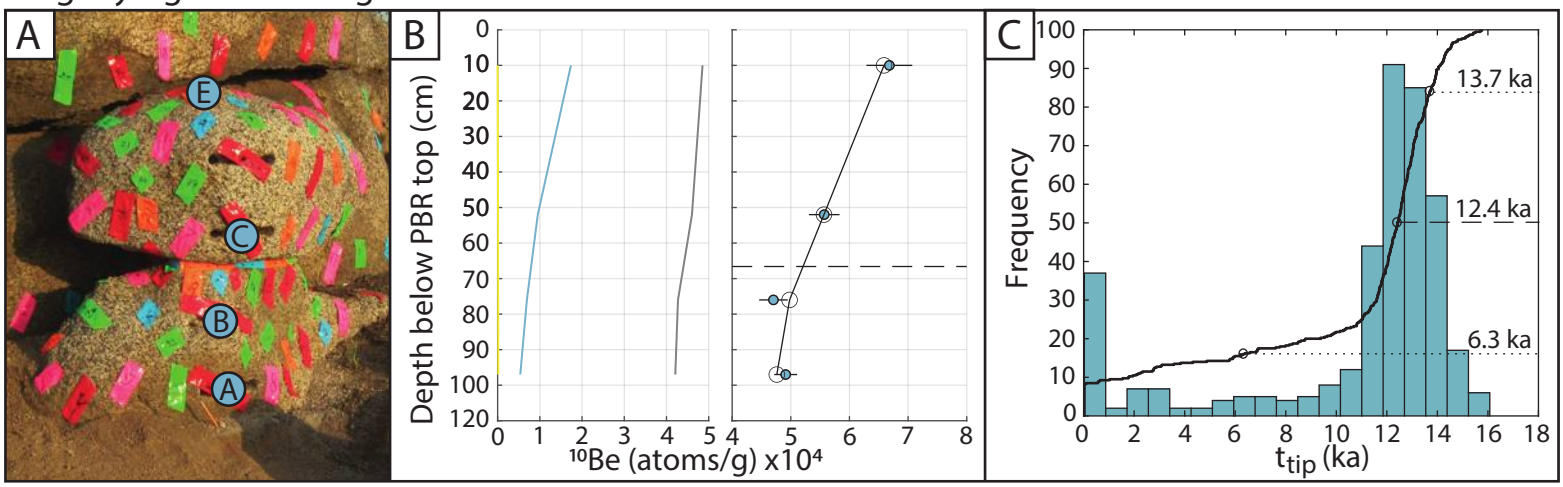

(A) Samples C and E are located on the PBR, and samples A and B are located on the pedestal. (B) Of the PBRs in this study, the fewest samples over the shortest height range were collected from UCR1. However, we demonstrate that our fragility age model is able to produce a good model fit to even only 4 measured samples collected over ~1 m of height. (C) We suggest that both the limited height over which to model the ^{10}Be data and the narrow range of shielding factors due to the small distance between samples resulted in a non-unique solution and, therefore, the lack of a clear t_{tip} histogram peak.

Hazard Validation Results Figures

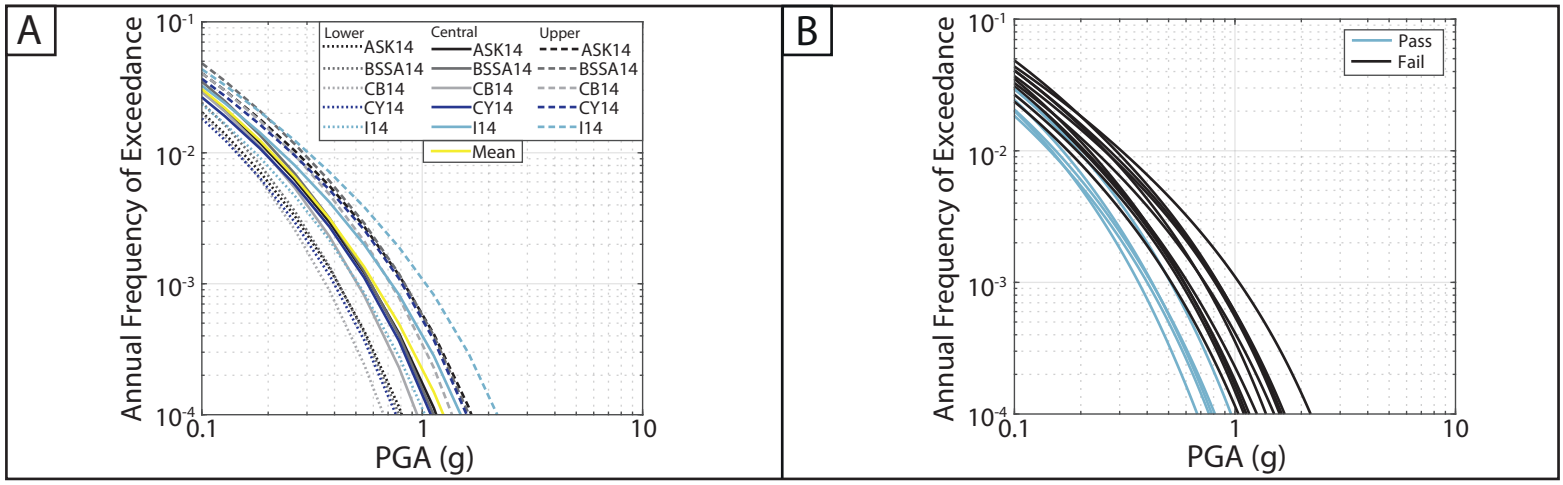

UCR1 is located between the San Jacinto and Elsinore faults, which are the dominant seismic sources controlling the seismicity at the site. The young fragility age and relatively unstable fragility of UCR1 cause the upper branches of all five GMMs, the central branches of ASK14, BSSA14, CY14, and I14 and the lower branch of I14 to be inconsistent with a 5% probability of survival of UCR1. The removal of the I14 GMM, at 2475 year mean return period, reduces the mean ground-motion estimate by 4% and the reduces the range of estimated 5th–95th fractile ground motions by 26% at the UCR1 site.

YV1

Fragility Results Figures

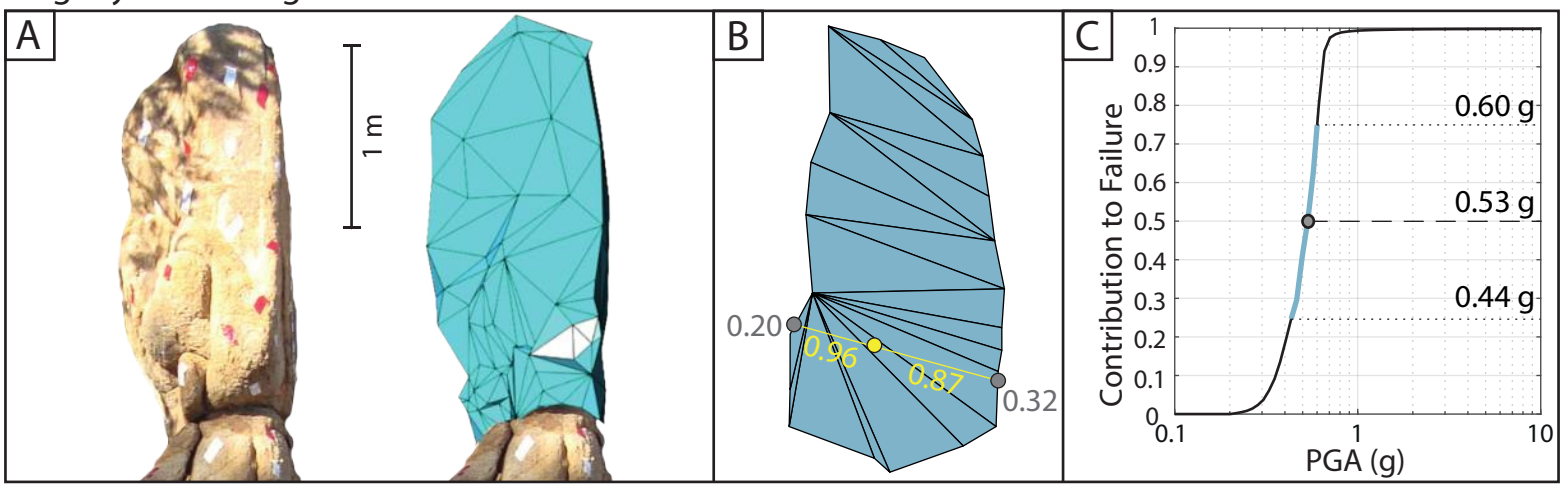

(A) The geometry of YV1 is well defined on one side by a joint surface (right side in photo), which suggests limited erosion on one side of the PBR. (B) The two alternative methods of selecting α_1 and α_2 produce near identical values, therefore, we are confident that the basal area of YV1 approximates the rectangular basal geometry that was described by the Purvance et al. (2008) fragility equations. α_2 is 1.58 times greater than α_1, so YV1 is classified as having an asymmetric rocking response. However, the rocking response of YV1 may be complicated by the dip of the pedestal towards the adjacent outcrop, which may be supporting the PBR in a direction orthogonal to its 2-D rocking direction. In other words, YV1 may instead fail in the direction of the supporting outcrop if the supporting outcrop were damaged during ground motion.

Fragility Age Results Figures

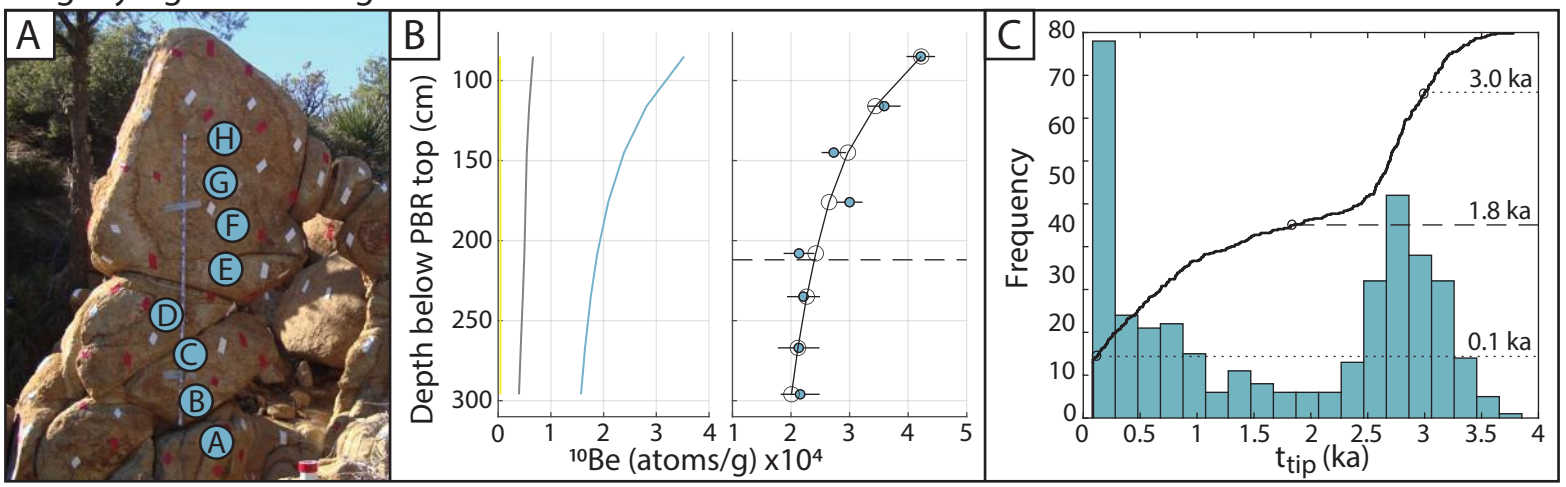

(A) Samples E - H are located on the PBR, and samples A - D are located on the pedestal. Due to the inclined dip of the PBR-pedestal contact, sample D is above the lowest point on the PBR-pedestal contact. (B) The best fit ε_1 suggests rapid exhumation, which is plausible considering the location of the PBR in the center of a stream channel, therefore negligible ^{10}Be accumulation is modeled to have occurred during exhumation (yellow line). Because the samples were collected from a planar surface, the shielding values result in a post-exhumation ^{10}Be profile (gray line) that has a shape similar to the pre-exhumation ^{10}Be profile (blue line), which has the net effect of producing a non-unique t_{tip} solution. Therefore, we have low confidence in the fragility age results of YV1.

Hazard Validation Results Figures

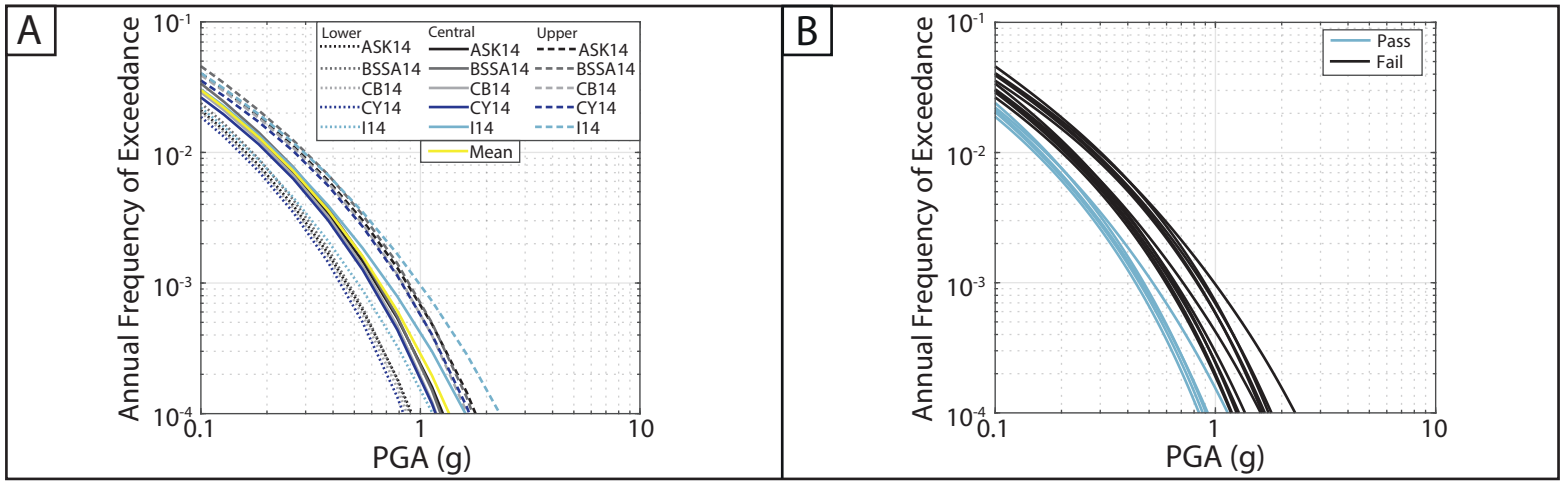

The dominant seismic source controlling the seismicity of the YV1 site is the Pinto Mountain fault. The young fragility age and relatively unstable fragility of YV1 cause the ground-motions estimated by the upper and central branches of all five GMMs to be are inconsistent with a 5% probability of survival of YV1. The removal of the I14 GMM, at 2475 year mean return period, reduces the mean ground-motion estimate by 2% and the reduces the range of estimated 5th–95th fractile ground motions by 21% at the YV1 site.

Table 1.1. Full parameters used for PBR sample data reduction.

PBR ID	Sample ID	Blank*	Quartz (g)	Be carrier (g)	[^{9}Be] (ug/g)	^{10}Be/^{9}Be†	1σ	[^{10}Be] atoms/g	1σ§	Facility	AMS ID
BR1	BR1-A	1	8.619	0.4735	424	1.9882E-13	3.9210E-15	305795	6141	LLNL	BE32173
	BR1-B	1	8.054	0.4775	424	1.6265E-13	3.5277E-15	269295	5972	LLNL	BE32174
	BR1-C	1	9.634	0.4731	424	1.3850E-13	4.0761E-15	189452	5705	LLNL	BE32175
	BR1-D	1	8.348	0.4770	424	9.0844E-14	2.8677E-15	143274	4697	LLNL	BE32176
	BR1-E	1	8.467	0.4750	424	8.1938E-14	1.9186E-15	126507	3129	LLNL	BE32177
	BR1-F	1	8.936	0.4736	424	1.4764E-13	2.7879E-15	218176	4239	LLNL	BE32178
	BR1-G	1	7.702	0.4748	424	1.4033E-13	5.6048E-15	240997	9819	LLNL	BE32179
BS1	BS1-A	2	20.025	0.7571	266	2.5219E-13	5.8599E-15	168429	3940	LLNL	BE25596
	BS1-B	2	20.050	0.7536	266	1.7945E-13	4.1701E-15	118844	2789	LLNL	BE25597
	BS1-C	3	20.264	0.4703	424	1.2007E-13	2.8292E-15	77031	1938	LLNL	BE26600
	BS1-E	4	7.997	0.4753	424	6.5347E-14	1.5136E-15	105462	2900	LLNL	BE31912
	BS1-F	4	7.929	0.4750	424	7.8242E-14	1.6362E-15	128177	3107	LLNL	BE31913
	BS1-G	4	7.708	0.4748	424	9.3389E-14	1.8437E-15	158231	3522	LLNL	BE31914
	BS1-H	4	8.166	0.4737	424	1.2680E-13	2.3589E-15	203931	4105	LLNL	BE31915
BS2	BS2-A	5	15.010	0.4458	449	5.4684E-14	2.5082E-15	44776	2345	SUERC	b6856
	BS2-B	5	14.857	0.4465	449	5.5242E-14	2.4719E-15	45811	2342	SUERC	b6857
	BS2-C	5	12.976	0.4459	449	5.1336E-14	2.2711E-15	48354	2482	SUERC	b6858
	BS2-D	5	11.935	0.4458	449	5.7195E-14	2.4552E-15	59126	2893	SUERC	b6860
	BS2-E	5	8.503	0.4454	449	4.3803E-14	2.7816E-15	61869	4548	SUERC	b6861
	BS2-F	5	9.762	0.4453	449	6.0543E-14	2.7342E-15	76788	3898	SUERC	b6862
	BS2-G	6	12.538	0.9677	204	4.6593E-14	2.1399E-15	46227	2372	SUERC	b7594
GV1	GV1-1	2	20.090	0.7566	266	2.9779E-13	5.5262E-15	198296	3701	LLNL	BE25598
	GV1-B	7	11.977	0.4452	449	4.0539E-13	1.1495E-14	448281	12855	SUERC	b6944
	GV1-C	7	13.488	0.4451	449	3.3452E-13	1.4564E-14	327809	14445	SUERC	b6945
	GV1-D	7	5.254	0.4444	449	9.8208E-14	3.9339E-15	240519	10219	SUERC	b6946
	GV1-E	7	11.736	0.4450	449	1.7354E-13	5.1336E-15	193520	5921	SUERC	b6947
	GV1-F	7	12.590	0.4447	449	1.6070E-13	5.7753E-15	166671	6188	SUERC	b6948
	GV1-G	7	13.403	0.4441	449	1.2081E-13	4.8546E-15	116687	4901	SUERC	b6950
GV2	GV2-1	2	20.034	0.7565	266	2.4486E-13	5.6897E-15	163298	3821	LLNL	BE25599
	GV2-2	2	20.038	0.7573	266	6.1231E-13	1.0011E-14	410286	6726	LLNL	BE25600
	GV2-3	3	19.494	0.4732	424	1.0038E-12	2.3220E-14	688326	15979	LLNL	BE26594
	GV2-4	3	20.018	0.4732	424	3.1289E-13	6.4669E-15	207599	4366	LLNL	BE26595
LB05	LB05-A	8	13.675	0.4456	449	1.6461E-13	5.6916E-15	144402	5987	SUERC	b6833
	LB05-B	8	12.882	0.4447	449	1.7912E-13	5.0220E-15	168008	5704	SUERC	b6835
	LB05-C	8	16.711	0.4458	449	2.2655E-13	6.0543E-15	167795	5172	SUERC	b6836
	LB05-D	8	11.235	0.4450	449	1.7465E-13	5.2452E-15	187462	6787	SUERC	b6837
	LB05-E	8	16.122	0.4444	449	2.5975E-13	5.9427E-15	200837	5258	SUERC	b6838
	LB05-F	8	15.078	0.4450	449	2.7956E-13	6.7797E-15	232574	6328	SUERC	b6839
LJ1	LJ1-1	2	20.011	0.7569	266	1.9213E-13	4.4583E-15	128122	3175	LLNL	BE25601
	LJ1-2	2	20.006	0.7560	266	9.9749E-14	2.3156E-15	65952	1875	LLNL	BE25602
	LB1-5	4	9.162	0.4719	424	6.8548E-14	1.6160E-15	96060	2374	LLNL	BE31926
	LB1-6	4	8.124	0.4712	424	3.8497E-14	1.1574E-15	58786	1927	LLNL	BE31925
	LB1-7	4	9.343	0.4715	424	3.4293E-14	1.1178E-15	45139	1621	LLNL	BE31924
	LB1-8	4	8.678	0.4720	424	3.0058E-14	8.4531E-16	42124	1335	LLNL	BE31923
	LB1-9	4	9.520	0.4726	424	5.0385E-14	1.3780E-15	67040	1957	LLNL	BE31922
LJ5	LJ5-A	9	15.198	0.3368	759.44	1.3445E-13	2.6865E-15	149323	3060	ANSTO	XBE0347
	LJ5-B	9	11.080	0.3350	759.44	1.6547E-13	3.3236E-15	251321	5142	ANSTO	XBE0348
	LJ5-C	9	14.403	0.3360	759.44	2.5096E-13	4.9874E-15	295122	5926	ANSTO	XBE0349
	LJ5-D	9	16.993	0.3368	759.44	2.9508E-13	5.8666E-15	295113	5917	ANSTO	XBE0350
	LJ5-E	9	14.026	0.3362	759.44	3.1673E-13	6.2916E-15	383238	7671	ANSTO	XBE0351
	LJ5-F	9	14.874	0.3369	759.44	3.7021E-13	7.3557E-15	423613	8469	ANSTO	XBE0352
	LJ5-G	9	16.425	0.3349	759.44	4.6747E-13	9.2918E-15	481971	9625	ANSTO	XBE0353

Table 1.1. (continued)

PBR ID	Sample ID	Blank*	Quartz (g)	Be carrier (g)	[^{9}Be] (ug/g)	^{10}Be/^{9}Be†	1σ	[^{10}Be] atoms/g	1σ§	Facility	AMS ID
LJB1	LJB1-A	10	7.030	0.4484	449	1.9000E-13	6.1659E-15	355487	11932	SUERC	b6993
	LJB1-B	11	19.963	0.4451	449	4.1934E-13	9.5418E-15	277812	6411	SUERC	b6847
	LJB1-C	11	11.872	0.4418	449	1.9000E-13	5.6079E-15	207621	6342	SUERC	b6848
	LJB1-D	11	18.018	0.4431	449	2.6505E-13	8.2863E-15	192579	6150	SUERC	b6849
	LJB1-E	11	16.240	0.4407	449	1.9670E-13	5.4405E-15	156852	4490	SUERC	b6850
	LJB1-F	5	12.626	0.4484	449	1.3727E-13	4.3524E-15	141536	4715	SUERC	b6869
	LJB1-G	5	14.716	0.4473	449	2.1595E-13	5.4963E-15	192888	5065	SUERC	b6866
LJB2	LJB2-A	10	15.761	0.4478	449	4.3580E-13	9.7092E-15	367879	8314	SUERC	b6953
	LJB2-B	10	16.359	0.4483	449	3.4903E-13	8.8722E-15	283485	7334	SUERC	b6954
	LJB2-C	10	15.701	0.4478	449	3.2448E-13	7.3656E-15	274027	6352	SUERC	b6958
	LJB2-D	10	17.532	0.4489	449	3.2727E-13	7.6167E-15	248154	5894	SUERC	b6959
	LJB2-E	10	17.919	0.4477	449	3.0439E-13	9.9603E-15	224996	7499	SUERC	b6960
MR1	MR1-A	12	8.996	0.4426	449	1.2137E-13	4.1571E-15	174457	6264	SUERC	b7510
	MR1-B	12	6.116	0.4436	449	6.5565E-14	3.2922E-15	135758	7400	SUERC	b7511
	MR1-C	12	17.725	0.4428	449	1.2583E-13	4.4640E-15	91928	3406	SUERC	b7515
	MR1-D	12	16.790	0.4430	449	8.6490E-14	3.4596E-15	65950	2820	SUERC	b7516
	MR1-E	12	8.082	0.4440	449	3.2922E-14	2.0311E-15	49022	3630	SUERC	b7517
	MR1-F	12	3.396	0.4437	449	1.6349E-14	1.7186E-15	51622	7518	SUERC	b7518
PC1	PC1-A	2	15.038	0.7548	266	2.4577E-13	5.7023E-15	217882	5090	LLNL	BE25604
	PC1-B	2	15.057	0.7547	266	3.3277E-13	7.7090E-15	295087	6870	LLNL	BE25605
	PC1-C	4	3.722	0.4740	424	1.0741E-13	2.0110E-15	377744	7837	LLNL	BE31909
	PC1-F	4	3.836	0.4747	424	8.9570E-14	2.6040E-15	304521	9574	LLNL	BE31910
	PC1-G	4	2.930	0.4752	424	7.3082E-14	2.2039E-15	323340	10808	LLNL	BE31911
PI1	PI1-A	13	15.277	0.3345	759.44	1.2839E-13	2.6111E-15	140821	2912	ANSTO	XBE0652
	PI1-B	13	15.089	0.3370	759.44	1.6997E-13	2.9596E-15	190768	3364	ANSTO	XBE0653
	PI1-C	13	17.456	0.3364	759.44	2.3720E-13	4.1261E-15	230355	4041	ANSTO	XBE0654
	PI1-D	13	17.199	0.3370	759.44	2.2386E-13	4.6420E-15	220950	4621	ANSTO	XBE0655
	PI1-E	13	15.639	0.3365	759.44	3.0952E-13	5.3890E-15	336163	5889	ANSTO	XBE0656
	PI1-F	13	7.191	0.3354	759.44	1.7440E-13	3.0359E-15	408877	7205	ANSTO	XBE0657
	PI1-FR	13	7.932	0.3368	759.44	1.9565E-13	3.4074E-15	418016	7357	ANSTO	XBE0658
PI2	PI2-A	14	11.785	0.3371	759.44	6.1966E-14	1.3491E-15	78856	2010	ANSTO	XBE0661
	PI2-B	14	8.108	0.3346	759.44	5.4182E-14	1.5095E-15	97466	3228	ANSTO	XBE0662
	PI2-C	14	7.462	0.3364	759.44	6.9973E-14	1.3298E-15	142600	3125	ANSTO	XBE0663
	PI2-D	14	11.952	0.3366	759.44	1.1711E-13	2.3714E-15	156450	3418	ANSTO	XBE0664
	PI2-E	14	9.601	0.3366	759.44	1.0400E-13	1.8295E-15	171435	3302	ANSTO	XBE0665
	PI2-F	14	9.888	0.3320	759.44	1.5581E-13	3.1005E-15	252463	5309	ANSTO	XBE0666
PNT01	PNT01-A	15	16.764	0.4461	449	1.8916E-13	4.6314E-15	148666	3760	SUERC	b7160
	PNT01-B	15	17.843	0.4452	449	1.5317E-13	6.5007E-15	112451	4909	SUERC	b7161
	PNT01-C	15	18.500	0.4453	449	1.3336E-13	3.9339E-15	94176	2908	SUERC	b7163
	PNT01-D	15	15.478	0.4451	449	9.7929E-14	4.2687E-15	81941	3756	SUERC	b7164
	PNT01-E	15	16.535	0.4453	449	9.7929E-14	3.4875E-15	76738	2902	SUERC	b7165
	PNT01-F	16	15.383	0.4471	449	2.1316E-13	5.3289E-15	185099	4663	SUERC	b7145
	PNT01-G	15	14.457	0.4459	449	8.2584E-14	3.2364E-15	73686	3098	SUERC	b7166
PP1	PP1-A	3	20.008	0.4703	424	9.4311E-13	1.9196E-14	626127	12795	LLNL	BE26584
	PP1-B	3	20.126	0.4741	424	3.8192E-13	8.8062E-15	252954	5903	LLNL	BE26585
	PP1-C	3	20.014	0.4727	424	9.6795E-14	1.5763E-15	62818	1190	LLNL	BE26586
	PP1-D	3	20.021	0.4722	424	9.8288E-14	2.2646E-15	63726	1610	LLNL	BE26587
	PP1-H	1	6.685	0.4752	424	1.6588E-13	3.8657E-15	329342	7836	LLNL	BE32157
	PP1-I	1	7.912	0.4739	424	5.3514E-14	1.3711E-15	86837	2445	LLNL	BE32158
	PP1-J	1	8.206	0.4750	424	3.3698E-13	9.0747E-15	548796	14900	LLNL	BE32159
	PP1-K	1	8.563	0.4750	424	3.5990E-14	1.0873E-15	52880	1845	LLNL	BE32160

Table 1.1. (continued)

PBR ID	Sample ID	Blank*	Quartz (g)	Be carrier (g)	[^{9}Be] (ug/g)	^{10}Be/^{9}Be†	1σ	[^{10}Be] atoms/g	1σ§	Facility	AMS ID
RT1	RT1-B	3	20.0344	0.4737	424	3.5255E-13	8.1060E-15	234216	5458	LLNL	BE26589
	RT1-C	3	20.0261	0.4726	424	1.9208E-13	4.4041E-15	126477	2996	LLNL	BE26590
	RT1-D	3	19.4975	0.4735	424	3.0566E-13	7.0036E-15	208302	4852	LLNL	BE26591
	RT1-G	4	6.5217	0.4747	424	7.0220E-14	1.5456E-15	139198	3609	LLNL	BE31916
	RT1-H	4	5.1906	0.4740	424	4.7571E-14	1.2588E-15	116037	3888	LLNL	BE31917
	RT1-I	4	6.2352	0.4749	424	5.8198E-14	1.4270E-15	119712	3552	LLNL	BE31918
	RT1-J	4	5.9923	0.4744	424	1.1030E-13	2.0520E-15	241297	4957	LLNL	BE31919
	RT1-K	4	7.4956	0.4748	424	1.0348E-13	1.9249E-15	180826	3756	LLNL	BE31920
SW02	SW02-A	17	9.080	0.3385	759.44	9.3890E-15	5.3885E-16	12193	1140	ANSTO	XBE0359
	SW02-B	17	11.448	0.3382	759.44	1.0202E-14	5.1782E-16	10881	876	ANSTO	XBE0360
	SW02-C	17	10.799	0.3381	759.44	1.0070E-14	5.0293E-16	11322	907	ANSTO	XBE0361
	SW02-D	17	10.672	0.3393	759.44	1.0145E-14	5.0545E-16	11618	925	ANSTO	XBE0362
	SW02-E	17	12.255	0.3387	759.44	1.4932E-14	6.0155E-16	16813	925	ANSTO	XBE0363
	SW02-F	17	14.213	0.3380	759.44	1.7285E-14	6.7793E-16	17307	881	ANSTO	XBE0364
	SW02-G	17	6.990	0.3384	759.44	1.0099E-14	5.3469E-16	17578	1472	ANSTO	XBE0365
	SW02-G (R)	17	6.236	0.3375	759.44	1.0298E-14	5.1130E-16	20197	1588	ANSTO	XBE0366
UCR1	PBR1-A	18	9.5211	0.2035	1082.27	3.4626E-14	1.2132E-15	49122	1953	LLNL	BE33167
	PBR1-B	19	8.2145	0.1816	1082.27	3.3420E-14	1.1468E-15	47037	2433	LLNL	BE33170
	PBR1-C	18	7.3345	0.1769	1082.27	3.4778E-14	1.4589E-15	55697	2612	LLNL	BE33168
	PBR1-E	20	5.6500	0.2116	1082.27	2.7482E-14	1.3996E-15	66807	3910	LLNL	BE33173
YV1	YV1-A	10	5.979	0.4477	449	1.3838E-14	1.1551E-15	21562	3326	SUERC	b6961
	YV1-B	10	7.241	0.4475	449	1.5736E-14	1.6768E-15	21314	3552	SUERC	b6962
	YV1-C	10	12.792	0.4461	449	2.5389E-14	2.5250E-15	22128	2814	SUERC	b6964
	YV1-D	10	12.539	0.4482	449	2.4161E-14	2.2627E-15	21364	2622	SUERC	b6965
	YV1-E	10	15.412	0.4462	449	3.8781E-14	2.3548E-15	30003	2198	SUERC	b6966
	YV1-F	10	14.231	0.4514	449	3.2922E-14	1.9893E-15	27295	2088	SUERC	b6967
	YV1-G	10	14.707	0.4481	449	4.3524E-14	2.9295E-15	35911	2809	SUERC	b6968
	YV1-H	10	14.875	0.4491	449	5.0778E-14	2.5361E-15	42155	2446	SUERC	b6972

Notes:

Samples PI1-FR and SW02-G (R) are replicates of the samples PI1-F and SW02-G, respectively. The mean and standard deviation of measured concentration of both the original sample and replicate were used as the concentration and uncertainty of these samples in the fragility age modeling.

*Blank information is provided in Supplementary Materials: Table 1.4.

†LLNL ^{10}Be/^{9}Be data were normalized to the primary standard 07KNSTD3110 with an assumed value of 2.85×10^{-12}, SUERC data were normalized to NIST standard with an assumed value of 2.79×10^{-11}, and ANSTO data were normalized to the primary standard KN-5-2 with a nominal value of 8.558×10^{-12} (Nishiizumi et al., 2007).

§Uncertainties include error on the sample and blank propagated in quadrature.

Table 1.2. Full parameters used for stream sediment sample data reduction.

Sample ID	Blank*	Quartz (g)	Be carrier (g)	[Be] (ug/g)	$^{10}Be/^{9}Be^{\dagger}$	1σ	[^{10}Be] atoms/g	1σ§	Facility	AMS ID
BS-SED	3	20.0463	0.4715	424	1.6436E-13	6.9053E-15	107583	4634	LLNL	BE26602
BR1-I	6	7.303	0.9693	204	1.0072E-13	3.0132E-15	177424	5600	SUERC	b7580
GV1-H	6	15.979	0.9706	204	1.7996E-13	5.1615E-15	146807	4314	SUERC	b7581
GV-SED	4	37.999	0.475	424	3.2903E-13	9.8076E-15	115565	3486	LLNL	BE26406
LJ-SED	3	21.1473	0.4716	424	1.3335E-13	2.3627E-15	82413	1581	LLNL	BE26599
LJB-SED2	11	11.98	0.4414	449	6.5286E-14	2.7035E-15	67699	3150	SUERC	b6851
MR1-G	6	8.978	0.8805	204	8.0631E-14	2.5277E-15	104245	3510	SUERC	b7587
PI1-G	13	12.726	0.334	759.44	2.7750E-13	5.5200E-15	367395	7358	ANSTO	XBE0659
PI2-G	14	6.527	0.3342	759.44	6.2732E-14	1.3266E-15	143147	3705	ANSTO	XBE0667
PNT01-I	6	6.017	0.971	204	3.4875E-14	1.7661E-15	70876	4186	SUERC	b7592
YV1-K	6	7.982	0.9698	204	3.0690E-14	1.7772E-15	46431	3169	SUERC	b7593

Notes:
*Blank information is provided in Supplementary Materials: Table 1.4.
†LLNL $^{10}Be/^{9}Be$ data were normalized to the primary standard 07KNSTD3110 with an assumed value of 2.85×10^{-12}, SUERC data were normalized to NIST standard with an assumed value of 2.79×10^{-11}, and ANSTO data were normalized to the primary standard KN-5-2 with a nominal value of 8.558×10^{-12} (Nishiizumi et al., 2007).
§Uncertainties include error on the sample and blank propagated in quadrature.

Table 1.3. Full parameters used for saprolite sample data reduction.

Sample ID	Blank*	Quartz (g)	Be carrier (g)	[Be] (ug/g)	$^{10}Be/^{9}Be^{\dagger}$	1σ	[^{10}Be] atoms/g	1σ§	Facility	AMS ID
BS1-D	3	21.2654	0.4727	424	2.09535E-13	4.98209E-15	130125	3180	LLNL	BE26601
GV1-I	6	17.422	0.9724	204	1.9502E-13	5.1057E-15	146360	3922	SUERC	b7582
GV2-5	3	20.0672	0.4728	424	1.6480E-13	4.4500E-15	108059	3021	LLNL	BE26596
LJ1-4	3	20.0342	0.4732	424	1.1637E-13	2.2313E-15	75919	1592	LLNL	BE26598
MR1-H	6	15.762	0.9704	204	7.6725E-14	2.6672E-15	62162	2316	SUERC	b7588
PNT01-H	6	18.129	0.971	204	8.5932E-14	2.9574E-15	60802	2220	SUERC	b7589
SW02-H	17	14.973	0.3376	759.44	9.3746E-15	4.8009E-16	7358	630	ANSTO	XBE0367

Notes:
*Blank information is provided in Supplementary Materials: Table 1.4.
†LLNL $^{10}Be/^{9}Be$ data were normalized to the primary standard 07KNSTD3110 with an assumed value of 2.85×10^{-12}, SUERC data were normalized to NIST standard with an assumed value of 2.79×10^{-11}, and ANSTO data were normalized to the primary standard KN-5-2 with a nominal value of 8.558×10^{-12} (Nishiizumi et al., 2007).
§Uncertainties include error on the sample and blank propagated in quadrature.

Table 1.4. Data on process blanks

Blank*	Blank ID	$^{10}Be/^{9}Be$†	1σ	Facility	AMS ID
1	BLK102911	2.3433E-15	4.4204E-16	LLNL	BE32172
2	BLK062408	1.5592E-15	1.9010E-16	LLNL	BE25606
3	BLK031009	3.5027E-15	3.3830E-16	LLNL	BE26582
	BLK031809	2.3376E-15	2.8443E-16	LLNL	BE26583
4	BLK062911	1.9998E-15	2.6591E-16	LLNL	BE31893
	BLK071311	2.5527E-15	3.8903E-16	LLNL	BE31927
	BLK072811	3.6149E-15	3.6338E-16	LLNL	BE31935
5	CFG1308	4.4361E-15	7.9794E-16	SUERC	b6855
6	CFG1320	2.6561E-15	7.0866E-16	SUERC	b7579
7	CFG1309	3.4317E-15	8.5932E-16	SUERC	b6931
8	CFG1307	1.6907E-14	2.2599E-15	SUERC	b6824
9	BLK210818	1.6713E-15	4.3158E-16	ANSTO	XBE0346
10	CFG1310	4.2408E-15	9.2628E-16	SUERC	b6952
11	CFG1306	4.0455E-15	9.0117E-16	SUERC	b6631
12	CFG1316	3.1806E-15	8.5095E-16	SUERC	b7361
13	BLK031019B	1.6549E-15	2.19356E-16	ANSTO	XBE0651
14	BLK300919B	7.6416E-15	5.22599E-16	ANSTO	XBE0660
15	CFG1313	2.9574E-15	8.5653E-16	SUERC	b7157
16	CFG1311	8.928E-16	4.464E-16	SUERC	b7379
17	BLK290818B	2.9442E-15	2.70301E-16	ANSTO	XBE0358
18	CB070312	2.84658E-15	3.53685E-16	LLNL	BE33155
19	CB100212	3.99941E-15	1.00064E-15	LLNL	BE33152
20	CFG1202	2.8158E-15	3.37725E-16	LLNL	BE33154

Notes:

*Each number corresponds to the number in the 'Blank' column in the preceding tables. The blanks with ID 3 and 4 use the average ratio and standard deviation as the blank correction.

†LLNL $^{10}Be/^{9}Be$ data were normalized to the primary standard 07KNSTD3110 with an assumed value of 2.85×10^{-12}, SUERC data were normalized to NIST standard with an assumed value of 2.79×10^{-11}, and ANSTO data were normalized to the primary standard KN-5-2 with a nominal value of 8.558×10^{-12} (Nishiizumi et al., 2007).

Table 2. Inputs to Balco et al. (2011) fragility age model: Sample-specific constants, and ^{10}Be concentrations for all the PBR samples.

PBR ID	Sample ID	Sample thickness (cm)*	Distance below PBR top (cm)†	S0,i§	Li (g cm^{-2})§	[Be-10] (atoms/g)	1σ
BR1	BR1-A	5	116	0.791	183.9	305795	6141
	BR1-B	2	147	0.621	209.0	269295	5972
	BR1-C	2.5	178	0.656	196.5	189452	5705
	BR1-D	2.5	210	0.435	227.9	143274	4697
	BR1-E	2	238	0.437	218.0	126507	3129
	BR1-F	2	287	0.581	191.2	218176	4239
	BR1-G	1	329	0.782	177.5	240997	9819
BS1	BS1-A	3	234	0.383	232.8	168429	3940
	BS1-B	5	320	0.392	206.3	118844	2789
	BS1-C	3	378	0.146	219.4	77031	1938
	BS1-E	3.5	348	0.091	213.7	105462	2900
	BS1-F	2.5	300	0.287	236.6	128177	3107
	BS1-G	2	252	0.422	215.0	158231	3522
	BS1-H	1	198	0.494	215.0	203931	4105
BS2	BS2-A	7.5	111	0.743	187.5	44776	2345
	BS2-B	6	90	0.689	202.4	45811	2342
	BS2-C	6.5	71	0.712	200.8	48354	2482
	BS2-D	6	51	0.766	196.2	59126	2893
	BS2-E	6	30	0.861	175.7	61869	4548
	BS2-F	5.75	11	0.933	168.4	76788	3898
GV1	GV1-1	5	89	0.836	174.6	198296	3701
	GV1-B	1.5	3	0.959	163.8	448281	12855
	GV1-C	2.5	24	0.919	169.7	327809	14445
	GV1-D	1	49	0.839	178.1	240519	10219
	GV1-E	1.5	77	0.737	188.3	193520	5921
	GV1-F	2.5	101	0.75	177.6	166671	6188
	GV1-G	2	130	0.735	182.1	116687	4901
LB05	LB05-A	4	160	0.689	188.2	144402	5987
	LB05-B	5	140	0.679	189.5	168008	5704
	LB05-C	5.5	121	0.697	189.9	167795	5172
	LB05-D	5	102	0.725	183.8	187462	6787
	LB05-E	5	82	0.769	184.7	200837	5258
	LB05-F	6	61	0.849	175.5	232574	6328
LJ1	LJ1-1	7	249	0.508	206.8	128122	3175
	LJ1-2	4	467	0.630	184.9	65952	1875
	LB1-5	1.5	282	0.391	221.6	96060	2374
	LB1-6	2	322	0.244	246.6	58786	1927
	LB1-7	1	362	0.182	256.9	45139	1621
	LB1-8	1.5	393	0.158	257.3	42124	1335
	LB1-9	1.75	508	0.665	184.7	67040	1957

Table 2. (continued)

PBR ID	Sample ID	Sample thickness (cm)*	Distance below PBR top (cm)†	S0,i§	Li (g cm^{-2})§	[Be-10] (atoms/g)	1σ
LJ5	LJ5-A	2.5	261	0.547	192.3	149323	3060
	LJ5-B	2	235	0.598	190.3	251321	5142
	LJ5-C	2	210	0.625	188.7	295122	5926
	LJ5-D	2	169	0.618	189.0	295113	5917
	LJ5-E	2.5	132	0.676	186.8	383238	7671
	LJ5-F	2	94	0.711	185.1	423613	8469
	LJ5-G	2	52	0.781	182.3	481971	9625
LJB1	LJB1-A	5	48	0.946	163.4	355487	11932
	LJB1-B	3	82	0.764	188.0	277812	6411
	LJB1-C	3	118	0.644	197.4	207621	6342
	LJB1-D	5	148	0.579	228.5	192579	6150
	LJB1-E	2	198	0.628	196.8	156852	4490
	LJB1-F	1	250	0.774	178.2	141536	4715
	LJB1-G	1	274	0.863	174.5	192888	5065
LJB2	LJB2-A	1	18	0.944	167.1	367879	8314
	LJB2-B	2.5	43	0.858	175.6	283485	7334
	LJB2-C	2.5	63	0.818	178.1	274027	6352
	LJB2-D	3.5	87	0.866	173.3	248154	5894
	LJB2-E	2.75	122	0.776	181.3	224996	7499
MR1	MR1-A	2	112	0.805	181.0	174457	6264
	MR1-B	2	140	0.729	197.9	135758	7400
	MR1-C	3	175	0.631	207.5	91928	3406
	MR1-D	2.5	224	0.757	180.6	65950	2820
	MR1-E	2	254	0.689	184.8	49022	3630
	MR1-F	2	303	0.637	188.5	51622	7518
PC1	PC1-A	5	305	0.605	187.6	217882	5090
	PC1-B	4	246	0.624	197.7	295087	6870
	PC1-C	4	181	0.732	184.7	377744	7837
	PC1-F	2	137	0.690	192.1	304521	9574
	PC1-G	2	375	0.694	179.3	323340	10808
PI1	PI1-A	2	164	0.720	185.2	140821	2912
	PI1-B	2	129	0.759	183.8	190768	3364
	PI1-C	2	107	0.779	181.9	230355	4041
	PI1-D	2	94	0.689	187.2	220950	4621
	PI1-E	2	59	0.763	183.0	336163	5889
	PI1-F	2	29	0.821	179.3	413447	6463
PI2	PI2-A	2	290	0.761	181.6	78856	2010
	PI2-B	2	255	0.782	180.6	97466	3228
	PI2-C	2	226	0.840	172.7	142600	3125
	PI2-D	2	201	0.591	192.2	156450	3418
	PI2-E	2	167	0.646	188.9	171435	3302
	PI2-F	2	133	0.721	184.4	252463	5309

Table 2. (continued)

PBR ID	Sample ID	Sample thickness (cm)*	Distance below PBR top (cm)†	S0,i§	Li (g cm^{-2})§	[Be-10] (atoms/g)	1σ
PNT01	PNT01-A	2	26	0.804	181.4	148666	3760
	PNT01-B	2.75	55	0.773	182.5	112451	4909
	PNT01-C	3	84	0.720	185.0	94176	2908
	PNT01-D	1.5	107	0.704	185.4	81941	3756
	PNT01-E	2.5	139	0.673	186.8	76738	2902
	PNT01-F	1.75	2	0.816	180.9	185099	4663
	PNT01-G	2	195	0.743	184.7	73686	3098
PP1	PP1-A	3	19	0.980	155.2	626127	12795
	PP1-B	3	245	0.221	298.7	252954	5903
	PP1-C	3	285	0.145	327.3	62818	1190
	PP1-D	3	343	0.224	240.0	63726	1610
	PP1-H	3	180	0.567	210.4	329342	7836
	PP1-I	3	273	0.164	318.1	86837	2445
	PP1-J	3	138	0.713	193.2	548796	14900
	PP1-K	3	410	0.312	210.9	52880	1845
RT1	RT1-B	2	92	0.685	330.4	234216	5458
	RT1-C	2	192	0.455	220.6	126477	2996
	RT1-D	2	310	0.776	173.9	208302	4852
	RT1-G	1.5	151	0.506	217.0	139198	3609
	RT1-H	2.75	231	0.400	216.7	116037	3888
	RT1-I	2	270	0.398	209.3	119712	3552
	RT1-J	3.5	337	0.835	170.6	241297	4957
	RT1-K	2	376	0.747	179.9	180826	3756
SW02	SW02-A	2.5	240	0.616	189.2	12193	1140
	SW02-B	2.5	204	0.659	187.6	10881	876
	SW02-C	2	179	0.678	186.7	11322	907
	SW02-D	2.5	145	0.681	186.4	11618	925
	SW02-E	2.5	115	0.729	184.7	16813	925
	SW02-F	2.5	89	0.733	184.4	17307	881
	SW02-G	2.5	56	0.767	182.9	18888	1852
UCR1	PBR1-A	4.5	87	0.649	188.7	49122	1953
	PBR1-B	4	66	0.658	189.9	47037	2433
	PBR1-C	3.5	42	0.709	186.0	55697	2612
	PBR1-E	4	0	0.746	180.2	66807	3910
YV1	YV1-A	3.5	296	0.586	191.1	21562	3326
	YV1-B	1.5	267	0.610	189.6	21314	3552
	YV1-C	1.25	235	0.639	187.9	22128	2814
	YV1-D	1.25	208	0.657	187.4	21364	2622
	YV1-E	1.5	176	0.659	186.9	30003	2198
	YV1-F	1.5	145	0.663	187.4	27295	2088
	YV1-G	1.5	116	0.695	186.2	35911	2809
	YV1-H	1.5	85	0.755	183.6	42155	2446

Notes: A surface erosion rate of zero was used for all samples, with the exception of GV2-3 to match the value used by Balco et al. (2011).
[*]Measured in field when each sample was collected.
[†]Vertical height measured from the highest point on the top of the PBR to the sample point.
[§]Calculated using the code of Balco (2014).

Table 3. Best-fit parameter results of the fragility age forward model.

PBR Name	fval	t_0 (ka)	t_{tip} (ka)	$\varepsilon_{0,sp}$ (m/Myr)	$\varepsilon_{0,mu}$ (m/Myr)	ε_1 (m/Myr)
BR1	211.0	42.6	42.4	10.1	25.2	10000.0
BS1	3.0	15.9	4.4	2.9	0.1	238.1
BS2	2.2	4.7	4.6	109.0	36.2	9998.3
GV1	18.3	18.5	7.4	27.0	67.6	91.1
GV2	35.2	24.7	17.7	15.9	39.7	214.7
LB05	1.6	29.4	29.3	36.9	92.3	10000.0
LJ1	25.8	35.6	9.9	10.2	25.4	164.0
LJ5	14.9	79.0	49.7	30.1	75.2	65.4
LJB1	51.1	10.8	10.5	19.3	3.9	9999.9
LJB2	9.0	14.3	14.2	42.0	5.2	9999.8
MR1	4.4	4.9	1.3	4.1	9.1	622.0
PC1	110.9	31.6	22.9	10000.0	10000.0	353.4
PI1	14.5	22.4	11.5	26.1	65.2	95.3
PI2	55.5	21.3	4.1	8.2	12.8	135.9
PNT01	2.7	9.8	9.7	46.0	115.0	10000.0
PP1	735.7	138.8	26.3	10000.0	10000.0	29.5
RT1	75.9	43.1	38.3	36.7	91.6	725.8
SW02	11.2	1.8	1.7	269.6	673.9	9999.4
UCR1	1.9	12.9	12.9	190.2	475.5	9999.4
YV1	5.6	1.0	0.8	88.5	33.7	9999.7

Notes:
Results calculated with the 4-parameter forward model scheme of Balco et al. (2011).

Table 4. Median and 16th-84th percentile uncertainty parameter results of the fragility age forward model.

PBR Name	t_0 (ka)			t_{tip} (ka)			$\varepsilon_{0,sp}$ (m/Myr)			$\varepsilon_{0,mu}$ (m/Myr)			ε_1 (m/Myr)		
	Median	16th	84th	Median	16th	84th	Median	16th	84th	Median	16th	84th	Median	16th	84th
BR1	42.6	41.4	43.7	42.3	41.1	43.5	9.9	8.8	11.6	24.8	8.8	11.6	10000.0	10000.0	10000.0
BS1	14.7	6.8	19.3	4.7	3.7	5.9	2.7	2.1	3.7	0.1	2.1	3.7	261.6	197.1	1350.5
BS2	7.2	1.6	9.9	5.7	0.7	7.9	130.0	97.8	356.8	85.8	97.8	356.8	9988.9	239.0	9999.8
GV1	18.6	16.1	21.0	7.3	6.3	8.3	27.4	24.1	31.9	68.1	24.1	31.9	88.1	70.3	123.2
GV2	24.8	23.1	26.4	17.6	16.5	18.8	15.9	14.8	17.1	39.5	14.8	17.1	206.8	158.8	330.4
LB05	28.7	12.8	31.1	28.5	10.3	30.9	36.6	27.3	56.5	79.4	27.3	56.5	9999.5	9930.7	9999.9
LJ1	35.6	33.8	37.6	9.9	9.5	10.3	10.2	8.8	12.0	25.4	8.8	12.0	164.4	154.0	175.2
LJ5	80.2	70.1	86.8	49.8	48.3	51.2	35.3	13.5	4001.7	88.3	13.5	4001.7	62.6	53.4	91.6
LJB1	10.7	9.6	12.0	10.5	9.4	11.8	19.3	17.9	21.0	3.8	17.9	21.0	9999.9	9999.4	10000.0
LJB2	14.1	8.1	19.8	14.0	7.9	19.5	43.4	38.1	51.1	4.9	38.1	51.1	9999.8	9998.1	10000.0
MR1	3.5	0.3	7.7	1.3	0.1	2.3	4.0	3.7	4.5	9.2	3.7	4.5	969.2	393.3	9999.8
PC1	31.6	30.7	32.4	22.9	22.3	23.5	9999.7	9995.6	9999.8	9999.8	9995.6	9999.8	355.4	308.2	418.4
PI1	22.2	20.5	23.7	11.4	11.0	11.8	25.9	23.5	28.6	64.1	23.5	28.6	96.1	85.3	111.1
PI2	21.2	18.8	23.7	4.0	3.6	4.5	8.1	7.2	9.3	12.4	7.2	9.3	136.5	122.2	154.5
PNT01	9.5	7.7	10.1	9.4	7.5	9.9	46.1	43.9	48.5	110.5	43.9	48.5	10000.0	9999.8	10000.0
PP1	138.7	137.5	140.0	26.5	26.2	26.8	10000.0	9999.9	10000.0	10000.0	9999.9	10000.0	29.6	29.3	29.9
RT1	42.8	38.9	49.2	38.3	37.6	38.9	35.3	21.3	3999.9	87.6	21.3	3999.9	736.8	323.5	9999.9
SW02	1.8	0.5	2.1	1.5	0.2	1.7	295.4	234.1	503.8	587.2	234.1	503.8	9998.9	2961.3	9999.9
UCR1	12.8	6.9	14.4	12.4	6.3	13.7	200.3	142.4	470.7	428.0	142.4	470.7	9999.8	452.7	10000.0
YV1	2.7	0.4	3.6	1.8	0.1	3.0	99.2	77.7	161.6	66.4	77.7	161.6	9999.2	1467.3	10000.0

Notes:
Results calculated for the 4 free parameters. The Monte Carlo optimizer was run for 400 iterations, starting at the best-fit values in Supplementary Materials: Table 3.

Table 5. Stream sediment samples online erosion rate calculator inputs and outputs.

Sample name	Mean Latitude (DD)	Mean Longitude (DD)	Effective Elevation (m)	Elv/pressure flag	Thickness (cm)	Density (g cm^{-2})	Shielding correction	[Be-10] atoms g^{-1}	+/-	Be AMS standard	[Al-26] atoms g^{-1}	+/-	Al AMS standard	Erosion rate* (m/Myr)	+/-
BS-SED	33.9080	-116.9864	780.4	std	1	2	1	107583	4634	07KNSTD	0	0	KNSTD	53.2	3.9
BR1-I	33.5928	-116.9241	768.6	std	1	2	1	177424	5600	07KNSTD	0	0	KNSTD	31.5	2.1
GV1-H	34.2788	-117.2414	1540.6	std	1	2	1	146807	4314	07KNSTD	0	0	KNSTD	67.0	4.4
GV-SED	34.2831	-117.2450	1556.1	std	1	2	1	115565	3486	07KNSTD	0	0	KNSTD	85.5	5.7
LJ-SED	34.5943	-117.8518	940.6	std	1	2	1	82413	1581	07KNSTD	0	0	KNSTD	78.8	4.9
LJB-SED2	34.6024	-117.8568	943.5	std	1	2	1	67699	3150	07KNSTD	0	0	KNSTD	96.1	7.3
MR1-G	33.8088	-117.2535	561.4	std	1	2	1	104245	3510	07KNSTD	0	0	KNSTD	46.7	3.2
PI1-G	34.3063	-117.2260	1689.9	std	1	2	1	367395	7358	07KNSTD	0	0	KNSTD	29.8	1.9
PI2-G	34.2979	-117.2232	1535.6	std	1	2	1	143147	3705	07KNSTD	0	0	KNSTD	68.5	4.4
PNT01-I	34.1421	-116.4891	1260.2	std	1	2	1	70876	4186	07KNSTD	0	0	KNSTD	113.0	9.4
YV1-K	34.1180	-116.5105	1298.1	std	1	2	1	46431	3169	07KNSTD	0	0	KNSTD	174.0	15.7

Notes:

*Version 3 of the online exposure age calculator described by Balco et al. (2008), and subsequently updated, was used for calculations. Erosion rates were calculated using a ^{10}Be production rate of 4.132 ± 0.218 atoms g^{-1} yr^{-1}, based on the "primary" calibration data set of Borchers et al. (2016) and a constant production rate model and scaling scheme for spallation (Lal, 1991; Stone, 2000).

Table 6. Saprolite samples online erosion rate calculator inputs and outputs.

Sample name	Latitude (DD)	Longitude (DD)	Elevation (m)	Elv/pressure flag	Thickness (cm)*	Density (g cm^{-2})	Shielding correction†	[Be-10] atoms g^{-1}	+/-	Be AMS standard	[Al-26] atoms g^{-1}	+/-	Al AMS standard	Erosion rate§ (m/Myr)	+/-
BS1-D	33.89750	-116.98592	759	std	5	2	0.762	130125	3144	07KNSTD	0	0	KNSTD	33.7	2.2
GV1-I	34.27813	-117.23254	1437	std	3.5	2	0.924	146360	3922	07KNSTD	0	0	KNSTD	57.7	3.8
GV2-5	34.27878	-117.2471	1510	std	5	2	0.941	108059	2978	07KNSTD	0	0	KNSTD	82.2	5.4
LJ1-4	34.59453	-117.85326	947	std	7	2	0.916	75919	1508	07KNSTD	0	0	KNSTD	77.5	4.9
MR1-H	33.80942	-117.25282	534	std	4	2	0.934	62162	2316	07KNSTD	0	0	KNSTD	72.2	5.1
PNT01-H	34.13845	-116.47844	1125	std	7	2	0.896	60802	2220	07KNSTD	0	0	KNSTD	106.0	7.4
SW02-H	34.29688	-117.33979	1107	std	2.5	2	0.931	7358	630	07KNSTD	0	0	KNSTD	892.0	92.8

Notes:
*Measured in field when sample was collected.
†Calculated as the product of the topographic shielding measured in the field and shielding due to thickness of overlying soil.
§Version 3 of the online exposure age calculator described by Balco et al. (2008), and subsequently updated, was used for calculations. Erosion rates were calculated using a ^{10}Be production rate of 4.132 ± 0.218 atoms g^{-1} yr^{-1}, based on the "primary" calibration data set of Borchers et al. (2016) and a constant production rate model and scaling scheme for spallation (Lal, 1991; Stone, 2000).

References

Balco, G. (2014). Simple computer code for estimating cosmic-ray shielding by oddly shaped objects. *Quaternary Geochronology, 22*, 175-182. doi:10.1016/j.quageo.2013.12.002

Balco, G., Purvance, M. D., & Rood, D. H. (2011). Exposure dating of precariously balanced rocks. *Quaternary Geochronology, 6*(3), 295-303. doi:10.1016/j.quageo.2011.03.007

Balco, G., Stone, J. O., Lifton, N. A., & Dunai, T. J. (2008). A complete and easily accessible means of calculating surface exposure ages or erosion rates from 10Be and 26Al measurements. *Quaternary Geochronology, 3*(3), 174-195. doi:10.1016/j.quageo.2007.12.001

Borchers, B., Marrero, S., Balco, G., Caffee, M., Goehring, B., Lifton, N., et al. (2016). Geological calibration of spallation production rates in the CRONUS-Earth project. *Quaternary Geochronology, 31*, 188-198. doi:10.1016/j.quageo.2015.01.009

Lal, D. (1991). Cosmic ray labeling of erosion surfaces: in situ nuclide production rates and erosion models. *Earth and Planetary Science Letters, 104*(2), 424-439. doi:10.1016/0012-821X(91)90220-C

Nishiizumi, K., Imamura, M., Caffee, M. W., Southon, J. R., Finkel, R. C., & McAninch, J. (2007). Absolute calibration of 10Be AMS standards. *Nuclear Instruments and Methods in Physics Research Section B: Beam Interactions with Materials and Atoms, 258*(2), 403-413. doi:10.1016/j.nimb.2007.01.297

Stone, J. O. (2000). Air pressure and cosmogenic isotope production. *Journal of Geophysical Research: Solid Earth, 105*(B10), 23753-23759. doi:10.1029/2000JB900181